Mathematical modeling of metal ion homeostasis and signaling systems

Cui, J.

Publication date
2009
Document Version
Final published version

ISBN 978-90-8891-088-3

MATHEMATICAL MODELING OF CALCIUM HOMEOSTASIS AND SIGNALING SYSTEMS Jiangjun Cui

Mathematical Modeling of Metal Ion Homeostasis and Signaling Systems

Jiangjun Cui

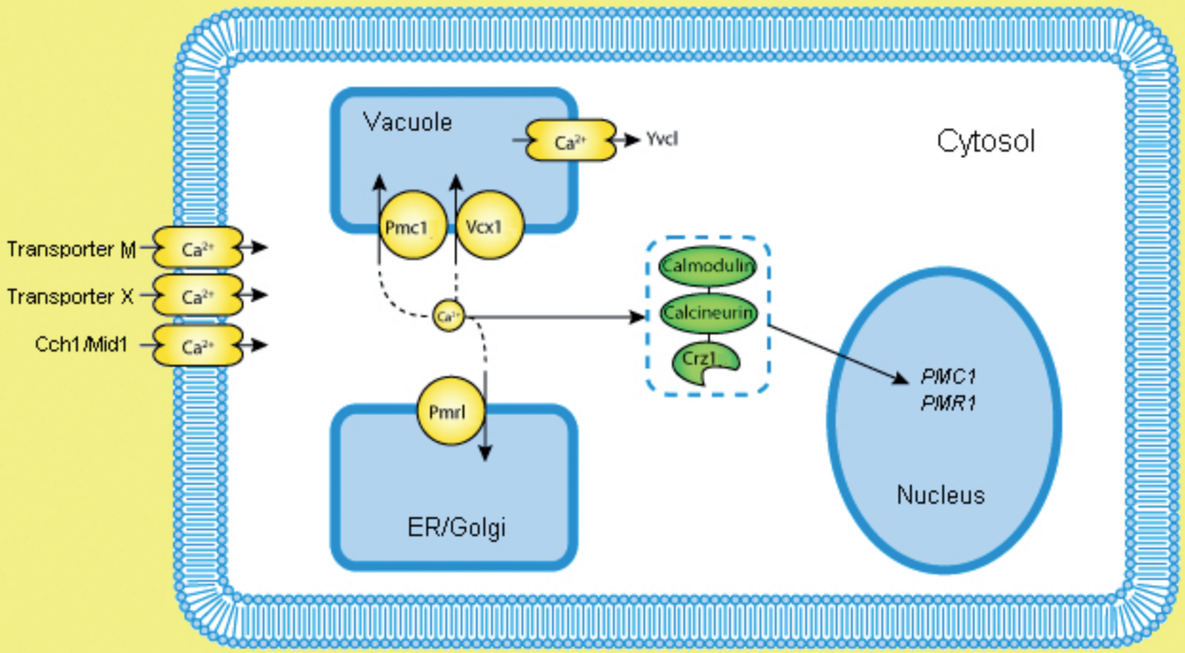

Mathematical Modeling of Metal Ion Homeostasis and Signaling Systems

ACADEMISCH PROEFSCHRIFT

ter verkrijging van de graad van doctor
aan de Universiteit van Amsterdam
op gezag van de Rector Magnificus
prof. dr. D.C. van den Boom
ten overstaan van een door het college voor promoties ingestelde
commissie, in het openbaar te verdedigen in de Agnietenkapel
op dinsdag 3 maart 2009, te 14:00 uur

door

Jiangjun Cui

geboren te Yin, China

Promotiecommissie:

Promotor:	**Prof. Dr. P.M.A. Sloot**
Co-promotor:	**Dr. J.A.Kaandorp**
Overige leden:	Prof. Dr. K.W. Cunningham Prof. Dr. R. van Driel Dr. Ir. A.G. Hoekstra Prof. Dr. Ir. J.J. Heijnen Dr. F.J. Bruggeman
Faculteit:	Faculteit Natuurwetenschappen, Wiskunde en Informatica

The work described in this thesis has been carried out in the Section Computational Science of the University of Amsterdam, with the financial support of the Dutch Science Foundation (NWO) and the European Commission (MORPHEX, NEST Contract No. 043322).

ISBN 978-90-8891-088-3

Printed by Box press, Oisterwijk.
Author contact: J.Cui@uva.nl

Cover figure: A schematic graph of calcium homeostasis system in budding yeast.

Contents

Chapter 1 General Introduction

The desire to understand life is as old as mankind [229]. Although the incredible diverse nature of living systems, often called biocomplexity, still forms a formidable challenge for computational science, it is believed that the method of computational and information science will help to establish the next generation biology [30,69]. In this post-genome era, the modeling and simulation of cellular processes such as signaling and metabolic pathways become increasingly important. The overwhelmingly great complexity and sophistication of these processes exceed our intuition and tax the most advanced mathematical and computational means [229]. The ability of mathematical and computational models to integrate collections of observations and connect them to a higher level of biological organization facilitates the understanding of cell function and physiological phenomena [30,37,166,229].

Metal ions such as calcium and zinc play critical roles in biological cells. For example, in eukaryoic cells, Ca^{2+} functions as a highly versatile intracellular messenger regulating a myriad of cellular processes such as proliferation, muscle contraction and neurotransmitter release [20-22,174,231]. Zinc serves as a structural component or catalytic cofactor in a large number of proteins such as RNA polymerase and zinc finger proteins and it also has very important signaling role [26,42,66,77,172,190,219]. The intracellular concentration of metal ions is usually under tight control through corresponding homeostasis systems involving coordination between ion uptake, distribution, storage and efflux [123,182]. Mathematical modeling and computational simulations are required for the understanding of metal ion homeostasis and signaling networks which is of fundamental importance in systems biology and has many applications in medicine (e.g., the understanding of zinc signaling in tumor cells will help devise thereupatic strategies to attenuate tumor growth, see Section 1.3.4.7. The understanding of calcium signaling in cardiac myocytes is critical for devising thereupatic drugs to treat diseases such as cardiac hypertrophy and heart failure, see Section 4.1). In this thesis, we will report some progress which we have made in this important field.

1.1 System Biology and Its Grand Challenges

"Every object that biology studies is a system of systems." Francois Jacob (1974).

Systems biology, as its name indicates, is an emergent field focusing on systematic study of complex interactions in biological systems [35,107,222,251]. According to Lilia Alberghina (University of Milano-Bicocca, Italy): "There is a growing awareness in medical science that biological entities are 'systems' -- collections of interacting parts" [252]. For example, in metal ion homeostasis and signaling systems, various proteins such as ion transporters, sensors and transcription regulators interact with each other and work together to achieve the tasks. However, it is only very recently that the systems approach becomes in fashion because the birth of functional genomics, the development of novel numerical methods, and the abundance of computational resources (due to the

usage of facilities for supercomputing, grid computing and cloud computing, etc.) make it possible to achieve system-level understanding of biological processes [35,107,222].

1.1.1 A Bit History of Systems Biology

The perspective of integration used by systems biology can be traced back to the Greek philosopher Aristotle (384–322 B.C.) who stated: "the whole is something over and above its parts and not just the sum of them all" [220]. As a newly emerged biological research field, systems biology finds its roots in the quantitative modeling of enzyme kinetics, the numerical methods developed to study neurophysiology, control theory and cybernetics [251].

The Austria-born biologist Ludwig von Bertalanffy (1901-1972) can be seen as a precursor of systems biology because of his “general systems theory”. The famous Hodgkin-Huxley model (1952) of the squid giant axon [105], developed by British neurophysiologists Alan Lloyd Hodgkin (1914-1998) and Andrew Fielding Huxley (1917-), described a cellular function (membrane action potential) emerging from the interaction between two components (a potassium channel and a sodium channel) and can therefore be seen as the beginning of (computational) systems biology [251].

System theorist Mihajlo Mesarovic (1928-) launched the formal study of systems biology as a distinct discipline in 1966 with an international symposium entitled "Systems Theory and Biology." Systems biology emerged as a movement in its own right around year 2000, symbolized by the establishment of Institutes of Systems Biology in Seattle and Tokyo [251]. Since then, various ambitious research initiatives and projects under the flag of systems biology have been launched such as the Silicon Cell Initiative (Amsterdam, the Netherlands) [248], the Virtual Physiological Human (VPH) Initiative (Multi-national) [257] and the IUPS Physiome project (Multi-national) [247].

1.1.2 Biological Complexity

Biological systems are often claimed to be dauntingly complex. Biological complexity is closely related to the characteristically hierarchical structure of biological systems [199,253]. The recognizable structure levels (from top to bottom) include ecosystem, community, population, organism, organ system, organ, tissue, cell and molecule. In this hierarchical organization, each higher entity is composed of numerous lower entities with intricate linkages of interactions to keep them together[1]. For example, a single *E. coli* cell consists of thousands of molecules including 6000-10,000 proteins, 2000 metabolites, 5000 mRNAs and 4000 genes with countless interactions among them to construct extremely complex networks [213].

In additional to the intricate interactions of biological entities on the same level that constitute the main source of biological complexity, another source of biological complexity originates from the constant interplay between events at different levels [253].

[1] With the exception that single celled organisms don’t contain tissue and organ level entities.

Such interplay may happen between events at extremely different time and space scales. For example, the course of evolution can be changed due to a unique molecular event such as a single mutation. On the other hand, the change of global environment (e.g., global warming) can be very influential in determining the biochemical transformations of ordinary cellular metabolism (e.g., those transformations which lead to coral bleaching) [201].

1.1.3 Computational Challenge and Other Challenges

Biological complexity imposes grand challenges to researchers in the field of systems biology, the first of which is experimental. To accurately simulate biological processes, one of the critical steps is to retrieve the correct data. New generations of high-resolution and high-throughput experimental equipments are needed to measure the properties of the molecules in biological cells, visualize their activity, etc. For example, in metal ion homeostasis and signaling systems, new technical devices are needed to determine various rate constants of the relevant protein-protein interactions. New imaging techniques need to be developed to monitor the concentration change of metal ions in biological cells. The lack of powerful visualization and image reconstruction methods has been one of the major impediments to studying the role of metal ions in various human diseases such as the role of Zn^{2+} in Alzheimer's disease [31,78,192,211,219].

The second grand challenge is computational [72,122]. For example, to achieve system-level understanding of biological cells, we need to model and simulate the dynamic behavior of gene regulation networks, intracellular signaling pathways, metabolic networks, etc [210,213,228]. To build an integrated human physiology, we must combine data from many related areas including *genome*, *proteome*, *metabolome*, and *physiome*, which embodies knowledge about genes, proteins, metabolic processes, and physiology. To handle such huge amount of data of great complexity, new modeling approaches and computational methods need to be developed and impressive computational resources are essential [72,118,199,222].

The third grand challenge is the collaboration. The research in the field of systems biology is highly interdisciplinary. To approximate the real biological systems using computational models and simulations, close collaborations between experimentalists, mathematicians, physicists, biochemists and computational scientists are necessary. Good communication is extremely important for successful collaboration. Very often, molecular biologists complain that their colleagues responsible for computational research do not understand the biological terms in their words, whereas computational scientists often complain that their computational methods are often misunderstood by their biologist colleagues.

In addition, there seems to be a paradox related to biological data: on the one hand, we have seemingly over-opulent data, many of them are now stored in all kinds of databases [246,249,250]; on the other hand, we frequently face the situation of data scarcity when doing modeling [204]. For example, to model the *in vivo* dynamics of zinc homeostasis system in *E. coli*, we will find that besides the lack of many kinetic rate constants, even

the most basic data such as the exact value of cytosolic zinc concentration is missing because of the limitation of the current technology [163], which further illustrates the experimental challenge of systems biology. In some other cases, the measurement of missing data can be achieved with the help of various experimental groups that have corresponding technical equipments, which further illustrates the challenge of collaboration. Thus the motivation of finding the missing data makes mathematical and computational modeling a good way of promoting the data collection process and systematically organizing the data.

1.1.4 Prize for Efforts: The Golden Fleece

The prizes to be attained after dealing with the above mentioned grand challenges are immense. The mostly direct prize will be in medical science. Systems biology has the potential to have general profound effects on the healthcare and medical science ranging from in silico drug design and testing to individualized medicine by using model-based experimentation techniques. Complex diseases such as diabetes, heart failure, cancer, and metabolic syndrome, for which there are currently no cures, can be predicted and treated as systems biology progresses [14,222,252]. As we will introduce later, metal ion homeostasis and signaling processes are closely related to many human diseases (for example, the accumulation of copper in body tissues can cause the symptoms of Wilson's disease [209,251]; the shortage of potassium in body fluids can lead to cardiac arrhythmia [251] and calcium signaling network in cardiac myocytes is responsible for controlling cardiac hypertrophy). Thus the understanding of these processes is certainly necessary and critical for treating these relevant diseases.

The second prize to be attained will be in agriculture and material science. According to Uwe Sauer (the Institute of Molecular Systems Biology, ETH Zurich, Switzerland): (a systems-perspective could) "open up entirely new options for the production of chemicals, food products and in plant breeding" [252]. For example, the thorough understanding and accurate simulation of biomineralization processes in the organisms such as corals and sponges through systems biology approach will potentially lead to the manually-controlled production of minerals through biological organisms. Since biomineralization processes are often closely related with metal ion homeostasis and signaling processes (for example, calcium calcification in coral is based on calcium homeostasis in cells in various coral tissues), mathematical modeling of the later processes will be certainly quite necessary for understanding the former ones [6].

The third prize to be attained will be inspiration of new theoretical sciences and new directions in relevant existent sciences and their applications in engineering. In the past centuries, investigations on biological problems had promoted the birth of many sciences and new computational methodologies [10,73,151,203,251]. For example, the mathematical modeling of natural, biological processes has resulted in the birth of an interdisciplinary field of study named as mathematical biology [65,151,178]. Very recently (actually in 2002), the systems biology study of complex biological networks has led to a new theory named as network motif theory (see Chapter 6) [10,11]. It is natural to anticipate that such trends will continue. In order to tackle the numerous open

questions (e.g., protein folding, the encoding of calcium signaling specificity, reaction-diffusion systems with boundaries of complex geometry, etc.) related to complex biological phenomena, new theoretical sciences (including new mathematics, new chemistry, etc.) and new computational methods are most likely required [222].

Finally let me end this section with an analogy with a well-known Greek mythology: Argonauts and Jason sought for the Golden Fleece. If we think of the grand challenges of systems biology as the great dangerous things met by the Argonauts and Jason on their voyage and adventures (the harpies, the clashing rocks and the sleepless dragon, etc.), what we need to do is to build a strong team of Argonauts composed of excellent biologists, mathematicians, physicists, biochemists and computational scientists, whose diligent, continuous and collaborative works will make them conquer all the difficulties on the way and eventually acquire the golden fleece.

1.2 Mathematical Modeling

Models are used as abstractions of reality whose representation includes diagrams, laws, graphs, equations, plots, etc [72,80]. A mathematical model is an abstract model that uses mathematical language to describe a system [251]. Although qualitative models such as boolean networks can be useful for describing systematic structures and processes, in this thesis we will mainly focus on quantitative mathematical models.

1.2.1 The Role, Levels and Strategies of Modeling

Modeling lies at the heart of systems biology [72,80]. Mathematical models and their computer simulations can help us to understand the involved dynamics of complex interactions of biological structures (or entities), based on which the system-understanding of biological systems becomes possible. Modelers start from experimentally acquired data and observed phenomena, make assumptions and devise hopefully useful models, which can make predictions of the behavior of studied systems and these predictions are further validated by new experiments, the results of which are used to help improve the models. Such iterations between experiments and models are the only possible way leading to realistic models, which also illustrates the necessity of close collaboration between experimentalists and modelers [72].

The levels of models are closely related to the hierarchy of biological systems. As shown in Fig. 1.1, models at the most fundamental level are those for molecules such as DNA (genes) and proteins. Models at intermediate levels include those for describing intracellular networks, cell-cell and transmembrane signals. Models at the top levels consist of those for tissues, organs, organisms and ecosystem, etc.

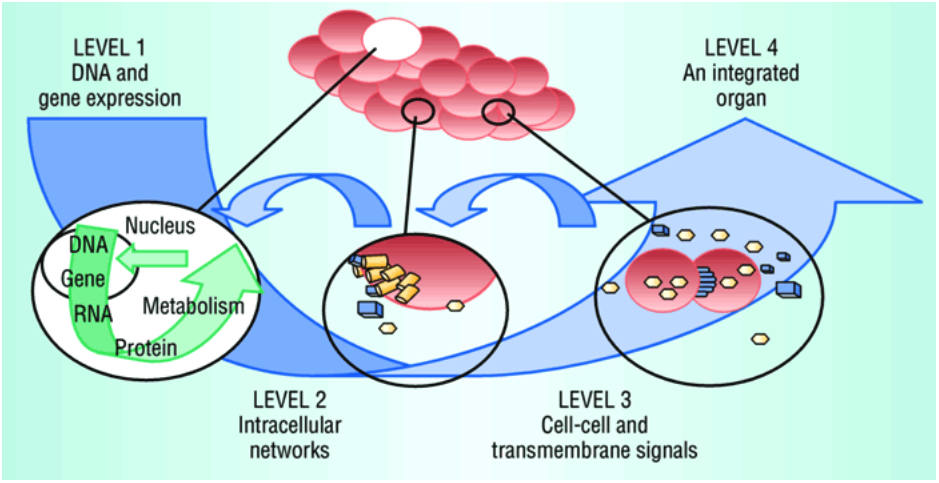

Figure 1.1. Different levels of models in systems biology. From bottom to top are models for DNA and gene expression, intracellular networks, cell-cell and transmembrane signals and integrated tissue or organ. Even higher levels of models such as models for populations and ecosystem are not shown here (this figure is taken from Ref. 72).

As abstraction of certain aspects of complex biological systems, models always need judicious simplification which means a trade-off between simplicity and accuracy of the model. The strategies of modeling include simplification, construction and integration. Occam's Razor is a very useful principle for modeling, which means that among models with roughly equal predictive power, the simplest one is the most desirable [72].

1.2.2 Approaches of Mathematical Modeling

Mathematical models in biology mainly include difference equations, ordinary differential equations and partial differential equations [65,67,151,178]. Difference equations are special recurrence relations which define recursive sequences of numbers, which are widely used in population biology because the number of individuals is essentially discrete. For example, the Nicholson-Bailey model is a theoretical model for host-parasitoid systems using difference equations [65]. A more well-known example is that of the dynamic growth of a rabbit population which can be described by a concise difference equation ($P_{n+1} = P_n + P_{n-1}$ for n>0 with $P_0 = P_1 = 1$ where P_n denotes the number of rabbit pairs at the end of the nth month) leading to the famous Fibonacci sequence.

However, the majority of mathematical models in biology belong to differential equations which have been used for modeling both discrete and continuous biological processes. For example, the well-known Lotka-Volterra model consists of two ordinary differential equations for describing interactions of predator-prey populations. The Hodgkin-Huxley model consists of four ordinary differential equations for describing the dynamics of membrane action potential in a squid axon which is essentially continuous [105]. As we will see later, in many cases, the main gradients of systems biology such as feedback controls and enzyme kinetics can be expressed into the form of differential equations.

Ordinary differential equations (ODEs) describe the quantitative relations between variables and their derivatives, whose classical examples include the above mentioned two models (the Lotka-Volterra model and the Hodgkin-Huxley model). To a first approximation, many biological reaction networks can be described mathematically by a set of ODEs that track the effects of the simultaneously occurring reactions. The ODE method is extremely suitable and effective for modeling complicated intracellular networks (e.g., signaling networks and metabolic pathways) in relatively small cells where certain spatial effects (e.g., diffusion) can be neglected [69,188,213].

In other cases when spatial effects are important, partial differential equations become a more amenable tool for approximating biological systems. Examples of PDE models in biology include models for blood flow, cell motions, traveling calcium waves, chemotaxis and pattern formation [65,69,71,151]. Compared with ODE models, PDE models are usually much more difficult for numerical simulations. The irregular boundaries (e.g., those composed of the membranes of cells and/or cellular organelles) add much to this difficulty [112].

According to their properties, many mathematical models can be classified as linear vs. nonlinear, deterministic vs. probabilistic (stochastic)**,** static vs. dynamic, lumped parameters (for homogeneous models) vs. distributed parameters (for heterogeneous models, typically represented by PDEs) [251]. In this thesis, we restrict ourselves to nonlinear ODE models, the properties of which will be further illustrated in Section 1.5.3.

1.2.3 Multi-Scale Modeling

The hierarchical structure of biological systems determines the necessity of multi-scale modeling, especially when we want to achieve such ambitious goals such as predicting and treating human disease based on molecular-level knowledge [156,157,199,204]. As mentioned before, one major source of biological complexity origins from the constant interplay between events at different levels of biological systems with extremely different time and space scales [253]. Multi-scale modeling is necessary for capturing and reproducing the dynamic characteristics of such constant interplay by integrating information from lower levels (molecule and cell) to higher levels (tissue, organ, organ system and organism, etc.). Multi-scale modeling will be the ultimate modeling framework of systems biology and is expected to summarize knowledge (including physiology and molecular biology) of the broad biological context in a quantitative manner. The classical 19th century problems in physiology and disease will be addressed by the 21st century molecular technologies and by adopting the systems biology approach based on multi-scale modeling [204].

1.3 Metal Ion Homeostasis and Signaling Systems

The relation between metals and living organisms is complicated. On one hand, many metals are essential for life as macronutrients or micronutrients and play important roles in its metabolism and growth. Micronutrients such as Co, Cu, Cr, Fe, Mn, Mo and Zn are

needed for human in small quantities (generally less than 100mg/day), which are also referred to as trace elements whose average concentrations are less than 100μg/g in the human body [123,251]. Macronutrients such as Na, Mg, K and Ca are needed in larger quantity and generally found in group IA and IIA of the periodic table. Insufficient intake of essential metals including macronutrients or micronutrients results in diseases or growth retardation [123]. On the other hand, metals are probably the oldest known toxins for life. Excessive intake of essential and some non-essential metals (e.g., Pb, Cd and Hg) results in toxicity. In this regard, highly regulated metabolic pathways (i.e., metal ion homeostasis systems) have been developed by living organisms to maintain essential or non-essential metals at optimal concentration ranges whereas detoxification mechanisms are used for many of the non-essential toxic metals [123,153].

1.3.1 Functions of Main Essential Metals

The major functions of main essential metals are listed in the following Table 1.1. An interesting observation may be that Al (aluminum), the most abundant metal in the Earth's crust is not in this list, the reason of which is that aluminum has no known function in living cells [251]. Another important fact worthy of notice is that Na, which is an essential macronutrient for human and other animals, is not needed by the plant [251]. This observation indicates the different requirements for particular metals in different kinds of organisms.

Table 1.1: Major functions of eleven metals which are essential for human [236,251]

Metal Symbol	Name and Ion Forms	Major functions in life
Ca	Calcium (Ca^{2+})	the most ubiquitous intracellular second messenger carrying signals to regulate a myriad of biological processes including proliferation, muscle contraction, neurotransmitter release and cell apoptosis; a major structural element in bones, calcified cartilage, teeth and shells
Mg	Magnesium (Mg^{2+})	help maintain normal muscle and nerve function; keep heart rhythm steady and bones strong; support a healthy immune system; help regulate blood sugar levels and promote normal blood pressure; needed for healthy teeth and energy metabolism; essential to the basic nucleic acid chemistry of life; a cofactor for ATP (adenosine triphosphate) and a number of enzymes; a regulator of ion channels; required for the structural integrity of numerous proteins and nucleic acids; a major component of chlorophylls in plants
Na	Sodium (Na^{+})	important for regulation of blood and body fluids; important for transmission of nerve impulses; important for muscle function and heart activity; having certain metabolic functions (please note that sodium ion is not needed by plants)
K	Potassium	work with sodium to maintain the body's water balance, thus important for regulation of blood and body fluids; important for

	(K^+)	transmission of nerve impulses; important for muscle function and heart activity; help the kidneys function normally
Fe	Iron (Fe^{2+}, Fe^{3+})	necessary for formation of hemoglobin, brain development and function, regulation of body temperature, muscle activity and catecholamine metabolism; essential for a healthy immune system and hair growth; structural component of cytochrome proteins and some other proteins; contributing to redox reactions in the iron-sulfer clusters of many enzymes such as nitrogenase
Co	Cobalt (Co^{2+} , Co^{3+} are most prevalent)	a central constituent of the vitamin B_{12} , work with it to prevent anemia and ensure the health of the nervous system
Cr	Chromium (Cr^{3+} is essential and Cr^{6+} is very toxic. All oxidation states from I to VI exist)	involved in amino acid transport and breakdown of glycogen and lipids; essential in order for insulin to function and important in the metabolism of fats and carbohydrates; stimulating fatty acid and cholesterol synthesis; an activator of several important enzymes
Cu	Copper (Cu^+, Cu^{2+})	important for synthesis of hemoglobin, proper iron metabolism, and maintenance of blood vessels; vital in making elastin, a chief component of the elastic muscle fibers found throughout the body; needed to build strong bones, connective tissue and joints; an essential components of macromolecules such as metalloenzymes and copper-based pigments; used for biological electron transport
Mn	Manganese (Mn^{2+} is most stable, although oxidation states from I to VII exist)	needed for bone development and maintenance of strong bones; helping to activate enzymes that are necessary for the body's proper use of biotin, B1 and vitamin C; important in the utilization of thiamine and the formation of thyroxin; cofactor of enzymes such as arginase and ligases ; component of the oxegen evolving complex (OEC), a water-oxidizing enzyme contained in chloroplast membrane in plants
Zn	Zinc (Zn^{2+} is the prevalent form, Zn^+ is rare)	structural component or catalytic cofactor in many proteins (e.g., zinc finger proteins; it is estimated that ~3000 proteins in human contain zinc); having signaling roles and functioning both as an intracellular second messenger and secreted signaling molecule in synaptic transmission, etc.; activator of certain enzymes such as carbonic anhydrase; playing role in olfaction

Mo	Molybdenum (Mo^{6+}, Mo^{5+}, Mo^{4+}, Mo^{3+}, Mo^{2+}, Mo^{+})	a cofactor for a number of enzymes that catalyze important chemical transformations in the global carbon, nitrogen, and sulfur cycles, three of which (sulfite oxidase, xanthine oxidase and aldehyde oxidase) are in human

1.3.2 Metals-Related Human Diseases

As mentioned before, deficiency of essential metals in human can lead to lots of diseases. For example, a shortage of potassium in body fluids may cause a potentially fatal condition known as hypokalemia whose symptoms include muscular weakness, lack of energy, muscle cramps, stomach disturbances and occasional cardiac arrhythmias, etc. Long-term calcium deficiency can result in osteoporosis, a disease of bone leading to an increased risk of fractures. Zinc deficiency can cause hair loss, skin lesions, diarrhea, wasting of body tissues and malfunctions of eyesight, taste, smell and memory. The symptoms of chromium deficiency include severely impaired glucose tolerance, a loss of weight, and confusion. Iron deficiency is the most common form of nutritional deficiency and it can lead to a disease named as iron deficiency anemia which is characterized by pallor, fatigue and weakness [251].

On the other hand, excessive accumulation of essential metals in human body can result in a number of other diseases. For example, excessive intake of copper can result in the inhibition of certain important enzymes which leads to vomiting, diarrhea, hemolytic anemia, anuria and cirrhosis. Moreover, the symptoms (including mild cognitive deterioration and clumsiness and liver disease) of Wilson's disease, which is also referred to as inherited copper toxicity[2], are caused by an accumulation of copper in human tissues and organs (especially in brain and liver). Miners can go mad with chronic exposure to manganese dust due to impaired motor skills and cognitive disorders caused by manganese poisoning [251].

Similarly, excessive intake of non-essential metals such as Pb (lead), Cd (cadmium) and Hg (mercury) can be toxic to human. Lead (Pb) poisoning works by the inhibition of some important enzymes which causes ineffective heme synthesis and subsequent microcytic anemia, a disease characterized by small red blood cells. Symptoms of mercury poisoning typically include sensory impairment (vision, hearing and speech), disturbed sensation and a lack of coordination. Inhalation of cadmium-containing fumes can result initially in metal fume fever but may progress to chemical pneumonitis and death [251]. Cadmium and several cadmium-containing compounds can also induce many types of cancer. It has been found that cadmium toxicity may result from the great similarity between cadmium and zinc so that cadmium (usually stronger than zinc in

[2] Wilson's disease is an autosomal recessive genetic disorder due to mutations in the ATP7B gene encoding a copper ATPase (see Table 1.3). In Wilson's disease, copper accumulates in tissues and this manifests itself with neurological symptoms and liver disease [209,251].

binding ability) competes with zinc for the binding of zinc-binding proteins (in particular, proteins that contain zinc finger protein structures) [123].

1.3.3 Metal Ion Homeostasis Systems

Metal ion homeostasis systems are highly regulated metabolic pathways used by living organisms to maintain metals at optimal concentration ranges, the values of which may vary much for different metals in different sorts of organisms. Moreover, the metal ion concentration in the cytoplasm of biological cell can be quite different from that in the extracellular fluid and from those in intracellular membrane-bounded compartments. For example, the following table shows a comparison of concentrations of metal ion macronutrients inside and outside a typical mammalian cell [5].

Table 1.2: Comparison of concentration values of four major metal ions on the two sides of the plasma membrane of a typical mammalian cell [Taken from Ref. 5]

Metal	Intracellular cytosolic concentration (mM)	Extracellular concentration (mM)
Na^+	5-15	145
K^+	140	5
Mg^{2+}	0.5	1-2
Ca^{2+}	10^{-4}	1-2

From this table, we can see that a typical mammalian cell maintains high gradients of Na^+, K^+ and Ca^{2+} (especially the gradient of Ca^{2+}) across the cell membrane. Such metal ion gradients are critical for the formation of membrane potential [126] and calcium signals.

1.3.3.1 Various Proteins Involved in Metal Ion Homeostasis

Metal ion homeostasis process involves coordination between ion uptake, distribution, storage and efflux. All these relevant tasks are accomplished by proteins and genes with intricate interactions which can be illustrated by schematic graphs and complex networks. For example, the following schematic graph Fig. 1.2 describes the zinc homeostasis system in yeast [133]:

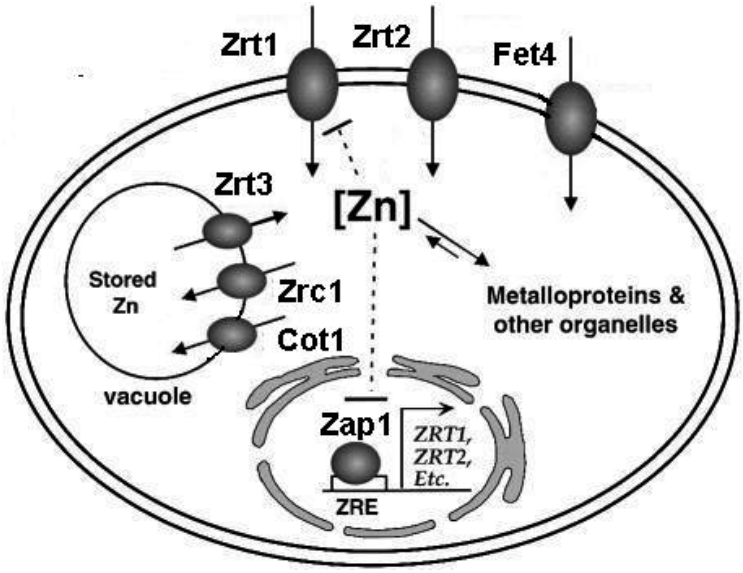

Figure 1.2. A schematic graph depicting the zinc homeostasis system in *Saccharomyces cerevisiae* (Modified after Fig. 9 in Ref. 133). Extracellular zinc ions are imported into the cell through Zrt1, Zrt2 and Fet4; the cytoplasmic zinc can be stored in metalloproteins, transported into the vacuole for storage through Zrc1 and Cot1 or transported to other organelles; the stored zinc in the vacuole can supplement the cytoplasmic zinc through Zrt3 when necessary; Zap1 is the critical regulatory protein which can senses the level of cytoplasmic zinc and activate a number of proteins including Zrt1, Zrt2, Zrt3, Fet4, Zrc1 and itself under zinc-limiting conditions[3]; excessive cytoplasmic zinc results in the inactivation of Zrt1 through endocytosis and vacuolar degradation; the cytplasmic trafficking of zinc may involve chaperone-like proteins. ZRE: zinc-responsive elements.

In many cases, due to the evolution, the various proteins which accomplish a certain task in a specific metal ion homeostasis process in different organisms are homologous in both sequence and function. For example, an incomplete list of homologous proteins that play specific roles in calcium, copper and zinc homeostasis in bacteria, yeast, plant and human are shown in the following Table 1.3:

Table 1.3: Homologous proteins that affect calcium, copper and zinc homeostasis in bacteria, yeast, plant and human [102, 246, 249]

Metal	Bacteria	Yeast	Plant	Human	Description
Ca		Cch1	OsTPC1	CACNA1A	Voltage-dependent channel (α1A subunit)
		Pmc1		PMCA1a	Ca^{2+} ATPase
		Pmr1		SPCA1	Ca^{2+} ATPase
		Vcx1	CAX1,		H^{+}/Ca^{2+} antiporter

[3] Actually the regulation of Zap1 on Zrt2 is complicated: Zrt2 is induced by Zap1 under conditions of mild zinc limitation but then repressed by Zap1 under more severe zinc-limitations.

			CAX5		
		Rcn1	RCN1	MCIP1, MCIP2, MCIP3	Calcineurin regulatory protein
		Mck1	AT5G14640	GSK3β	Protein kinase
		Crz1		NFATc2	Calcineurin-dependent transcription factor
	CALM_KLULA	Cmd1	CAM6	CALML3	Ca^{2+} sensor (CALML3 is Calmodulin-like protein 3; the rest three including CAM6, Cmd1 and CALM_KLULA are calmodulin proteins)
			CAM7	CAMI	Calmodulin (Ca^{2+} sensor)
			CAM2	CAMII	Calmodulin (Ca^{2+} sensor)
			CAM3	CALM3	Calmodulin (Ca^{2+} sensor)
		Cna1		CNA1/CALN	Catalytic subunit of calcineurin (protein phosphatase)
		Cnb1		CNBII	Regulatory subunit of calcineurin (protein phosphatase)
Cu	CopA	Ctr1-Ctr3	COPT1	hCtr1/hCtr2	Copper transporter
		Atx1	CCH	Hah1p	Copper chaperone
	CopZ	Ccs1	CCS1	CCS	Copper chaperone
		Cox17		hCox17	Copper chaperone
		Ccc2	RAN1, PAA1	ATP7A, ATP7B	Copper ATPase
		Sco1, Sco2		SCO1, SCO2	Copper-binding protein
	CueO	Fet3		Ceruloplasmin, Hephaestin	Multicopper oxidase
Zn		Zrt1-Zrt3	ZIP1-ZIP12	hZIP1-hZIP5	Zinc transporter
		Cot1		ZNT1	Zinc transporter
			ZAT1	ZNT2	Zinc transporter
			MTP4	ZNT4	Zinc transporter
			AT2G04620	ZNT7	Zinc transporter
		Zrc1		ZNT8	Zinc transporter
		Sod1	CSD1	hSOD1	Superoxide dismutase

Moreover, the same organism may possess homologous proteins functioning in the homeostasis systems of different metal ions. For example, *Bacillus subtilis* contains three homologous transcriptional regulator proteins (Fur, PerR, and Zur) which play central regulatory roles in iron and zinc homeostasis systems [149]. *E. coli* possesses two important homologous proteins (ZntR and Mer) which are critical metalloregulators in zinc homeostasis and mercury detoxification systems [182]. Another interesting phenomenon worthy of notice is that a specific kind of protein may play several roles in different metal ion homeostasis systems in a single organism. For example, Pmr1 in yeast is a high affinity P-type ATPase for transporting Mn^{2+} as well as Ca^{2+} into Golgi [246,249]. Sod1, CSD1 and hSOD1 function as superoxide dismutase in both iron and copper homeostasis systems in yeast, plant and human, respectively [249]. Metallothionein (MT) is a family of cysteine-rich proteins which functions as binding proteins for the buffering of both essential heavy metals such as zinc and copper and non-essential heavy metals such as cadmium, mercury and silver. Metallothionein proteins are widely found in all kinds of organisms including prokaryotes, yeast, plant and animals [249,251].

Finally, different organisms may use proteins which are homologous in function but not in sequence to play similar roles in specific metal ion homeostasis systems. For example**,** Zap1 and MTF1 are zinc-responsive transcription factors which function similarly (although they are not homologues in sequence) in zinc homeostasis systems in yeast and human [182]. Similar zinc-responsive transcription factors have been found in fungi, mammals, fish, and possibly plants, suggesting that the universal importance of transcriptional control of genes involved in zinc homeostasis [182].

1.3.3.2 Regulated Membrane Ion Transport

Regulated membrane ion transport constitutes the major scheme used by the biological cell to maintain optimal concentrations of metal ions in its cytosol. The lipid bilayer of cell membranes serves as a barrier to the passage of most polar molecules, including metal ions [5]. There are numerous ion transport proteins (including channels and transporters) on the cell membrane to transfer metal ions across the membrane. The regulations on membrane ion transport can be achieved by regulating the membrane concentration or the opening probability of relevant transport proteins.

The regulation on the membrane concentration (i.e., the number) of ion cannels or transporters can be accomplished through transcriptional, translational, posttranslational or biochemical binding mechanisms. For example, in zinc homeostasis system in *E. coli*, the zinc influx through zinc transporter ZnuABC and the zinc efflux through zinc ATPase ZntA are regulated respectively by Zur and ZntR through transcriptional regulations [172]. In calcium homeostasis in yeast, the regulations of calcineurin on Pmc1 and Pmr1 through Crz1 are transcriptional whereas the regulation of calcineruin on Vcx1 is supposed to be posttranslational [50,51,132]. Another example of posttranslational regulation can be found in the zinc homeostasis system in yeast, where high intracellular zinc causes the inactivation of zinc transporter Zrt1 through endocytosis and the subsequent degradation of Zrt1 in the vacuole [133]. Regulation by biochemical binding

can be illustrated by the competitive inhibition on the availability of binding sites of transport proteins for a specific metal ion (e.g., Ca^{2+}) by other similar ions (e.g., Mg^{2+}).

Regulations on the opening probability of the ion transport proteins are even more common. For example, in mammalian calcium homeostasis systems, the opening probability of IP_3R proteins on the mammalian endoplasmic reticulum (ER) is regulated both by the cytosolic calcium concentration and IP_3 concentration [57,69]. The opening probability of voltage-gated ion channels which play crucial role in excitable neuronal and muscle tissues is regulated by the membrane potential [69,105,154]. It has been reported that the opening probability of some L-type calcium channels are dynamically regulated by the calcium-bound calmodulin binding [243].

1.3.3.3 Other Strategies of Maintaining Homeostasis

Biological cells use a diverse range of strategies to maintain intracellular metal ion concentrations within an optimal range. Besides regulated membrane transport which is related with the regulations imposed on the metal ion uptake and efflux, cells also impose regulations on the storage and distribution processes to help achieve homeostasis [92,110,137,142,182,191,209]. These regulations can be realized through transcriptional, translational, post translational or biochemical binding mechanisms. For example, intracellular Fe^{2+} in *E. coli* represses (through Fur) the transcription of a small RNA (sRNA) named as RyhB, which facilitates the degradation of mRNAs encoding iron-using proteins [191]. This example exemplifies a combination of two control mechanisms: a transcriptional regulation on the expression of RyhB by Fur and a posttranscriptional regulation on the Fe-proteins by RhyB. It turns out later that sRNAs repressing iron-using proteins might be a quite common mechanism in bacteria because functional homologues of RhyB have been found in many other bacteria such as *P. aeruginosa* and *P. putida.* Regulations through translational mechanisms can be illustrated by the control of translation and RNA stability by iron-regulatory proteins in various organisms. For example, Cth2 is a zinc finger RNA-binding protein in yeast which regulates the mRNA stability of iron-using proteins in response to iron depletion [142].

An even more novel strategy to achieve homeostasis is to impose regulations on the regulatory proteins. The autoregulations of Zap1 in the yeast zinc homeostasis system and CopY (repressor) in the copper homeostasis system of *E. hirae* provide good examples [25,66,77,202]. However, there are more complicated cases. For example, in *E. coli*, ZntR is a metalloregulatory protein activating the zinc efflux ATPase ZntA. Recent experiments have shown that the binding of zinc to ZntR can reduce its degradation so that more ZntR molecules can be available for activating the zinc efflux pathway [172]. Another interesting example is that in yeast calcium homeostasis system, the activity of calcineurin is modulated by Rcn1 in a biphasic way (i.e., Rcn1 stimulates calcineurin at low concentrations and inhibits calcineurin at high concentrations) [100].

The great variety of possible mechanisms provides biological cells freedom of selecting suitable strategies to achieve homeostasis. It is quite common that a certain cell uses a combination of various strategies in a specific metal ion homeostasis system. For

example, as shown in Fig. 1.2, yeast cell uses both transcriptional control mechanisms to regulate membrane ion transport and the expression of the regulatory protein itself (through the transcriptional regulator Zap1) and posttranslational control mechanism to regulate the influx through Zrt1 to achieve zinc homeostasis. The iron homeostasis system in yeast exemplifies another good combination of several control mechanisms: Aft1 and Aft2 are iron-responsive transcription factors which activate the transcription of iron transport proteins and Cth2 during iron deprivation [142]. These transcriptional control mechanisms work together with the translational regulation of Cth2 on iron-using proteins to help the cell to maintain optimal iron concentration.

1.3.4 Metal Ion Signaling Systems

One of the basic characteristics of life is that living organisms can respond to stimuli. When a biological cell receives extracellular stimuli, it relies on diffusible signaling molecules named as intracellular second messengers (e.g., Ca^{2+}, IP_3, cAMP, NO, etc.) to activate effector proteins within the cell to exert a cellular response [251]. It has been well established for decades that Ca^{2+} is the most ubiquitous and versatile second messenger [20-22] whereas the identity of Zn^{2+} as a novel intracellular second messenger has been recently uncovered [238]. Moreover, the molecular identification of the extracellular calcium-sensing receptor (CaR) opens the possibility of that Ca^{2+} may function as a first messenger as well [106]. In the nervous system, Zn^{2+} is now regarded as neurotransmitter and functions as a transcellular and transmembrane signaling factor [219].

1.3.4.1 Versatility and Universality of Calcium Signaling

The novelty of calcium signaling was firstly demonstrated by a “mistaken” experiment conducted by British clinician and pharmacologist Sidney Ringer (1836-1910) who used London tap water (instead of distilled water) containing calcium at nearly the same concentration as the blood to make a saline medium for suspending isolated rat hearts [39]. The beating of the hearts became progressively weaker and eventually stopped when the tap water was replaced by distilled water. Since then, the mysterious fog covering the iceberg of calcium signaling was gradually unveiled and now calcium is regarded as the most versatile carrier of signals regulating a myriad of important processes both inside and outside the cells [20-22,39,98,124,140].

The life of animals begins with a wave of calcium. When the sperm interacts with the egg, Ca^{2+} wave and subsequent sustained Ca^{2+} oscillations are initiated to trigger the developmental program (see Fig. 1.3a) [39,186]. During the embryogenesis, Ca^{2+} signaling controls the cleavage process (see Fig. 1.3b), contributes to body polarity and pattern formation and is critical for coordinating the motility of the cells. In later development, the differentiation of specific cell types (including muscle, neuron, heart and eyes, etc.) is again controlled by calcium (see Fig. 1.3c-d) [20-22,140,231]. In addition to playing critical roles in animal fertilization and development, calcium signaling is also important for the cell differentiation process and for the function of many different types of cells [20,126,138]. As shown by the experiment of Sidney Ringer,

calcium signals are required for cardiac muscle contraction. It has been recently found that calcium signaling controls the growth of heart as well [224]. In the nervous system, calcium signaling plays a pivotal role in receiving and transmitting neuronal signals, in controlling the release of neurotransmitters (e.g., Zn^{2+}), as well as in regulating excitability and the changes that underlie learning and memory [20-22]. Recent experimental discoveries have uncovered calcium as a central cell death regulator which triggers and modulates the apoptotic cell death process [20,162].

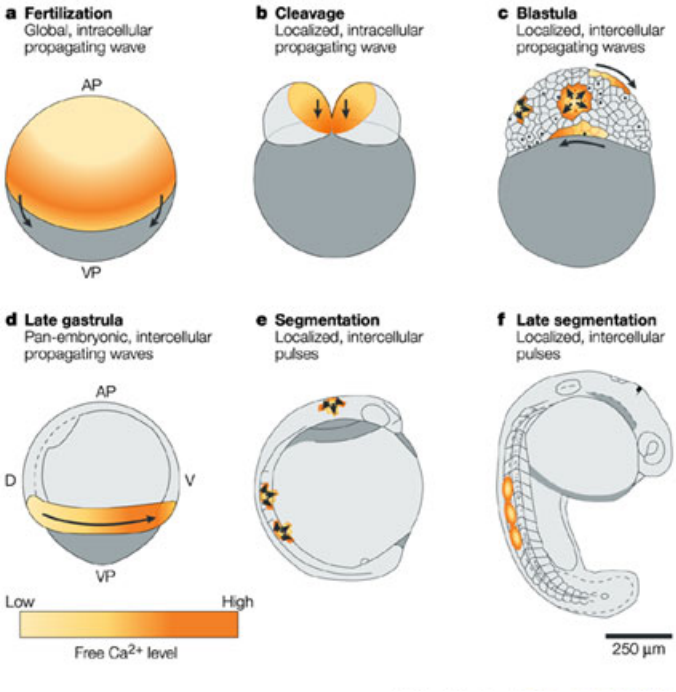

Figure 1.3. Various forms of calcium signals in embryogenesis. Please note the transition from a and b | intracellular, to c | localized intercellular, to d | pan-embryonic intercellular, and then back to e and f | localized intercellular Ca^{2+} signaling. AP: animal pole; D: dorsal; V: ventral; VP: vegetal pole (this figure is taken from Ref. 231).

In plants, calcium signals function in most aspects of growth and development including the response to drought, cold and salt stresses, mechanical wounding, symbionts and pathogens [94,184,185]. Ca^{2+} signals are implicated in various responses to plant hormones (such as abscisic acid and auxin) and have been shown to play an essential role in pollen tube growth and fertilization. In yeast, as we will show in Chapter 2 and 3, there exists an elaborate calcium homeostasis/signaling system whose components (except H^{+}/Ca^{2+} antiporter) have all functionally retained in animal cells (see Table 1.3) [174]. Ca^{2+} signals are critical in the response of yeast cell to various stimuli such as pheromone, hypertonic shock, hypotonic shock, etc [17,108,150,165].

Compared with its well-established signaling role in eukaryotes, the role of calcium in prokaryotes is more elusive [60]. Calcium ions have been found to be involved in the maintenance of bacterial cell structure, motility, transport and cell differentiation processes such as sporulation, heterocyst formation and fruiting body development. The characterization of calcium-binding proteins and the identification of other relevant factors suggest the possible existence of calcium signal transduction in bacteria [60].

1.3.4.2 Intracellular Calcium Signaling

Calcium homeostasis is the basis of calcium signaling. As mentioned before, a biological cell maintains an extremely high gradient of Ca^{2+} concentration across the cell membranes through the functioning of its calcium homeostasis system. Extracellular stimuli cause the change of the opening probability of various calcium transport proteins (mostly channels) on the membranes and results in sudden calcium influx into the cytosol due to the extremely high gradient. Calcium signaling depends on the increased levels of cytosolic Ca^{2+} concentrations derived either from sources outside the cell or within the organelles such as ER (in mammalian and plant cells) and/or the vacuole (in plant and yeast cells). A calcium signaling network consists of numerous components (the Ca^{2+} signaling toolkit) which can be grouped into four functional units as described in Fig. 1.4a [21-22].

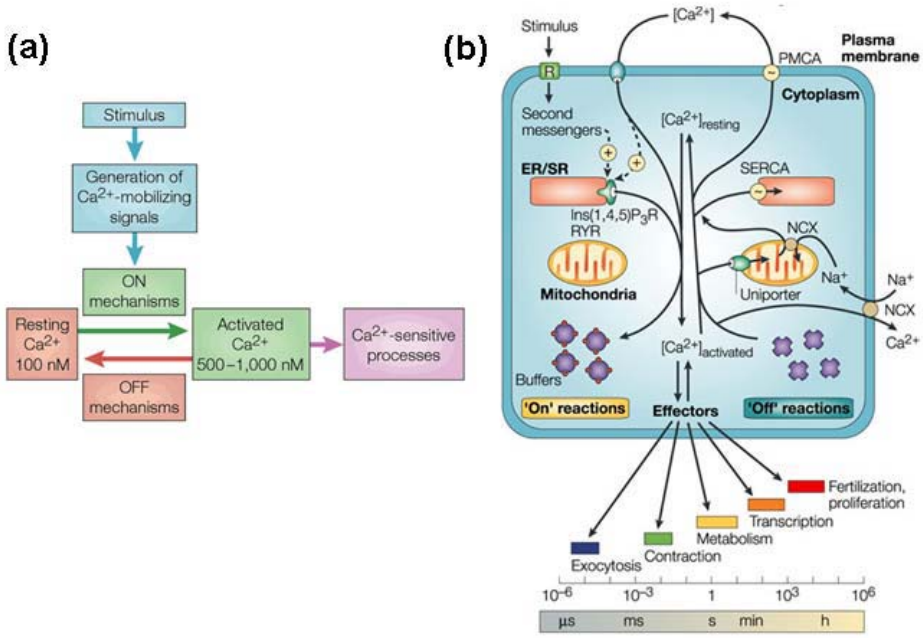

Figure 1.4. The Functional Units and Dynamics of Calcium Signaling. (a) The four functional units (colored as blue, green, purple and pink, respectively) of the Ca^{2+} signaling network: (i) Extracellular stimuli triggers the signaling process by generating Ca^{2+}-mobilizing signals. (ii) Ca^{2+}-mobilizing signals activates the ON mechanisms through which cytosolic Ca^{2+} is fed. (iii) Numerous Ca^{2+}-sensitive processes are stimulated by Ca^{2+} signals (this graph is taken from Ref. 22). (iv) The resting state of cytosolic Ca^{2+} concentration is restored through the functioning of the OFF mechanisms. (b) Calcium signaling dynamics and homeostasis in animal cells (this graph is taken from Ref. 21).

A more detailed schematic graph depicting the dynamical process of calcium signaling and homeostasis in animal cells is shown in Fig. 1.4b. From the top left corner of this graph, we can see that extracellular stimulus acts on the receptor protein and induces both the entry of external Ca^{2+} through calcium channels and the formation of second messengers such as IP_3 molecules which will act as Ca^{2+}-mobilizing signaling molecules to activate the Ins(1,4,5)P_3R channels and the ryanodine receptor (RYR) on the ER membrane. The opening of channels on both plasma membrane and ER membrane constitutes the ON mechanisms which result in the rise of cytosolic calcium level with the occurrence of the 'On' reactions. Most of the rushed-in cytosolic Ca^{2+} (shown as red dots) is bound to buffers, whereas a small proportion binds to the effectors that activate various cellular processes that operate over a wide temporal spectrum. The OFF mechanisms (see Fig. 1.4a) are composed of pumps and exchangers including the sarco(endo)plasmic reticulum Ca^{2+}-ATPase (SERCA), the Na^{+}/Ca^{2+} exchanger (NCX) and the plasma-membrane Ca^{2+}-ATPase (PMCA) and Uniporter on the membrane of

mitochondria which sequester Ca^{2+} into the organelles or outside the cell and promote the recovery of the resting state[4] [21-22].

1.3.4.3 Extracellular Calcium Signaling

The well-established identity of calcium as the most versatile second messenger has vastly eclipsed its role as a first messenger. However, it seems much more natural if we consider the possible toxicity of calcium. The necessity of maintaining calcium homeostasis in the extracellular body fluid requires a detector to detect the extracellular calcium concentration and this role is played by CaR, a G-protein-coupled receptor which has now been found to be expressed in all major organs such as brains, pancreas, blood vessels, parathyroid gland, thyroid gland and heart [106,200,207]. CaR functions in the parathyroid and thyroid glands to tightly regulate blood calcium levels through regulating the secretion levels of parathormone (i.e., PTH, a hormone which stimulates calcium release from bone, calcium absorption by the intestine and reabsorption by the kidney) and calcitonin which can antagonize the effects of PTH [68,106]. It has been suggested that the CaR (also named as CaSR) may function in the adult brain by modifying the architecture of dendrites in response to changes in synaptic activity [227]. The discovery of CaR in key components of the cardiovascular system indicates that the CaR may modulate myogenic tone (i.e., pressure-induced constriction) through activation of nitrogen oxide (NO) production and K-channels in the vascular tree, thus making calcium a first messenger that modulates the system [200]. It has been experimentally shown *in vitro* that an intracellular calcium signal may induce generation of an extracellular calcium signal that is sensed by the CaR on neighbouring cells or even on the same cell [200]. Such novel mechanism provides an alternative strategy for the propagation of calcium signals across the cells other than using gap junctions as found in neuronal cells and may underlie the formation of localized intercellular calcium signals in embryogenesis and development (see Fig. 1.3).

1.3.4.4 Calcium Signaling Toolkit

The incredible versatility of calcium signaling arises through the use of an extensive Ca^{2+}-signalling toolkit composed of receptors, transducers, channels, pumps and exchangers, calcium buffers, calcium effectors, calcium-sensitive enzymes and processes [21-22,94]. For example, according to Harper *et al.* (2005) [94], *Arabidopsis thaliana* (a model plant) is predicted to have a large number of calcium transport proteins (including 20 cyclic nucleotide-gated channels, 30 glutamate receptors, a single two-pore Ca^{2+} channel, 14 Ca^{2+} pumps and 12 potential H^+/Ca^{2+} exchangers) and a large number of Ca^{2+}effector proteins (including 9 calmodulins, ~50 calmodulin-like proteins, 7 annexins and 10 calcineurin B-like proteins).

The signaling toolkits in different organisms may not only share many features as partially shown in Table 1.3), but also have important differences. For example, in mammalian cells, there are hundreds of G-protein-coupled receptors (including

[4] Please note that during the 'off' reactions, the rapidly sequestered Ca^{2+} by mitochondrial uniporter is released more slowly back to the cytosol by Na^+/Ca^{2+} exchanger (NCX) on the mitochondrial membrane.

bradykinin receptors B_1, B_2 and CaR) and 58 known tyrosine-kinase-linked receptors whereas *A. thaliana* has no tyrosine-kinase-linked receptors and only one identified (GCR2) and one putative (GCR1) G-protein-coupled receptor. Unlike animals, land plants in general do not have protein kinase C, stereotypical calmodulin dependent protein kinases (CaMKs) or calcineurin (see Table 1.3). Instead, they have Ca^{2+}-dependent protein kinases (CDPKs), chimeric Ca^{2+} and calmodulin-dependent protein kinases (CCaMKs) and CDPK-related kinases (CRKs), etc., some of which are regulated by Ca^{2+}-binding proteins [94].

1.3.4.5 Spatial and Temporal Aspects of Calcium Signaling

As mentioned before, repetitive intracellular waves of calcium trigger the developmental program of animals. In animals and plants, calcium signals may appear in various forms such as intracellular localized signals (blips, quarks, puffs and sparks) and intercellular or intracellular global signals (transients, pulses, oscillations and waves) [20-22,231]. For example, the schematic graph shown in Fig. 1.3 describes the different forms of calcium signals used in six developmental stages of a representative embryo (e.g., a zebrafish) [231].

The spatial organization of calcium signaling toolkit (especially channels) may have influence on the formation of various forms of Ca^{2+} signaling. Intracellular Ca^{2+} blips, quarks, puffs, or sparks represent elementary Ca^{2+} signaling units which are thought to reflect the local opening of individual (or small groups of) Ca^{2+}-release channels on the ER membrane. Sufficiently strong and persistent extracellular stimulus may result in regenerative Ca^{2+} wave across the cytoplasm due to the propagation of the localized signals. Single Ca^{2+} wave results in pulses and transients whereas repetitive Ca^{2+} waves lead to oscillations. It is believed that both the waves and the oscillations depend, in part at least, on a combination of positive and negative feedback regulations by cytosolic Ca^{2+} on the calcium-releasing channels on ER (IP_3Rs and RyRs): the released Ca^{2+} initially stimulates more Ca^{2+} release, a process known as Ca^{2+}-induced Ca^{2+} release (CICR), whereas later, high cytosolic Ca^{2+} inhibits further release [20-22].

As shown in Fig. 1.4b, the processes regulated by calcium signaling operate over a wide temporal spectrum. In the case of fast signaling events such as synaptic transmission or cardiac contraction, the effector systems respond to calcium signals within μs to ms range whereas in the case of slower events (e.g., oocyte activation at fertilization), calcium signals (the repetitive calcium waves in the case of fertilization) may last as long as several hours to fully accomplish their tasks [21].

1.3.4.6 Calcium Signature Hypothesis vs. Chemical Switch Hypothesis

The central question in the field of calcium signaling is related with its specificity. How can calcium signaling link different extracellular signals to a myriad of cellular responses?

Calcium signature hypothesis assumes that calcium signals are encoded in the temporal and spatial nature and the amplitude of cytosolic calcium concentration changes (the

calcium signature), which are later decoded by the effectors [20,169,217]. It has been experimentally demonstrated that in mammalian cells, Ca^{2+} signals varying in amplitude, duration, frequency, and localization may result in differential responses. For example, changes in the amplitude and duration of a Ca^{2+} signal in B lymphocytes can induce differential activation of transcription factors [59]. Experiments conducted by Li *et al.* (1998) demonstrated that the degree of gene expression can be determined by the frequency of Ca^{2+} spikes via nuclear factor of activated T-cell (NFAT) [128]. It has been experimentally shown that Ca^{2+}/calmodulin-dependent protein kinase II (CaMKII) and protein kinase C (PKC) are able to decode frequency-modulated Ca^{2+} signals which widely exist in many cells including hepatocytes, salivary glands, endothelial cells and smooth muscle cells. In wildtype *Arabidopsis* guard cells, Allen *et al.* (2000) demonstrated that calcium signature (in the form of oscillations) is produced in response to extracellular calcium and H_2O_2 to specifically direct stomatal closure and such signature can be mimicked by artificially produced calcium oscillations [8,9].

In plant calcium signaling field, however, the dogma of calcium signature has aroused many doubts and debates [170,189]. For example, Scrase-Field *et al.* (2003) argued that calcium may be merely an essential chemical switch in signaling and that calcium signature hypothesis describes the exception (e.g., in the just mentioned guard-cell signaling) rather than the rule. They enumerated experimental evidence suggesting that signal specificity can be the responsibility of some signaling components other than calcium [189].

1.3.4.7 Zinc Signaling

The very recent exciting discovery of the existence of intracellular zinc wave by Yamasaki *et al.* (2007) has provided evidence showing that zinc is a novel intracellular second messenger [238]. Their experiments demonstrated that a zinc wave was induced several minutes after mast cells were stimulated by an extracellular stimulus called as FcεRI cross-linking. This zinc wave originated from the perinuclear region that includes the ER and was dependent on both calcium influx and MAPK/ERK kinase (MEK) activation. The role of the zinc wave is supposed to be to regulate the duration of MAPK activation, inhibit tyrosine phosphatase activity and modulate signaling quantity of the relevant events [238].

Similar as Ca^{2+}, Zn^{2+} has been implicated as an important messenger in a number of cellular signaling pathways in animals, including those involved in synaptic transmission, cell proliferation and apoptosis. It has been noticed for decades that Zn^{2+} plays some enigmatic role in the central nervous system. Experimental observation has shown that Zn^{2+} is accumulated by specific neurons into synaptic vesicles and can be released by stimulation in a Ca^{2+}-dependent manner [62,219]. Now Zn^{2+} is regarded as a neurotransmitter modulating both excitatory and inhibitory neurotransmission. The very recent hypothesis about the existence of a specific zinc-sensing receptor (ZnR) may explain some interesting phenomena, for instance, the application of Zn^{2+} to epithelial cells in culture or to PC-3 (Human prostate cancer cell line) cells leads to an increase in intracellular Ca^{2+} concentration via the IP_3 pathway [62,97]. The molecular identification

of ZnR in the future will eventually establish zinc's identity of a first messenger. Because extracellular Zn^{2+} promotes cell growth in numerous cancer cell types (e.g., HT-29, PC-3 and NIH3T3 fibroblasts) by activating and regulating major signaling pathways (e.g., MAP kinase pathway), the thorough understanding of zinc signaling in these cells will help devise therapeutic strategies to attenuate tumor growth and cure related diseases [62].

1.4 Feedback Control Theory and Network Motifs

The biological cell is a collection of protein machines full of feedback regulations. The mysterious ability that a biological cell can keep a relatively stable internal environment in an ever-shifting extracellular environment relies on a variety of negative and positive feedback controls embedded in its complicated intracellular networks composed of proteins, genes and metabolites [5,32,74,213,220]. Negative feedback controls constitute the central scheme of metal ion homeostasis [241]. For example, *E. coli* cell employs transcriptional negative feedback control mechanisms to regulate the uptake and efflux of zinc ions whereas in yeast cells [172], the negative feedback control pathway through calcineurin plays an important role regulating the long-term cytosolic calcium homeostasis [132].

1.4.1 A Bit of History of Feedback Control

The primary motivation for feedback control in ancient time was the need for the accurate determination of time. As early as about 270BC, the Greek inventor and mathematician Ktesibios (285-222BC) invented an improved water clock (a clepsydra) operated by means of a regulated flow of water into a tank where the water level is measured by a float and fed back for the regulation of the inflow. Thus the water level in the tank is kept as a constant which causes a constant flow through a tube at the bottom into a second tank whose water level can be measured to determine the time elapsed [220,251].

The concept of feedback was later used by Charles Darwin (1805-1882) who devised the theory that feedback over long time periods is responsible for the evolution of species. Vito Volterra (1860-1940) used this concept to explain the balance between two populations of fish in a closed pond [251]. However, the most influential person in the history of feedback control theory is Norbert Wiener (1885-1964) who introduced the fruitful concepts of positive and negative feedbacks in biology and founded the theory of cybernetics [233]. It is very worth to mention that Wiener's work owed much to Walter Cannon (1871-1945) who developed the concept of homeostasis and popularized it in his book "*The Wisdom of the Body"*[38]. Cannon noticed the remarkable stability of numerous blood properties in mammals in the face of enormous environmental change and termed this process as homeostasis.

1.4.2 Basic Feedback Control System

As shown in Fig. 1.5, the most elementary control system consists of three components: a plant (the object to be controlled), a sensor and a controller. The output of the plant (i.e.,

$y(t)$) is measured by the sensor whose output (i.e., $b(t)$) is compared with a reference input (i.e., $r(t)$) and then the deviation (i.e., $e(t)$) is fed back to the plant through a controller [61,127]. However, in many complex feedback systems as those considered in this thesis, the reference signal is usually hidden or even absent.

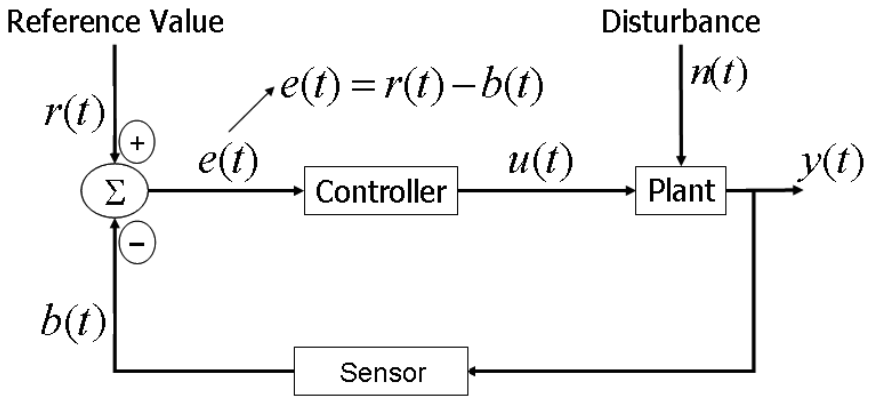

Figure 1.5. Elementary control system. $y(t)$: the plant output and measured signal; $u(t)$: the plant input (i.e., actuating signal); $n(t)$: the external disturbance; $b(t)$: sensor output; $r(t)$: reference or command input; $e(t)$: error or deviation (this figure is based on Ref. 61).

One of the first mathematical analysis of control systems was the frequency-domain approach which is based on Laplace transformation.

$$\mathbf{L}[f(t)] = F(s) = \int_0^\infty f(t)e^{-st}dt \tag{1.1}$$

The central concept of frequency-domain approach is that of *a transfer function* (defined as $Y(s)/U(s)$ where $Y(s)$ and $U(s)$ denote the Laplace transform of the output and the input of the plant, respectively) which turns out to embody the *transfer characteristics* of the system. However, this approach is appropriate for linear time-invariant systems, especially for single-input/single-output systems where the graphical techniques are very efficient [61,251]. As we will see later, most control systems considered in this thesis are non-linear and time-variant, so we will not discuss too much the frequency-domain approach here.

1.4.3 Negative Feedback

Negative feedback is the basic mechanism by which systems, whether mechanical, electrical, or biological, maintain their equilibrium or homeostasis. In his famous book "Cybernetics", Norbert Wiener defined negative feedback as "the feedback (which) tends to oppose what the system is already doing" [233]. In another word, negative feedback

counteracts the effect of the stimulus, thus stabilizes outputs and enables biological systems to operate with resilience.

In many other cases, negative feedback can also result in oscillations. Norbert Wiener discussed in detail how a simple linear negative feedback can result in an oscillation whose amplitude does not increase or even an unrestrained and increasing oscillation (i.e., catastrophe) [233]. Negative feedback has been proposed to be the underlying basic mechanism responsible for various oscillations found in protein synthesis, MPF activity, MAPK signaling pathways, and circadian rhythms [82,221]. However, there are more complex cases in which oscillations arise in systems containing both positive and negative feedbacks [114,188,139].

The blood calcium homeostasis model proposed by EL-Samad *et al.* (2002) gives a nice example of negative (so called proportional plus integral (PI)) feedback control, the block diagram of which is shown in Fig. 1.6 [68].

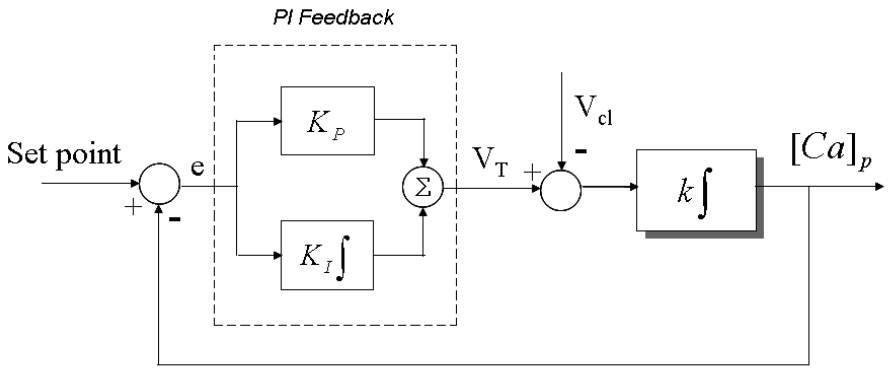

Figure 1.6. A block diagram of the blood calcium homeostasis model. This assumes that the studied system employs a PI (proportional + integral feedback) control mechanism. $[Ca]_p$: plasma calcium concentration; V_T : the total rate of calcium introduced into the plasma; V_{cl} : the calcium clearance rate from the plasma; k :the inverse of the total plasma volume; K_P : the real constant of the proportional feedback control; K_I the real constant of the integral feedback control; e : the error; set point: the desired value of $[Ca]_p$ (this figure is based on Ref. 68).

For more details on the physiological basis and the mathematical expression of this model, please see the original paper [68].

1.4.4 Network Motifs

Networks arise naturally in biology including gene regulation networks, protein networks, epidemiology networks, ecological food webs, etc [10,11]. In biological cells, metal ion homeostasis and signaling processes usually involve complex networks composed of genes, proteins and metabolites. For example, it is estimated that the calcium signaling

network in mammalian cardiac myocyte consists of tens to hundreds of components [224], part of which related to cardiac hypertrophy is described in Chapter 4 of this thesis. To uncover the design principle of such complex networks and understand their dynamics, a natural idea is to break them down into basic building blocks which are termed as 'network motifs' and study the specific functions of these motifs by using mathematical models [10,11,193].

Network motifs are defined as "patterns of interconnections that recur in many different parts of a network at frequencies much higher than those found in randomized networks" [10,193]. Since their first definition, a number of network motifs such as feedforward loop motif, autoregulation motif, feedback loop motif, single input module (SIM) motif and coupled feedback loop motifs have been found in sensory transcription networks, developmental networks, signal transduction networks and neuronal networks [10,114,115,193]. As we will see in Chapter 6 of this thesis, simillar motifs also exist widely in metal ion homeostasis and signaling networks, two examples of which are shown in Fig. 1.7.

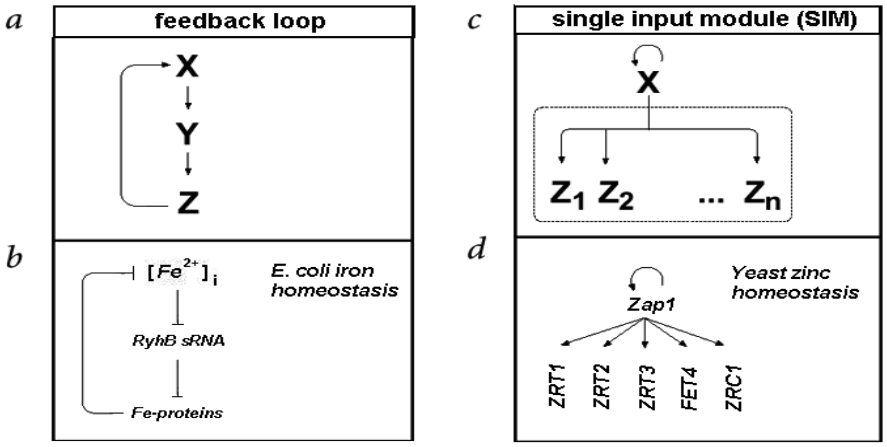

Figure 1.7. Two examples of network motifs. (a). In feedback loop motif, component X regulates component Y, Y regulate Z and Z regulates X. (b). An example of (negative) feedback loop motif found in *E. coli* iron homeostasis system. Cytoplasmic Fe^{2+} (i.e., $[Fe^{2+}]_i$) in *E. coli* represses (through Fur) a small RNA (sRNA) named as RyhB, which facilitates the degradation of mRNAs encoding Fe-using proteins (i.e., Fe-proteins) [142,191]. (c). In SIM motif, a single component X regulates a set of components $Z_1, Z_2, \ldots, Z_n$. X is usually autoregulatory. (d) An example of SIM motif found in yeast zinc homeostasis system. Zap1 is a zinc-responsive activator in yeast which activates the transcription of genes encoding cytosolic zinc influx transporters (ZRT1, ZRT2, ZRT3, FET4) and efflux transporter (ZRC1) (see Fig. 1.2).

1.5 Enzyme Kinetics and Nonlinear ODE Modeling

An enzyme is a substance that acts as a catalyst for chemical reactions. Enzymes reduce the needed activation energy of the reactions in living systems so that they can proceed at

rates that are useful to the cell [5,58,70,251]. In metal ion homeostasis and signaling systems, there are many enzyme catalyzed reactions. For example, the metal ion uptake and efflux processes are mediated by ion channels and transporters which can be regarded as enzymes. Calcineurin, which plays central role in calcium signaling in many organisms, is a special enzyme (phosphatase) which catalyzes the deposphoration of proteins such as Crz1 in yeast and NFAT in cardiac myocytes [208,224]. Thus basic knowledge about enzyme kinetics is quite necessary for modeling metal ion homeostasis and signaling systems.

1.5.1 Michaelis-Menten Kinetics

The kinetics of many enzyme-catalyzed reactions in solution has been proven to conform to the classic model of Michaelis and Menten as follows [58,178]:

$$E + S \underset{k_{-1}}{\overset{k_1}{\leftrightarrow}} ES \xrightarrow{k_2} E + P \tag{1.2}$$

Where in the first reaction, the enzyme (E) and the substrate (S) reversibly form an intermediate complex (ES), which produces the product (P) and releases the enzyme (E) in the subsequent second reaction. k_1 and k_{-1} denote the forward and the backward rate constants of the first reaction, respectively whereas k_2 denotes the rate constant of the second reaction which is assumed as irreversible.

This model can be expressed into 4 ODEs and we can further simplify the system by making the quasi-steady-state hypothesis (i.e., we assume that the concentration of ES is steady), the velocity of the enzyme reactions (denoted as v) can be calculated as follows:

$$v = \frac{V_{\max}[S]}{[S] + K_M} \tag{1.3}$$

Where $V_{\max}$ denotes the maximal velocity of the production, $[S]$ denotes the concentration of substrate and K_M denotes the Michaelis constant with dimensionality unit: mol l^{-1} (the concentration of substrate that leads to half-maximal velocity) which can be calculated as $\frac{k_2 + k_{-1}}{k_1}$.

1.5.2 Reversible Competitive Inhibition

The rate of an enzyme-catalyzed reaction can be reduced by inhibitors. Loss of enzyme activity may be either reversible, where activity may be restored by the removal of the inhibitor, or irreversible, where the loss of activity is time dependent and cannot be recovered during the timescale of interest [58]. In metal ion homeostasis and signaling

systems, reversible competitive inhibition happens quite frequently. For example, different metals such as (Mg^{2+} and Ca^{2+}) can compete for the binding of the same channel or transporter protein. Moreover, enzymes such as calcineurin usually have many target proteins which compete with each other for its binding. So some knowledge about reversible competitive inhibition is also very necessary.

Let us consider the case where two substrates S_1 and S_2 compete for the binding of the same enzyme E to produce different products (P_1 and P_2) as modeled by the following scheme:

$$E + S_1 \underset{k_{-1}}{\overset{k_1}{\leftrightarrow}} ES_1 \xrightarrow{k_2} E + P_1 \tag{1.4}$$

$$E + S_2 \underset{k_{-3}}{\overset{k_3}{\leftrightarrow}} ES_2 \xrightarrow{k_4} E + P_2 \tag{1.5}$$

If we assume that the rates of product formation are much slower than attainment of the equilibrium (i.e. $k_2 << k_{-1}$ and $k_4 << k_{-3}$), the rates of formation of P_1 and P_2 are given by

$$v_1 = \frac{V^1_{\max}[S_1]}{K^1_M(1+\frac{[S_2]}{K^2_M})+[S_1]} \tag{1.6}$$

and

$$v_2 = \frac{V^2_{\max}[S_2]}{K^2_M(1+\frac{[S_1]}{K^1_M})+[S_2]} \tag{1.7}$$

, respectively where $V^1_{\max}$ and $V^2_{\max}$ denote the maximal velocity of the production of P_1 and P_2. K^1_M denotes the Michaelis constant of S_1 which is called the inhibition constant of S_1 over S_2. Similarly, K^2_M denotes the Michaelis constant of S_2 which is also called the inhibition constant of S_2 over S_1. The effect of competitive inhibition on the velocity of the enzyme reaction is illustrated in Fig. 1.8.

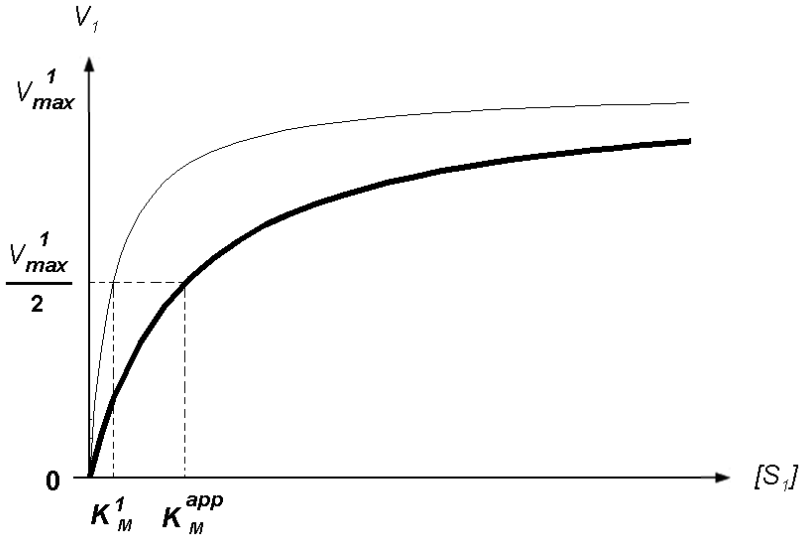

Figure 1.8. Effect of enzyme competitive inhibition. The solid curves depict the production velocity of P_1 as a function of the concentration of S_1 without inhibition (thin solid curve) and with inhibition (thick solid curve) from S_2, respectively. Without inhibition, the half-maximal velocity is reached when $[S_1] = K_M^1$ whereas with competitive inhibition from S_2, the half-maximal velocity is reached only when $[S_1] = K_M^{app} = K_M^1(1 + \frac{[S_2]}{K_M^2})$ where K_M^{app} denotes the apparent Michaelis constant of S_1.

1.5.3 Nonlinear ODE Modeling

As mentioned before, to a first approximation, ODEs provide a good framework for modeling the dynamics of biochemical reaction networks (see Secion 1.2.2) [120,213]. The immense variety of nonlinearities in living systems constitutes one of the major difficulties for modeling biological systems [113,139,141,213]. As we will see in later chapters, all the models presented in this thesis are nonlinear ODEs. In the case of intracellular metal ion homeostasis and signaling systems, the nonlinearity mainly arises from several sides:

(i). The nonlinear characteristics of the extracellular stimulus. For example, a very universal stimulus for the perturbation of metal ion homeostasis system is the step rise of extracellular ion concentration which is nonlinear.

(ii). The nonlinear interaction between the extracellular stimulus and the cell. For example, in Chapter 3, we can see that extracellular hypertonic shock can lead to the nonlinear evolution of the yeast cell volume.

(iii). The nonlinear transport characteristics of ion channels and transporters. For example, the uptake behavior of many metal ion transporters (and channels) can be modeled by the Michaelis-Menten kinetics which is essentially nonlinear.

(iv). The nonlinear interaction among proteins, genes and metabolites. For example, according to law of mass action, a reversible biochemical reaction ($A + B \rightleftharpoons C$, which means reactant A binds with reactant B to form product C) can be described by the following ODEs:

$$\frac{dC}{dt} = -\frac{dA}{dt} = -\frac{dB}{dt} = -r_b C + r_f AB \tag{1.8}$$

which naturally contain a nonlinear term AB (in the above equations, r_f and r_b denote the forward and backward rate constants, respectively). Similar nonlinearity arises in metal ion sensing process because of the binding of sensor proteins with the metal ions.

Nonlinear ODEs systems may have steady or unsteady (oscillating, chaotic, etc.) solutions [218]. In metal ion homeostasis systems, the steady state value of the variable in the ODEs solution denoting the regulated metal ion concentration is the most important because the task of all the components of the ion homeostasis system is just to keep this concentration value within an optimal range with no regard to various physiologically reasonable perturbations [123]. In the case of metal ion signaling systems, oscillating solutions can become quite important because of the widely existing phenomena of oscillations such as calcium oscillation and heart beating related to metal ion signaling [69,221]. Chaotic solutions may be useful (although rarely compared with steady and oscillating solutions) to mimic the abnormal behavior in pathological conditions, for instance, the cardiac arrhythmia.

1.6 Thesis Overview

The central question of this thesis is how to use mathematical models to simulate the complicated dynamics arising from metal ion (Ca^{2+} and Zn^{2+}) homeostasis and signaling systems in various organisms and to explain certain mutant behavior. First we will present a preliminary mathematical model which we developed for yeast calcium homeostasis, a work where all experimental data and some critical parameters are taken from literature (see Chapter 2). This concise model consists of 4 ODEs (ordinary differential equations) and is based on an assumption of quick feedback regulation on cytosolic Ca^{2+} sequestering transporters (Pmc1, Pmr1, etc.) through a gene expression feedback pathway through calmodulin (a ubiquitous Ca^{2+} sensor) and calcineurin (Ca^{2+} phosphatase). Simulation results show that our model can qualitatively reproduce the experimentally observed response curve of real yeast cell responding to step-like disturbance in extracellular Ca^{2+} concentration and correctly predict certain mutant behavior.

After the publication of this first model, we managed to establish good collaboration with Professor Kyle W. Cunningham of the Johns Hopkins University. We designed some new experiments which showed that the afore mentioned calcineurin-dependent expression feedback pathway has little or no effect on aequorin luminescence traces within the first few minutes of a Ca^{2+} shock. Therefore we built a new mathematical model that omits calcineurin-dependent feedback and instead includes rapid Ca^{2+}-dependent feedback inhibition of Ca^{2+} influx pathways which fit well new experimental data (see Chapter 3). Our simulation results strongly suggest the existence of a new calcium transporter M on the *yvc1 cch1* plasma membrane under hypertonic shock.

Next we move from a relatively simple organism (yeast) to a more complex organism (mice). Due to Professor Kyle W. Cunningham's suggestions, we have made detailed investigations into the possible mechanisms of the paradoxical, dual role of MCIP1 (Modulatory calcineurin-interacting protein 1) in mice cardiac hypertrophy. By including some recent experimental findings, we constructed a mathematical model composed of 28 ODEs to describe the complex underlying calcium-calcineurin signaling network (see Chapter 4). This complicated model can correctly predict the mutant ($MCIP1^{-/-}$) behavior under different stress such as PO (pressure overload) and CaN^{*} (activated calcineurin) overexpression.

Next we proceed to zinc homeostasis, although this time we study an even simpler organism - *E. coli*. The zinc homeostasis in *E. coli* involves a highly symmetrical structure which consists of repression on zinc influx through ZnuABC transporter by Zur ($\underline{Z}n^{2+}$ $\underline{u}$ptake $\underline{r}$egulator) and activation on zinc efflux via ZntA by ZntR (a zinc-responsive regulator). We constructed a mathematical model composed of 14 reactions which can quantitatively reproduce and interpret various reported results of the *in vitro* experiments of Zn^{2+} homeostasis system in *E. coli* (see Chapter 5) such as Zur-DNA binding curve, Zur and ZntR sensitivity curves, etc.

We finish the investigations on particular homeostasis/signaling networks and try to discover the general principles underlying metal ion homeostasis and signaling networks. We enumerate network motifs found in these systems such as the autoregulation motif, SIM (single-input module) motif, signaling cycle motif and coupled feedback motifs (see Chapter 6) and show the great variety of edge relations in those motifs. Particularly, we develop an ODE model and present simulation results to show the modulation on the properties of the signaling cycle motif by an inhibitor.

In the concluding Chapter 7, we summarize this thesis, discuss several interesting issues related to metal ion homeostasis and signaling systems based on our findings and indicate the directions of future work.

Chapter 2 The 1st Model for Yeast Calcium Homeostasis[5]

2.1 Introduction

As mentioned before, biological cells use highly regulated homeostasis system to keep a very low cytosolic Ca^{2+} level (see Section 1.3.3). The cytosolic Ca^{2+} concentration in normal yeast cell (*Saccharomyces cerevisiae*) is maintained in the range of 50-200 nM in the presence of environmental Ca^{2+} concentrations ranging from <1μM to >100mM [145]. This homeostatic process has two basic characteristics:

- "zero" steady-state error to extracellular stimuli, which means that cytosolic Ca^{2+} concentration is tightly controlled.
- Robustness of such "perfect" adaptation, which means that the system is relatively insensitive to specific kinetic parameters [119].

The underlying mechanism of this calcium homeostatic process involves the regulated internalization and sequestration of Ca^{2+} into a variety of intracellular compartments such as the vacuole, ER (endoplasmic reticulum) and Golgi apparatus through many membrane transport proteins (including channels and transporters) [4,27] (see Fig. 2.1a). Under normal conditions, extracellular Ca^{2+} enters the cytosol through an unknown Transporter X [132] whose encoded gene has not been identified yet. Cytosolic Ca^{2+} can be pumped into ER and Golgi through Pmr1 and can be sequestered into the vacuole through Pmc1 and Vcx1. Channel Cch1-Mid1 on the plasma membrane opens only under some abnormal conditions such as depletion of secretory Ca^{2+} [132], pheromone stimulation [150] and hypotonic shock [17]. Under the abnormal condition of extracellular hypertonic shock, the vacuole can release Ca^{2+} into the cytosol through Yvc1 [165]. Both the expression and function of *PMC1*, *PMR1* and *VCX1* are regulated by calcineurin, a highly conserved protein phosphatase that is activated by Ca^{2+}-bound calmodulin [51,111,223].

[5] This Chapter is based on: Jiangjun Cui and Jaap Kaandorp, Mathematical modeling of calcium homeostasis in yeast cells, *Cell Calcium* 39: 337-348, (2006).

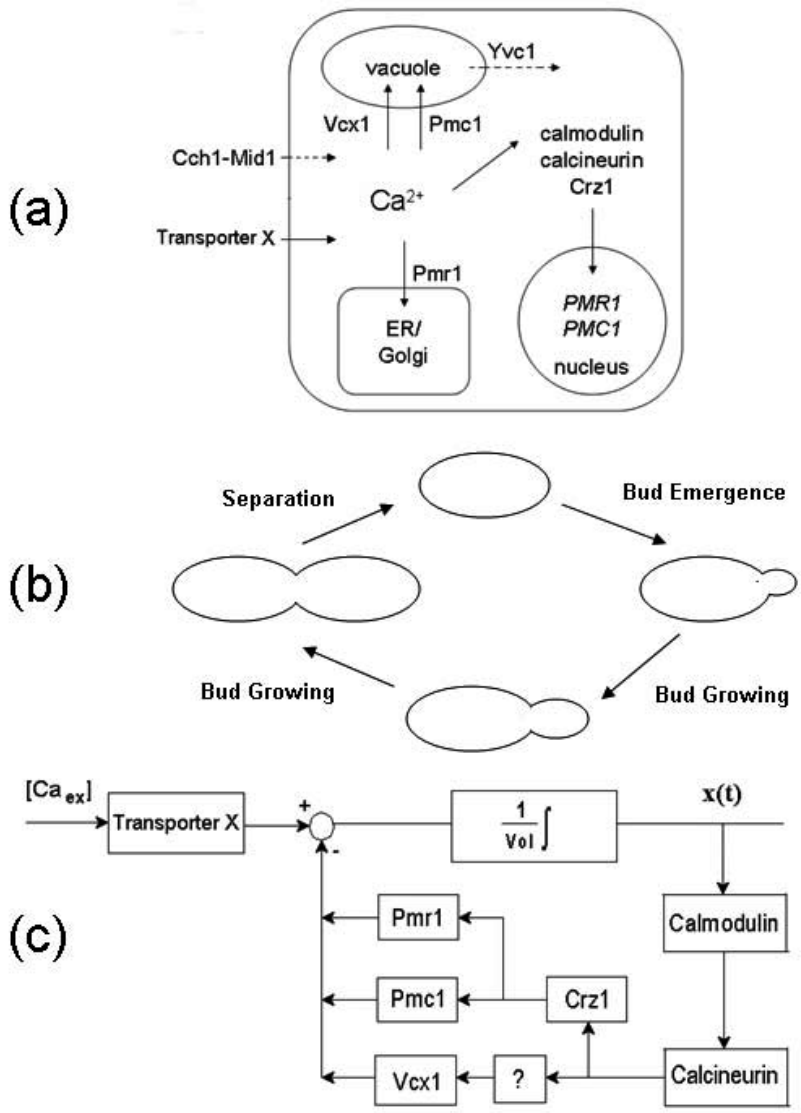

Figure. 2.1. Two schematic graphs and the block diagram of yeast calcium homeostasis system. (a) A schematic graph illustrating the protein level observations. (b) A schematic graph of the cell cycle of *Saccharomyces cerevisiae*. The bud emerges from a selected site of the cell and the further cell growth is restricted to the bud as the cell orchestrates the duplication and segregation of its organelles [173]. When the bud grows to nearly the same size of the mother cell, separation happens between the mother and daughter (i.e., the bud). (c) Control block diagram of calcium homeostasis under normal conditions. Extracellular Ca^{2+} enters the cytosol through an unknown Transporter X. The feedback control is added on Pmr1, Pmc1 and Vcx1 through calmodulin and calcineurin. Crz1 is a transcriptional factor and `?' denotes some unknown mechanism. $[Ca_{ex}]$ denotes extracellular

calcium ion concentration, $x(t)$ denotes cytosolic calcium ion concentration and Vol denotes the volume of the cytosol.

Calmodulin is a small Ca^{2+}-binding protein. In resting cells, calmodulin exists in the Ca^{2+}-free (also named apo-calmodulin) form. In response to the elevation of cytosolic Ca^{2+} level, calmodulin binds Ca^{2+} to activate a host of target proteins including calcineurin [53]. Structural analyses show that calcineurin is a heterodimer composed of a catalytic (A) subunit and an essential regulatory (B) subunit which have been highly conserved through evolution. Activated calcineurin increases the sequestering rates of Pmc1 and Pmr1 through a transcription factor Crz1. Activated calcineurin also decreases the sequestering rate of Vcx1 by regulating its synthesis [51,111].

Crz1 is a highly phosphorylated protein that can be dephosphorylated by activated calcineurin and this dephosphorylation promotes the translocation of Crz1 into the nucleus (to regulate the transcription of relevant genes including *PMC1* and *PMR1*) by increasing the efficiency of its nuclear import and down-regulating its nuclear export [29,208]. This mechanism of Crz1 translocation in yeast cells is strikingly similar to NFAT (nuclear factor of activated T-cells, a transcription factor that is also regulated by calcineurin) translocation in mammalian T-cells [29,161,208].

The so called conformational switch model was firstly proposed by Okamura *et al.* (2000), based on their detailed experimental study of NFAT1 phosphorylation states using a combination of mass spectrometry and systematic mutational analysis [161]. Later Salazar *et al.* [183] further developed this concept into a fully mathematical form which may generally apply to highly phosphorylated proteins. In the subsequent modeling we will use this mathematical model to simulate Crz1 translocation.

Saccharomyces cerevisiae is also called budding yeast and it grows by budding and dividing [173,230] (see Fig. 2.1b). The cell division cycle begins with a single unbudded cell. This cell buds, the bud grows to nearly the size of the mother cell, the nucleus divides, and the mother and daughter cells separate into two unbudded cells. The cycle then begins again for both of the cells. Intracellular organelles such as mitochondria, the vacuole, the Golgi, peroxisomes and the peripheral ER are all partitioned via specific mechanisms in this budding and dividing process [173,232] which eventually results in an exponential increase in the number of cells with a doubling time equal to the mean cell-division-cycle time [230]. The pattern of cell volume increase during cell growth is largely exponential [235]. Varying the Ca^{2+} in the growth medium from 1μM to 100mM has little effect on the growth rate of yeast cells [63]. The growth behavior of yeast cultures grown in a closed environment will experience the lag phase, logarithmic phase, stationary phase and the death phase [230].

Mutant cells lacking different genes can exhibit different phenotypes. *PMC1* null mutant cell (also denoted as *PMC1*Δ) is viable in low calcium media and fails to grow in media containing high levels of calcium ion [50] whereas *VCX1*Δ is viable in both low and high calcium media [146].

It is well-known that in plant cells, the excess cytosolic calcium ion can be extruded through pumps and exchangers on the plasma membrane [184,185]. But for yeast cells, it is not the case. Calcium efflux is truly observed in real yeast cells [90], however, there is no Ca^{2+}-ATPase or exchanger detected on the plasma membrane [212,244]. The calcium ion in the non-exchangeable pool (i.e., the vacuole) is mainly diluted by the exponential growth of yeast cells since the vacuole calcium efflux into the cytosol *in vivo* is proved to be very small under normal conditions [63]. The calcium efflux from the real cells is thought to be via exocytosis: Ca^{2+} in ER/Golgi is wrapped into secretory vesicles which will eventually fuse with the plasma membrane to free their content. Recently there has been some experimental evidence to support this hypothesis [244].

Although much has been known about the regulation mechanism of calcium homeostasis in yeast cells and there are also some experimental data available, there is no quantitative model yet to describe this important cellular process. The aim of this chapter is to present the first preliminary mathematical model of calcium homeostasis in normally growing yeast cells which is consistent with many available experimental observations. Such model can be used to steer the further experiments for acquiring more missing data and eventually help us to thoroughly understand the underlying mechanisms of calcium homeostasis, which can be a good starting point for revealing the mechanisms of a lot of related cellular processes such as calcium signaling and Zn^{2+} homeostasis [135].

2.2 Methods

2.2.1 Control Block Diagram

Based on the protein level observations and relevant experimental results about the feedback regulation part, we can first build the control block diagram of the calcium homeostasis problem as shown in Fig. 2.1c.

In this diagram, we can see that under normal conditions, if we let the inflow rate through Transporter X into the cytosol subtract the sequestering rates of Pmc1, Pmr1 and Vcx1, then we can immediately get the change rate of cytosolic Ca^{2+}. For non-growing cells, if we take an integral of this change rate and divide it by the volume of the cytosol, then eventually we will get the concentration of cytosolic Ca^{2+} (i.e., $x(t)$). In the case of growing cells, we need to further consider the dilution effect caused by the cell growth.

The mathematical modeling of calcium homeostasis in yeast cells under normal conditions can now be divided into three parts: feedback modeling, protein modeling (including Transporter X, Pmc1, Pmr1 and Vcx1) and growth modeling.

2.2.2 Feedback Modeling

Sensing cytosolic Ca^{2+}: In yeast cells, since one of the two C-terminal EF-hands (site IV) is usually defective, yeast calmodulin can only bind to a maximum of three molecules of

Ca^{2+} [53]. For simplicity, we assume that very strong cooperativity exists among the 3 active sites, then we can describe the cytosolic Ca^{2+} sensing process as follows [93]:

$$3Ca^{2+} + Calmodulin \rightleftharpoons CaM \tag{2.1}$$

where CaM denotes Ca^{2+}-bound calmodulin. If we further denote the concentration of Ca^{2+}-bound calmodulin as $m(t)$, then according to the law of mass action, we can derive the time dependence of $m(t)$ as follows :

$$m'(t) = k_M^+([CaM_{total}] - m(t))x(t)^3 - k_M^- m(t) \tag{2.2}$$

where k_M^+ denotes the forward rate constant, k_M^- denotes the backward rate constant, $x(t)$ denotes cytosolic calcium ion concentration and $[CaM_{total}]$ denotes the total concentration of calmodulin (including Ca^{2+}-free and Ca^{2+}-bound form).

Calcineurin activation: The catalytic (A) unit of calcineurin contains a carboxyl-terminal autoinhibitory domain and upon elevation of cytosolic Ca^{2+} level, Ca^{2+}-bound calmodulin reversibly binds to this catalytic subunit and ultimately activates calcineurin by displacing the autoinhibitory domain [46,53]. This binding process can be described as:

$$CaM + Calcineurin \rightleftharpoons CaN \tag{2.3}$$

where CaN denotes activated calcineurin. Since each molecule of calcineurin binds with one molecule of Ca^{2+}-bound calmodulin, if we denote the concentration of activated calcineurin as $z(t)$, then according to the law of mass action, we can derive the following equation:

$$z'(t) = k_N^+([CaN_{total}] - z(t))m(t) - k_N^- z(t) \tag{2.4}$$

where k_N^+ denotes the forward rate constant, k_N^- denotes the backward rate constant, $m(t)$ denotes the concentration of Ca^{2+}-bound calmodulin and $[CaN_{total}]$ denotes the total concentration of calcineurin (including inactive and activated). This equation will still be valid if $z(t)$ and $[CaN_{total}]$ are all expressed in relative units to a certain constant (i.e., the two sides of the above equation are simultaneously divided by a certain constant), we will make use of this observation later on.

Gene expression control: Experimental results show that activated calcineurin regulates the sequestering rates of Pmc1 and Pmr1 by controlling the synthesis of these two proteins through a transcription factor Crz1 (also named as Tcn1) [111,208]. Although it has not been totally established by experiments that only fully dephosphorylated Crz1 molecules in the nucleus are transcriptionally active, it has been shown to be the case for NFAT1 (a main member of NFAT family) [161,183]. So here we assume that it is also the case for Crz1. As mentioned in the introduction part, here we use a conformational

switch model to simulate Crz1 translocation. By describing the conformational switch model as a protein network and using the rapid equilibrium approximation [183], we can use the following equation to describe the kinetics of the total nuclear Crz1 fraction which is denoted by *h(t)*:

$$h'(t) = d \cdot \phi \cdot (1 - h(t)) - f \cdot \psi \cdot h(t) \tag{2.5}$$

where d denotes the import rate constant, f denotes the export rate constant, ϕ denotes the ratio of the fraction of the cytoslic active conformation over the total cytosolic fraction and ψ denotes the ratio of the fraction of nuclear inactive conformation over the total nuclear fraction. ϕ can be calculated as follows [183]:

$$\phi = \frac{\sum_{n=0}^{N} a_n}{\sum_{n=0}^{N} (a_n + i_n)} = \frac{1}{1 + \sum_{n=0}^{N} i_n / \sum_{n=0}^{N} a_n} = 1/(1 + L_0 \frac{(\lambda k / c)^{N+1} - 1}{\lambda k / c - 1} \frac{k/c - 1}{(k/c)^{N+1} - 1}) \tag{2.6}$$

Where the small case letters a_n and i_n $(n = 0,1,2...N)$ denote cytosolic active and inactive conformations with n phosphorylated residues respectively. k and c denote kinase and calcineurin activity in the cytosol respectively (Please note that in the remaining part of this Chapter, the capital letters A_n, I_n $(n = 0,1,2...N)$, K and C are the corresponding nuclear symbols). N is the number of relevant regulatory phosphorylation sites (In the case of NFAT1, experimental data shows that $N = 13$ [Ref. 161,183]). L_0 is the basic equilibrium constant and λ is the increment factor.

Under the assumption of $k/c = K/C$, we can calculate $\psi = 1 - \phi$. By observing the above expression, ϕ can be regarded as a function of k/c. If we assume that the kinase level is a constant and further express the concentration of activated calcineurin(i.e., $z(t)$) in dimensionless units relative to this constant (see Eq. 2.4) , then

$$\phi(k/c) = \phi(1/(c/k)) = \phi(1/z(t)) \tag{2.7}$$

Now we can rewrite the kinetics equation (Eq. 2.5) of the total nuclear fraction as follows:

$$h'(t) = d \cdot \phi(1/z(t)) \cdot (1 - h(t)) - f \cdot (1 - \phi(1/z(t))) \cdot h(t) \tag{2.8}$$

where ϕ represents the function
$\phi(y) = 1/(1 + L_0 \cdot ((\lambda y)^{N+1} - 1)/(\lambda y - 1) \cdot (y - 1)/(y^{N+1} - 1))$.

Once we know the total nuclear fraction $h(t)$, we can further calculate the transcriptionally active Crz1 fraction in the nucleus as follows[6] [183]:

$$A_0 + I_0 = h(t) \cdot \frac{A_0 + I_0}{\sum_{n=0}^{N}(A_n + I_n)} = \frac{h(t) \cdot (1 + L_0)}{\frac{(K/C)^{N+1} - 1}{K/C - 1} + L_0 \frac{(\lambda K/C)^{N+1} - 1}{\lambda K/C - 1}} \tag{2.9}$$

Under the assumption of $k/c = K/C$, we can rewrite the above expression as

$$A_0 + I_0 = h(t) \cdot \theta(k/c) = h(t) \cdot \theta(1/z(t)) \tag{2.10}$$

where $z(t)$ is in dimentionless units relative to the cytosolic kinase level which is assumed to be constant and the function
$\theta(y) = (1 + L_0)/((y^{N+1} - 1)/(y - 1) + L_0 \cdot ((\lambda y)^{N+1} - 1)/(\lambda y - 1))$..

Once we know the transcriptionally active Crz1 fraction in the nucleus, since Crz1 is a transcription factor which is necessary for the synthesis of Pmc1 and Pmr1, a natural assumption is that the concentrations of these two proteins are proportional to transcriptionally active Crz1 fraction in the nucleus which means that:

$$[Pmc1] = k_a \cdot h(t) \cdot \theta(1/z(t)) \tag{2.11}$$

$$[Pmr1] = k_b \cdot h(t) \cdot \theta(1/z(t)) \tag{2.12}$$

where $[Pmc1]$ and $[Pmr1]$ denote the concentrations of Pmc1 and Pmr1 respectively and k_a, k_b denote the feedback control constants.

For the feedback regulation of activated calcineurin on the synthesis of Vcx1, we do not know exactly what is going on there. The only knowledge about this regulation is that the mechanism is possibly posttranslational and the general effect is suppressing [51]. So here we use a highly putative expression to model this regulation as follows:

$$[Vcx1] = k_d /(1 + k_c \cdot z(t)) \tag{2.13}$$

where k_c, k_d denote the feedback control constants. With this expression the suppressing relation (i.e., when $z(t)$ rises, the concentration of Vcx1 will drop) can be represented.

2.2.3 Growth Modeling

As mentioned before, yeast cells grow by budding and dividing [173,230]. Normal yeast cells are somewhat spherical with a typical diameter of 1-7μm [230], so we can assume

---

[6] Please note that $h(t) = \sum_{n=0}^{N}(A_n + I_n)$, which means that the total nuclear fraction is the sum of the fractions of all the nuclear inactive and active conformations.

our mode cell (without growth) as a sphere with a diameter of 4μm. Since the pattern of cell volume growth is largely exponential [235], it is plausible to model the volume growth as follows (C.L. Woldringh, personal communication):

$$V(t) = V_0 \cdot e^{\alpha t} \tag{2.14}$$

where $V(t)$ denotes the volume of the cell (Please note for $nT \le t \le (n+1)T$, $n = 1,2,3,...,$ the original cell has divided into 2^n cells and *V(t)* is the sum of the volumes of all these 2^n cells) , V_0 denotes the initial volume (33.5 μm^3), T is the mean cell-division-cycle time and α denotes the growth rate constant which can be calculated as $\ln 2 / T$. Since the intracellular organelles are all partitioned during cell growth [173,232], we assume that the volume growth of the organelles (the vacuole, ER and Golgi, etc.) follows the same exponential pattern [44]. Two obversations worthy of notice are that the diameter of the neck area between the mother cell and the bud is much smaller than the size of the mother cell (see Fig. 2.1b) and that the duration of the unbudded period is much shorter than the mean cell-division-cycle time [235]. To calculate the surface area of the cell (including the bud), we can consider an approximating case of the bud sphere growing separately from the mother cell with the total volume bound by the above exponential growth relation (i.e., the volume of the bud $V_b = V_0(e^{\alpha t} - 1)$ for $0 \le t < T$). With this approximation, the surface area of the cell (including the bud) can be calculated as follows:

$$S(t) = S_0 \cdot 2^n \cdot (1 + (e^{\alpha(t-nT)} - 1)^{2/3}) \quad (nT \le t < (n+1)T, n = 0,1,2,3,...) \tag{2.15}$$

where $S(t)$ denotes the surface area of the cell (Please note again that for $nT \le t < (n+1)T, n = 0,1,2,3,...$, the original cell has divided into 2^n cells and $S(t)$ is the sum of the surface areas of all these 2^n cells), S_0 denotes the initial surface area (50.3 μm^2). Under normal conditions, yeast cells will double every 1.5-2.5 hours [63,230]. With such growth rate, it is easy to show that $1 \le (S(t)/S_0)/(V(t)/V_0) < 1.12$ which means that the cell surface area change is roughly proportional to the cell volume change during budding and dividing. So approximately we can use an exponential growth model (similar as Eq. 2.14) instead of using Eq. 2.15 to describe the surface area change of the cell (also to describe membrane surface area change of the organelles) during cell growth. As we will see, such an approximation will make our preliminary model much simpler.

2.2.4 Protein Modeling

Experimental results show that the uptake of all the four involved proteins (Transporter X [132], Pmc1 [215], Pmr1 [205] and Vcx1 [159]) conforms to the Michaelis-Menten equation, which is a general equation for describing single site protein-mediated ion uptake [5]. Moreover, since yeast cells are growing, a natural assumption is that during growth, the uptake rate of calcium transporting protein is proportional to the surface area

of the corresponding membrane on which this protein resides. For example, the uptake rate of Transporter X can be expressed as :

$$U(t) = \frac{V_{\max} \cdot [Ca_{ex}]}{K_x + [Ca_{ex}]} \cdot e^{\alpha t} \tag{2.16}$$

where $U(t)$ denotes the uptake rate of Transporter X, $[Ca_{ex}]$ denotes extracellular calcium ion concentration, $V_{\max}$ is the maximum uptake rate of Transporter X and K_x is the binding constant.

2.2.5 Preliminary Model

Since now we have built the uptake models for all the four involved proteins and models for the relevant feedback regulation, according to the control block diagram (Fig. 2.1c) and by further considering the dilution effect caused by the exponential cell growth, we can derive the main equation of our calcium homeostasis problem as follows:

$$\begin{aligned} x'(t) = & \underbrace{\frac{V_x \cdot [Ca_{ex}]}{K_x + [Ca_{ex}]}}_{TransporterX} - \underbrace{h(t)\theta(1/z(t))\frac{V_1 \cdot x(t)}{K_1 + x(t)}}_{Pmc1} - \underbrace{h(t)\theta(1/z(t))\frac{V_2 \cdot x(t)}{K_2 + x(t)}}_{Pmr1} \\ & - \underbrace{\frac{1}{1 + k_c z(t)}\frac{V_3 \cdot x(t)}{K_3 + x(t)}}_{Vcx1} - \alpha x(t) \end{aligned} \tag{2.17}$$

where $x(t)$ denotes cytosolic calcium ion concentration , $z(t)$ denotes the concentration of activated calcineurin which is expressed in relative units to constant cytosolic kinase level, $h(t)$ denotes total nuclear fraction of Crz1 , α denotes the growth rate, and θ is the function $\theta(y) = (1 + L_0)/((y^{N+1} - 1)/(y - 1) + L_0 \cdot ((\lambda y)^{N+1} - 1)/(\lambda y - 1))$ (Note that in the above main equation the feedback constants k_a, k_b and k_d have been implicated in parameters V_1, V_2 and V_3 respectively, the last term (i.e., $-\alpha x(t)$) appears because the volume of the cytosol is changing during growth. According to differentiation rule, $x'(t) = (C'(t) - x(t) \cdot Vol'(t))/Vol(t)$ where $C(t)$ denotes the cytosolic Ca^{2+} content).

It is reported that after 2.5 hours of incubation, the maximum Ca^{2+} accumulation due to Transporter X is around 390nmol/10^9cells [132]. Since the cell counting is performed at the end of the assay [132] and the cell number has doubled in 2.5 hours, we can roughly calculate parameter V_x in the main equation as follows:

$$\begin{aligned} V_x &= V_{\max}/(V_0 * 10\%) = (2 * 390 nmol/10^9 cells/(\int_0^{2.5hours} e^{\alpha t} dt))/(33.5 \mu m^3 * 10\%) \\ &\approx 1000 \mu M/\min \end{aligned} \tag{2.18}$$

(Please note that here we assume the volume percentage of the cytosol to be 10% [135] and the growth rate constant $\alpha = 0.006\,\mathrm{min}^{-1}$ [63]). Then we have to consider the influence of calcium uptake by the growing yeast cells on the extracellular media calcium ion concentration. Under the most favourable conditions, yeast cells will double in number every 90 minutes until a density of 3-5*10^7 cells/ml after which the growth rate slows down [230]. So after 2.5 hours of normal growth from any initial density (obviously this density should be less than 2.5*10^7 cells/ml to assure normal log-phase growth), the upper limit of the relative change of extracellular media calcium ion concentration can be roughly estimated as follows:

$$\frac{\Delta[Ca_{ex}]}{[Ca_{ex}]} < \int_0^{2.5h} U(t)dt * (5*10^7\, cells/ml/2)/[Ca_{ex}] * 100\% < 5\% \qquad (2.19)$$

(Please note that K_x is reported to be 500 μM [132]). This means the relative change rate of extracellular media calcium ion concentration is very slow and it is a good approximation to assume $[Ca_{ex}]$ as a constant. Then we look at the change of vacuolar calcium ion concentration after some hours of normal growth:

$$\Delta[Ca_{vacuole}] < \int_0^t U(y)dy/(33.5e^{\alpha t}\mu m^3 * 50\%) < \frac{1}{\alpha}V_{\max}/(33.5\mu m^3 * 50\%) < 32mM \quad (2.20)$$

(Please note that here we assume the volume percentage of the vacuole to be 50% [135] and the growth rate constant $\alpha = 0.006\,\mathrm{min}^{-1}$). If we assume that the initial vacuolar Ca^{2+} concentration to be around 2mM [63] (Please note that this original Ca^{2+} concentration will exponentially decrease due to the exponential growth of vacuolar volume), we can conclude that the influx into the vacuole will never saturate the store due to the dilution effect of cell growth. Since at least 90% of the total cellular Ca^{2+} is sequestered within the vacuole [145], we can estimate the change of calcium ion concentration in ER and Golgi after any hours of normal growth as follows:

$$\Delta[Ca_{ER\&Golgi}] < \int_0^t U(y)dy * 10\%/(33.5e^{\alpha t}\mu m^3 * 10\%) < 16mM \qquad (2.21)$$

(Please note that here we assume the volume percentage of ER and Golgi to be 10%). If we assume that the initial Ca^{2+} concentration in ER and Golgi to be less than 1mM [212] and further take into account the Ca^{2+} efflux from ER and Golgi through exocytosis, we can conclude that the Ca^{2+} saturation in the ER and Golgi will never happen due to the dilution effect of cell growth. So the main equation (Eq. 2.17), together with three previously stated equations (Eqs. 2.2, 2.4, 2.8) for $m(t)$, $z(t)$ and $h(t)$ respectively, constitutes a more or less complete mathematical model for calcium homeostasis in yeast cells under normal conditions. The whole set of parameters (except the control parameter $[Ca_{ex}]$) in our model which will be used in the subsequent simulations are listed in Table 2.1.

Table 2.1: Model parameters for which all results are calculated unless otherwise stated.[7]

Parameter	Value	Description
K_x	500 μM	the binding constant of Transporter X [132]
K_1	4.3 μM	the binding constant of Pmc1 [215]
K_2	0.1 μM	the binding constant of Pmr1 [205]
K_3	100 μM	the binding constant of Vcx1 [159]
V_x	1000 μM/min	the rate parameter of Transporter X (Calculated from [132])
V_1	30000 μM/min	the rate parameter of Pmc1
V_2	100 μM/min	the rate parameter of Pmr1
V_3	10000 μM/min	the rate parameter of Vcx1
k_c	10	the feedback control constant
k_M^+	500 $(\mu M)^{-3}min^{-1}$	the forward rate constant of Eq. 2.2
k_M^-	100 min^{-1}	the backward rate constant of Eq. 2.2
k_N^+	5 $(\mu M)^{-1}min^{-1}$	the forward rate constant of Eq. 2.4
k_N^-	5 min^{-1}	the backward rate constant of Eq. 2.4
$[CaM_{total}]$	25 μM	the total concentration of calmodulin
$[CaN_{total}]$	25	the total concentration of calcineurin
d	0.4 min^{-1}	the nuclear import rate constant [183]
f	0.1 min^{-1}	the nuclear export rate constant [183]
N	13	the number of relevant regulatory phosphorylation sites [183]
L_0	$10^{-N/2}$	the basic equilibrium constant [183]
λ	5	the increment factor [183]
α	0.006 min^{-1}	the growth rate constant [63]

2.3 Results

2.3.1 Steady-State Properties

The model consists of four equations (Eqs. 2.2, 2.4, 2.8, 2.17) with four unknowns: $x(t)$, $m(t)$, $z(t)$ and $h(t)$. By setting the zero initial conditions (except that $z(0)$ is set to be 10^{-8} to avoid the singularity) and then solving the four equations (Eqs. 2.2, 2.4, 2.8, 2.17, using the parameters listed in Table 2.1) numerically, we can first depict the $x(t)$ curves

[7] Please note that $[CaN_{total}]$ is expressed in dimensionless units relative to cytosolic kinase level which is assumed to be constant.

for parameter $[Ca_{ex}] = 1\mu M$ as shown in Fig. 2.2a. In Fig. 2.2b, resting levels of $x(t)$ for different values of parameter $[Ca_{ex}]$ are shown. In the simulations we also investigated resting levels of calcium ion-bound calmodulin. The simulated calcium ion-bound calmodulin concentration rests within 0.048-0.49μM (regardless of the initial conditions) when the simulated medium calcium level ($[Ca_{ex}]$) ranges from 1μM to 100mM. The derived figure (data not shown here) is very similar to Fig. 2.2b.

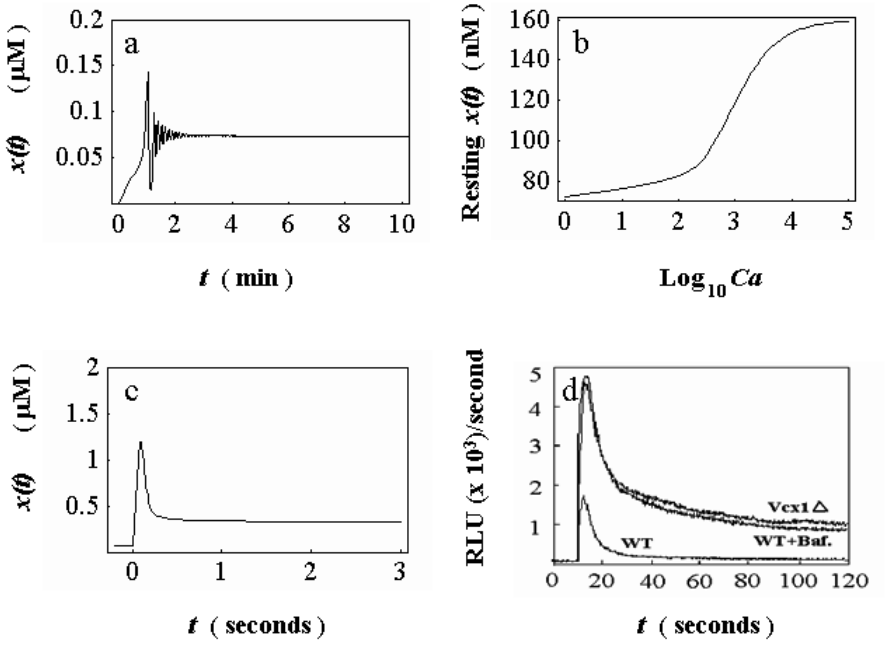

Figure. 2.2. Resting levels and comparison of response curves.
(a) $x(t)$ curve for parameter $[Ca_{ex}] = 1\mu M$ under zero initial conditions (except that $z(0)$ is set to be 10^{-8} to avoid the singularity). The simulated cytosolic calcium ion concentration eventually rests at 73nM. (b) Resting levels of $x(t)$ for different values of parameter $[Ca_{ex}]$. The simulated cytosolic calcium ion level of our model cell rests within 73-159nM (regardless of the initial conditions) when the simulated medium calcium level (parameter $[Ca_{ex}]$) ranges from 1μM to 100mM. (c) Simulated response curve of $x(t)$ under the step-like disturbance of that at $t = 0$, the simulated extracellular calcium ion level ($[Ca_{ex}]$) suddenly changes from 6μM to 100mM. (d) The corresponding experimental response curve of real cells responding to step-like disturbance in media calcium ion concentration (Figure from [146], courtesy of David M. Bedwell), WT denotes wild type cell. Stimulus condition: the extracellular calcium ion concentration is firstly controlled at a low level (~6μM) using EGTA. At $t = 10$ s, the media calcium ion level is suddenly increased to 100mM by injecting $CaCl_2$ into the cuvette. Cytosolic calcium ion concentration is reported in aequorin luminescence. RLU denotes relative luminescence unit. The curve of interest is the bottom curve which is labeled as WT curve. The top two curves in this figure show the response curves of Vcx1 mutant (labeled as Vcx1Δ) and wildtype cell pre-treated with bafilomycin A_1 (labeled as WT+Baf.), respectively.

2.3.2 Transients and Mutant Behavior

Now let us examine how our model cell will respond to extracellular stimulus. For the model cell (Eqs. 2.2, 2.4, 2.8, 2.17, using the parameters listed in Table 2.1), the stimulus condition is that at $t = 0$, the simulated extracellular calcium ion level ($[Ca_{ex}]$) suddenly changes from 6μM to 100mM. The simulated response curves of $x(t)$, $m(t)$, $z(t)$, $h(t)$ and the transcriptionally active Crz1 fraction are shown in Fig. 2.2c and Fig. 2.3(b-d) respectively, in which we can see that at first our model cell is in resting state: the simulated cytosolic calcium ion concentration $x(t)$ rests at 76nM (see Fig. 2.2c), the simulated calcium ion-bound calmodulin concentration $m(t)$ rests at 0.05μM (Fig. 2.3b) and around 47% of Crz1 molecules are in the nucleus (Fig. 2.3d). However, only 2% of all Crz1 molecules are transcriptionally active (see Fig. 2.3d). The sudden change of the simulated extracellular calcium ion level (i.e., parameter $[Ca_{ex}]$) incurs a sudden rise of the simulated cytosolic calcium ion level (Fig. 2.2c) and then calmodulin senses this elevation and binds calcium ions (Fig. 2.3b) to initiate the feedback control mechanism. As a result, the simulated concentration of activated calcineurin quickly rises from its original resting level of 1.29 to a peak value of more than 18 (Fig. 2.3c) and subsequently these activated calcineurin molecules dephosphorylate Crz1 so that the simulated transcriptionally active Crz1 fraction increases from 2% to more than 40% (Fig. 2.3d). Then due to the strong effects of feedback regulation, the simulated cytosolic calcium ion level is quickly lowered and then gradually goes to a new resting level of 159nM (Fig. 2.2c and Fig. 2.3a). Almost at the same time the simulated concentration of calcium ion-bound calmodulin decreases (more gradually) to a new resting value of 0.49μM (Fig. 2.3b) and the simulated concentration of activated calcineurin decreases (even more gradually) to a new resting value of 8.26 (Fig. 2.3c), whereas more Crz1 molecules are imported into the nucleus until that almost all Crz1 molecules are in the nucleus (Fig. 2.3d) and eventually the simulated transcriptionally active Crz1 fraction further increases gradually to a high resting level of 88% (Fig. 2.3d).

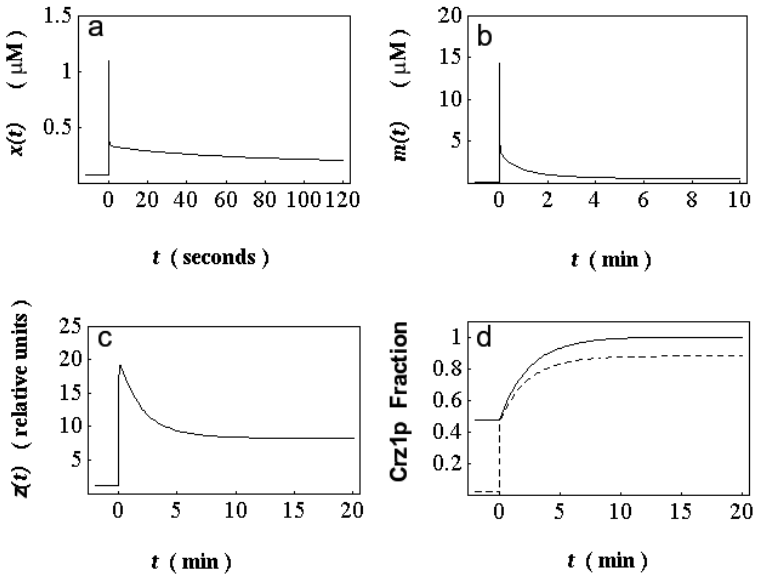

Figure. 2.3. The simulated response curves under the step-like disturbance of that at $t = 0$. The simulated extracellular calcium ion level ($[Ca_{ex}]$) suddenly changes from 6μM to 100mM. (a) Response curve of $x(t)$. This figure is the same as Fig. 2.2c except that here the curve is depicted in a longer time range. (b) Response curve of $m(t)$. (c) Response curve of $z(t)$. (d) Response curves of Crz1 fraction. The solid curve describes the response change of $h(t)$ (i.e., the total nuclear Crz1 fraction) and the dashed curve describes the response change of the transcriptionally active Crz1 fraction.

Now we would like to check the mutant behavior of our model. After taking the sequestering rate part of Pmc1 (i.e., $h(t)\theta(1/z(t))\dfrac{V_1 \cdot x(t)}{K_1 + x(t)}$) out of the main equation (Eq. 2.17), the model cell becomes a *PMC1* null mutant cell. In Fig. 2.4a and Fig. 2.4b, we depict the curves of the simulated cytosolic calcium ion concentration ($x(t)$) of our model *PMC1*Δ cell under the conditions of parameter $[Ca_{ex}] = 6\mu M$ and $[Ca_{ex}] = 200mM$ respectively. From Fig. 2.4a, we can see that in a typical low calcium media (parameter $[Ca_{ex}] = 6\mu M$), after a short transient time, the simulated cytosolic calcium ion concentration eventually rests at 82nM. From Fig. 2.4b, we can see that in a high calcium media ($[Ca_{ex}] = 200mM$), the simulated cytosolic calcium ion concentration rises quickly and almost linearly and there is no physiologically reasonable resting level anymore. In 5 minutes, the simulated cytosolic calcium ion concentration has rocketed up to a level higher than 4mM. The transition point on which the system transiting from having a reasonable resting level to having no reasonable resting level is around 60μM (data not shown here).

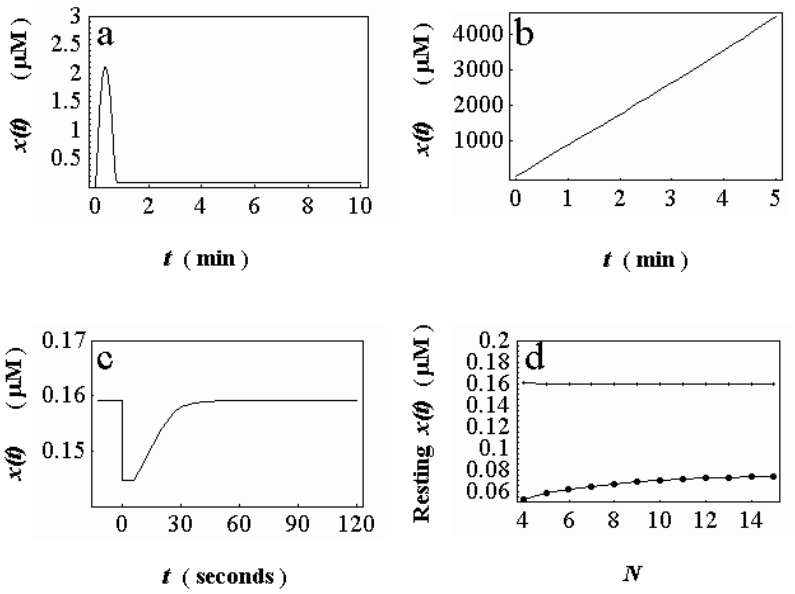

Figure. 2.4. *PMC1* null mutant behaviour and parameter sensitivity. (a) $x(t)$ curve of the simulated *PMC1* null mutant for parameter $[Ca_{ex}] = 6\mu M$ under zero initial conditions (except that $z(0)$ is set to be 10^{-8} to avoid the singularity). The simulated cytosolic calcium ion concentration eventually rests at 82nM. Further tests show this resting level is regardless of the initial conditions. (b) $x(t)$ curve of the simulated *PMC1* null mutant for parameter $[Ca_{ex}] = 200mM$. Here the resting levels for parameter $[Ca_{ex}] = 6\mu M$ are used as initial conditions. In several minutes, the simulated cytosolic calcium ion concentration has rocketed up almost linearly to a level higher than 4mM. Further analysis shows that $x(t)$ eventually rests at an unreasonably high level (143mM) which means the system is out of control. (c) $x(t)$ response curve for parameter $[Ca_{ex}] = 100mM$, at $t = 0$, k_N^+ suddenly increases from 5(μM)$^{-1}$ min^{-1} to 5000(μM)$^{-1}$ min^{-1} and at $t = 6$ seconds, it changes back to 5(μM)$^{-1}$ min^{-1}. (d) Influence of N on the simulated resting levels of $x(t)$. The upper curve (with smaller dots) depicts the resting values of the simulated cytosolic calcium ion concentration for parameter $[Ca_{ex}] = 100mM$ with N ranging from 4 to 15. The lower curve (with larger dots) depicts the simulated resting values for parameter $[Ca_{ex}] = 1\mu M$.

Similarly we can do simulations for the *VCX1* null mutant cell. Investigations show that when the simulated medium calcium level ($[Ca_{ex}]$) ranges from 6μM to 100mM, the simulated cytosolic calcium ion level of our model *VCX1*Δ cell rests within 76-159nM. Under the stimulus condition of that at $t = 0$, the simulated extracellular calcium ion level ($[Ca_{ex}]$) suddenly changes from 6μM to 100mM, the simulated $x(t)$ response curve of our model *VCX1*Δ cell is almost identical to that of the simulated wild type cell (Fig. 2.2c).

2.3.3 Parameter Sensitivity

The next issue is the robustness of our feedback control system. In the following simulation, the test condition is that parameter $[Ca_{ex}]$ is set to be 100mM and at $t = 0$, we let k_N^+ suddenly change from 5(μM)$^{-1}$ min^{-1} to 5000(μM)$^{-1}$ min^{-1} and then at $t = 6$ seconds, it changes back to 5(μM)$^{-1}$ min^{-1}. In Fig. 2.4c, we can see that at first, the simulated cytosolic calcium ion level rests at 159nM and it quickly drops to 145nM due to this large upward impulse-like disturbance, rests there for a while and then recovers to 159nM after the disturbance is over. Further tests show that when large upward or downward impulse-like disturbance is imposed on other rate constants, we can derive similar results.

As mentioned above, in our model the number of relevant regulatory phosphorylation sites (i.e., N) is put to 13, which is actually an experimentally found number for NFAT1 translocation. Since the exact value of N for Crz1 translocation has not been well established, we now would like to examine the influence of parameter N to our model cell behavior. By changing the value of N and recording the corresponding resting levels, we can eventually derive Fig. 2.4d. From this figure, we can see that for high media calcium level ($[Ca_{ex}] = 100mM$, the simulated resting level of our model cell is totally insensitive to the change of N. For low media calcium level ($[Ca_{ex}] = 1\mu M$), the simulated resting level seems to be more sensitive and increases somewhat with the increase of N.

We have tested the sensitivity of the system to every parameter except those reported ones (see Table 2.1) and Table 2.2 gives a summary of the range of the parameter values in which the system is very insensitive to the change of that particular parameter.

Table 2.2: The range of parameter values in which the system shows great insensitivity

Parameter	Value range (Min-Max)	Resting level range of $x(t)$ for $[Ca_{ex}]$ ranging from 1μM to 100mM	
		Parameter = Min	Parameter = Max
V_1	25000-5000000 μM/min	73-185 nM	66-75 nM
V_2	1-800 μM/min	73-167 nM	72-122 nM
k_c	0.1-15	20-158 nM	73-159 nM
k_M^+	0.5-5000 (μM)$^{-3}$min^{-1}	20-81 nM	34-147 nM
k_M^-	80-2000 min^{-1}	68-157 nM	20-255 nM
k_N^+	0.5-500 (μM)$^{-1}$min^{-1}	21-221 nM	16-145 nM
k_N^-	0.5-50 min^{-1}	34-146 nM	21-221 nM
$[CaM_{total}]$	5-500 μM	21-194 nM	27-146 nM

$[CaN_{total}]$	5-500	21-222 nM	27-140 nM
d	0.1-5000 min^{-1}	74-159 nM	70-159 nM
f	0.0001-10 min^{-1}	70-159 nM	78-159 nM
N	4-15	53-161 nM	74-159 nM
λ	0.001-10	61-159 nM	95-159 nM

2.4 Discussion

From Fig. 2.2a and Fig. 2.2b, we can see that when the simulated medium calcium level ($[Ca_{ex}]$) ranges from 1μM to 100mM, the simulated cytosolic calcium ion level of our model cell rests within 73-159nM. Further tests show that the above simulated resting levels are independent of the initial conditions. In normal real yeast cells the cytosolic calcium ion concentration rests within 50-200nM when medium calcium level ranges from < 1μM to > 100mM [145]. The resting levels of our model cell agree with those of real cells.

As mentioned above, when the simulated medium calcium level ($[Ca_{ex}]$) ranges from 1μM to 100mM, the simulated resting level of calcium ion-bound calmodulin remains under a level of 0.5μM. By noting that in the model the total concentration of calmodulin $[CaM_{total}]$ is put to be 25μM (see Table 2.1), we can conclude that the absolute majority of calmodulin molecules are in calcium ion-free form when our model cell is resting. When the simulated cytosolic calcium ion level ($x(t)$) is elevated, calmodulin senses this elevation and quickly binds calcium ion to activate calcineurin (see Fig. 2.3a, Fig. 2.3b and Fig. 2.3c). Such behavior of calmodulin is in accordance with the relevant knowledge presented in literature [53].

By comparing this experimental curve (WT curve in Fig. 2.2d) with the corresponding $x(t)$ curve (Fig. 2.2c) of the model cell, we can find that the general shape of two curves is in accordance: cytosolic calcium ion concentration rises and falls due to the extracellular stimulus. As to the amplitude, the peak value of the experimental (WT) curve in Fig. 2.2d is equivalent to ~260nM [146]. The amplitude of our model response curve (its peak value is around 1.2μM) is in the same order of that of the experimental curve. By depicting the $x(t)$ curve of the model cell in a range of two minutes after the disturbance (Fig. 2.3a) and making the comparison with Fig. 2.2c again, we find that the general part (30-120 seconds after the disturbance) is in agreement with that of the experimental curve: the cytosolic calcium ion level gradually decreases to a new low resting value. Actually a remarkable difference exists in the widths of response spikes. This effect will be explained in Chapter 3.

From Fig. 2.4a, we can see that in low calcium media, our model *PMC1* null mutant cell can achieve calcium homeostasis very well, although this ability is a bit compromised

compared to that of the simulated wild type cell (Please note that for $[Ca_{ex}] = 6\mu M$, the resting $x(t)$ level of our model wild type cell is 76nM whereas the resting $x(t)$ level of our model *PMC1*Δ cell is 82nM). From Fig. 2.4b, we can see that in high calcium media, the simulated cytosolic calcium level is out of control and our model *PMC1*Δ cell must die since calcium homeostasis is vitally important for cell viability. Further tests show that this behavior is basically independent of the initial conditions. These results suggest that our simulated *PMC1*Δ cell exhibits the similar basic characteristic which has been experimentally found in real *PMC1*Δ cell: it is viable in low calcium media and fails to grow in media containing high levels of calcium ion [50].

Robustness is an essential property of biological systems [16,119]. The main phenomenological property exhibited by robust systems is parameter insensitivity which means that the system is relatively insensitive to specific kinetic parameters. In Fig. 2.4c, we can see that when large impulse-like disturbance is imposed on a certain rate constant of our model system, the simulated cytosolic calcium ion level changes slightly and the system quickly recovers to its original resting level when the disturbance is over. In Fig. 2.4d, we can see that in general the value change of N will not have much influence on resting levels. For example, when $N = 4$, the model cell will rest within 53-161nM with parameter $[Ca_{ex}]$ ranging from 1μM to 100mM. When $N = 15$, the model cell will rest within 74-159nM. These ranges of the simulated resting levels are in accordance with the experimentally found range of 50-200 nM. This indicates that our previous discussions of resting levels are not only applicable for only one specific value $N = 13$, but also can apply to other values of N. We can show that our previous discussions of the other behavior of our model cell such as response curves, mutant behavior and robustness are valid for any reasonable value of N. From Table 2.2, we can see that the behavior of our model cell (Eqs. 2.2, 2.4, 2.8, 2.17) exhibits a large degree of insensitivity for almost every parameter except those reported ones. As for parameter V_3, when it ranges from 0 to 10000μM/min, the system always rests within 76-159nM for $[Ca_{ex}]$ ranging from 6μM to 100mM and small oscillations are occasionally observed for $[Ca_{ex}]$ ranging from 1μM to 6μM. Since these small oscillations are bound between 30-150nM and they only occur for a small range of $[Ca_{ex}]$ values, they have limited influence on the effectiveness of our model. All these results show that the feedback control mechanism in our model cell is robust.

The simulation results of our model cell show that tightly controlled low cytosolic calcium ion level can be very natural under the general mechanism of gene expression feedback control (see Fig. 2.2a, Fig. 2.2b and Fig. 2.2c). The calmodulin (a sensor protein) behavior in our model cell agrees well with observations in actual cells (see Fig. 2.3a, Fig. 2.3b and Fig. 2.3c). Our model can qualitatively reproduce the reported response curve of real yeast cells responding to step-like disturbance in media calcium ion level (see Fig. 2.2c and Fig. 2.2d). Our model mutant cell such as *PMC1* null mutant can exhibit some basic characteristic similar to that of real mutant cells (see Fig. 2.4a and Fig. 2.4b). Moreover, the feedback control mechanism in our model is shown to be robust (see

Fig. 2.4c, Fig. 2.4d and Table 2.2). Our model cell exhibits a homeostatic behavior similar to that of real yeast cells, whose main characteristic is robust ``perfect'' adaptation.

On the other hand, we have to realize that this is a relatively coarse model. For example, in the current model, we assume that the concentrations of Pmc1 and Pmr1 are directly proportional to the quantity of transcriptionally active Crz1 (Eqs. 2.11, 2.12). This is a big simplification since in real cells, this process involves the increased gene expression through Crz1 followed by translation and trafficking of the proteins to the respective intracellular destinations [5]. The existence of unknown factors further puts limitations on our model. Besides the unknown mechanism through which Vcx1 is regulated by activated calcineurin, recently some other factors such as Rcn1 [100,111], Mck1 [100] and an ER-localized ATPase Cod1/Spf1 [47] have been shown to play certain roles (although not major roles) in yeast calcium homeostasis. Moreover, the current model does not include the influence from other relevant pathways whereas in real cells, any response to given extracellular stimulus is likely to be the result of complex cross-talk between multiple pathways [184]. For example, it has been reported that intracellular glucose 1-phosphate and glucose 6-phosphate levels modulate calcium homeostasis in yeast cells [4] which means that the glucose metabolism pathway is coupled with the pathway of calcium homeostasis.

The coarseness of our model determines that there are certain discrepancies between our model cell behavior with the behavior of real cells. For example, for our model *PMC1* null mutant cell, the transition point on which the system transits from having a reasonable resting level to having no physiologically reasonable resting level is around 60μM, which is much lower than that of real *PMC1*Δ cell transiting from being viable to being inviable (about 200mM, [50]). As mentioned in Section 2.3.2, the response curve of our model *VCX1Δ* cell (data not shown here) is almost identical to that of the simulated wild type cell (Fig. 2.2c) whereas from Fig. 2.2d, we can clearly see that in the case of real cells, there are distinct differences between the experimental response curve of *VCX1*Δ cell (*VCX1*Δ curve in Fig. 2.2d, its peak value is equivalent to ~360nM [146]) with that of the wild type cell (WT curve in Fig. 2.2d, its peak value is equivalent to ~260nM [146]). Moreover, there are published data indicating that *PMC1* mRNAs accumulate and peak over the course of 10 to 30 minutes before declining when yeast cells are dealt with 100mM extracellular calcium media (see Fig. 2B in Ref. 100). From Fig. 2.3d, we can see that for our model cell, transcriptionally active Crz1 (thus also *PMC1* mRNAs according to our model assumption) accumulate over the course of 10 to 20 minutes. So our model can explain the accumulation and the corresponding time scale is comparable. However, it can not explain the final decline as shown in Fig. 2B in Ref. 100.

We should note that this model is built for log-phase yeast cultures grown in standard synthetic or YPD medium at about 26-30 ^{0}C [50,51,63,132,145,146,150,215]. For yeast cultures grown in very poor media or for yeast cultures out of the log-phase, the current model will possibly not be valid anymore because the dilution effect caused by cell growth may become too small to prevent the saturation of the inexchangeable pool - the vacuole. For example, if the growth rate is zero, for $[Ca_{ex}] = 100mM$, according to our

model, the cytosolic Ca^{2+} will rest at 159nM, and the total steady flux through Pmc1 and Vcx1 should be $941\mu M/\min * Vol$. We can calculate the characteristic time of vacuolar Ca^{2+} saturation by $t_{vac} = 200mM/(941\mu M/\min * (Vol/V_{vac})) = 1063$ min which means after about 18 hours, the vacuole will eventually be saturated for non-growing cells (Please note that here we assume the maximum possible Ca^{2+} concentration in the vacuole to be 200mM).

To conclude, we have built the first preliminary mathematical model to describe calcium homeostasis in growing yeast cells under normal conditions. It provides the first quantitative example exploring the consequences of changes in the quantity of Ca^{2+}-pump and exchanger due to the expression of the protein-encoding genes that follows Ca^{2+}-dependent signal cascade. Such exploration is partially supported by the experimental evidence [100]. The model can correctly predict the different phenotypes of different mutant cells like *PMC1*Δ and *VCX1*Δ. It gives the first quantitative explanation that *PMC1* null mutant's failure to grow in media containing high levels of Ca^{2+} is possibly due to its inability of achieving calcium homeostasis. With this model, we can test and verify theoretical hypotheses by comparing simulation results with corresponding experimental results and generate new hypotheses on the regulation of calcium homeostasis. On the other hand, due to the existence of unknown factors and the lack of experimental data, this model is not an exact model yet. However, it does can give some quantitative insight into the possible dynamics of the whole process and provide a general framework for more elaborate investigations. As we will see in Chapter 3, in order to make it compatible with some new experimental findings, we will revise and extend this preliminary model and develop a new mathematical model to simulate the cytosolic calcium dynamics of *yvc1 cch1* yeast cells in response to hypertonic shock.

Chapter 3 Detection of A New Calcium Transporter on Yeast Plasma Membrane[8]

3.1 Introduction

As described in Section 1.3.4.1 and Section 1.3.4.2, Ca^{2+} functions as a ubiquitous intracellular messenger by which extracellular factors induce a variety of physiological responses such as proliferation and muscle contraction, etc [5,89]. In budding yeast (*Saccharomyces cerevisiae*), calcium signals are used to effect important adaptations in response to mating pheromones [108], membrane damaging compounds [28], and a variety of environmental stresses such as high salt, high pH, high osmolarity, and others [150].

Due to the sudden increase in extracellular Ca^{2+}, cytosolic free Ca^{2+} level rapidly rises and falls with complex dynamics, as judged by luminescence measurements of yeast cells expressing aequorin [145]. In response to these changes, the universal Ca^{2+} sensor protein calmodulin can bind and activate the protein phosphatase calcineurin, which inhibits the function of Vcx1 and induces the expression of Pmc1 and Pmr1 via activation of the Crz1 transcription factor (see Fig. 3.1a) [50,51,53,111,208]. These calcineurin-sensitive adaptations appear to be crucial for proliferation of yeast cells in high calcium environments. Mathematical modeling of these feedback networks successfully recapitulated the observed changes in aequorin luminescence (see Fig. 2.2c-d). In this chapter, we extend the initial model that was discussed in Chapter 2.

[8] This Chapter is based on: Jiangjun Cui, Jaap Kaandoorp, Olufisayo O. Ositelu, Veronica Beaudry, Alicia Knight, Yves F. Nanfack and Kyle W. Cunningham, Simulating calcium influx and free calcium concentrations in yeast, *Cell Calcium*, in press, (2008).

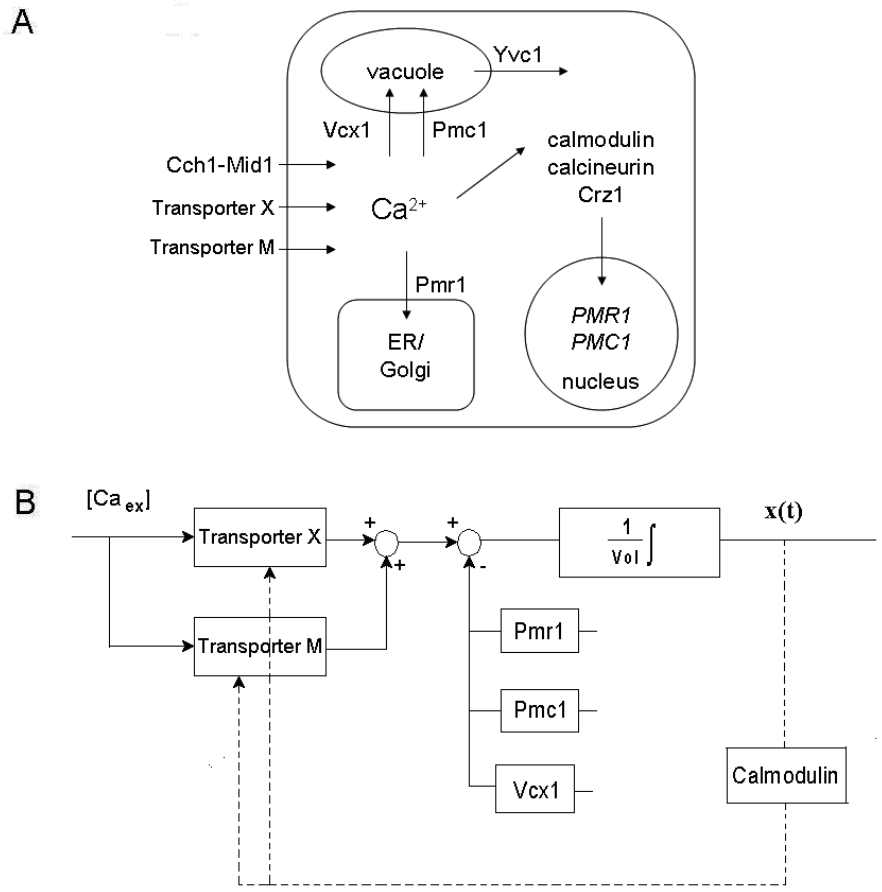

Figure. 3.1. Schematic graph of the system and control block diagram. *Panel A*, A schematic graph of Ca^{2+} homeostasis/signaling system in yeast cells (it is easy to see that this graph is a slightly modified version of Fig. 2.1a). Transporter M is newly detected in this work and is assumed to open under extremely high extracellular Ca^{2+} concentration. *Panel B*, Control block diagram of our model. In *yvc1 cch1* yeast cells, the cytosolic Ca^{2+} influx is through Transporter X and an assumed Transporter M, the cytosolic Ca^{2+} outflux is through Pmc1, Pmr1 and Vcx1. The dashed lines describe the feedback regulations: cytosolic Ca^{2+} concentration is sensed by the calmodulin and Ca^{2+}-bound calmodulin is assumed to inhibit the activity of both transporters M and X.

Here we show that the calcineurin-dependent feedback networks described above have little or no effect on aequorin luminescence traces within the first few minutes of Ca^{2+} shock. Therefore, the initially complex dynamics of cytosolic Ca^{2+} homeostasis must arise through other mechanisms. The observed dynamics are well described by a new mathematical model that omits calcineurin-dependent feedback and instead includes rapid Ca^{2+}-dependent feedback inhibition of Ca^{2+} influx. Though the feedback mechanism and the Ca^{2+} influx transporters all remain to be identified, experimental

evidence suggests that the primary Ca^{2+} influx transporters are competitively inhibited by extracellular Mg^{2+}. Indeed, the impaired growth of yeast cells in high calcium environments was ameliorated by inclusion of Mg^{2+} salts in the medium and the best fitting mathematical model incorporates two Mg^{2+}-sensitive Ca^{2+} influx pathways with different cation affinities. These findings extend a recent report of Ca^{2+} influx pathways in yeast that become (re)activated upon withdrawal of extracellular Mg^{2+} [234] and demonstrate the power of combining experimental and computational methodologies.

3.2 Methods

3.2.1 Experimental Methods

The ability of extracellular Mg^{2+} to prevent toxicity of extracellular Ca^{2+} to yeast was measured as in [50]. Briefly, stationary phase cultures of each yeast strain were diluted 1000-fold into fresh YPD pH 5.5 medium containing varying concentrations of $CaCl_2$ and $MgCl_2$, incubated at 30°C for 24 hr, and then optical density was measured at 650 nm using a 96-well platereader (Molecular Devices). The concentration of $CaCl_2$ causing a 50% inhibition of growth (the IC_{50}) was obtained by fitting the data to the simple sigmoid equation.

Cytosolic free Ca^{2+} concentrations were monitored in populations of yeast cells expressing aequorin essentially as described [150]. Briefly, yeast cells were transformed with plasmid pEVP11 and grown to mid-log phase in synthetic medium lacking leucine to select for plasmid maintenance. Cells were harvested by centrifugation, washed, and resuspended at OD600 = 20 in medium containing 10% ethanol and 25 μg/mL coelenterazine (Molecular Probes, Inc.). After 45 min incubation at room temperature in the dark, cells were washed twice with YPD pH 5.5 medium and shaken at 30°C for an additional 90 min. Aliquots of the cell suspension (450 μL) were pipetted into tubes containing appropriate volumes of 1 M $MgCl_2$, mixed, and placed into a Sirius tube luminometer (Berthold Inc.). Luminescence was recorded at 0.2 sec intervals for 0.5 min prior to and 3.0 min post injection of 2 M $CaCl_2$ (300 μL). Output is plotted as relative luminescence units per second (RLU) over time using similar numbers of cells per sample.

3.2.2 Mathematical Modeling

3.2.2.1 Control Block Diagram

In the control block diagram as shown in Fig. 3.1B, we can see that for yeast cells with fixed volume, we can calculate the concentration of cytosolic Ca^{2+} (i.e., $x(t)$) by taking an integral of the flux rate difference (i.e., the influx rate through Transporter M and Transporter X into the cytosol subtracting the sequestering rates of Pmc1, Pmr1 and Vcx1) divided by the cytosolic volume. Since the slow gene expression feedback pathway through calcineurin has now been shown not to be accounting for the observed response

spikes, there should be some other quick feedback mechanisms the details of which we are currently quite ignorant to. Since calmodulin has been reported to have the ability of directly regulating the opening probability of Ca^{2+} influx pathways [243] , here for simplicity, we just assume that the activity of Transporter M and Transporter X are both directly inhibited by Ca^{2+}-bound calmodulin (see the dashed lines in Fig. 3.1B). If the volume of yeast cells changes due to growth or hypertonic shock etc., then we need to further consider the effects caused by the cellular volume change.

The mathematical modeling for simulating calcium response curves in *yvc1 cch1* yeast cells can now be divided into three parts: feedback modeling, protein modeling (including Transporter M, Transporter X, Pmc1, Pmr1 and Vcx1) and volume evolution modeling.

3.2.2.2 Feedback Modeling

Sensing cytosolic Ca^{2+}: Here we use the same equation as Eq. 2.2 to describe the cytosolic Ca^{2+} sensing process by yeast calmodulin:

$$m'(t) = k_M^+([CaM_{total}] - m(t))x(t)^3 - k_M^- m(t) \tag{3.1}$$

Where $m(t)$ denotes the concentration of Ca^{2+}-bound calmodulin and $m'(t)$ denotes its change rate, k_M^+ denotes the forward rate constant, k_M^- denotes the backward rate constant, $x(t)$ denotes cytosolic calcium ion concentration and $[CaM_{total}]$ denotes the total concentration of calmodulin (including Ca^{2+}-free and Ca^{2+}-bound form).

Once we know the concentration of Ca^{2+}-bound calmodulin, we can use algebraic expressions to model its presumed inhibitory regulation on Transporter M and Transporter X as follows:

$$J_M = J_{MO}/(1 + k_a \times m(t)) \tag{3.2}$$
$$J_X = J_{XO}/(1 + k_b \times m(t)) \tag{3.3}$$

where k_a, k_b denote the feedback control constants. J_M and J_X denote the calcium ion flux through Transporter M and Transporter X respectively. J_{MO} and J_{XO} denote the calcium ion flux through Transporter M and Transporter X in the case of without calmodulin inhibition. Obviously with such simple algebraic expressions the inhibitory relation (i.e., when $m(t)$ rises, the activity of Transporter M and Transporter X will both drop) can be represented.

3.2.2.3 Volume Evolution Modeling (Under Hypertonic Shock)

As we will see later, our aequorin response curves are all obtained under condition of applying hypertonic shocks (e.g., by the sudden injection of 800 mM $CaCl_2$ into the extracellular medium) to the yeast cells. Under such great osmotic perturbation, yeast

cells will quickly shrink due to the existence of water channels in the plasma membrane [79,56,206]. The evolution of the cell volume is governed by the following equation [56]:

$$V'(t) = -A(t)L_p\sigma(\prod_{ex} - RTn_s/(V(t)-b)) \tag{3.4}$$

Where $V(t)$ and $A(t)$ denote the volume and the surface area of yeast cells at time t, respectively, $V'(t)$ denotes the change rate of yeast cell volume, L_p denotes the hydraulic membrane permeability, σ denotes the reflection coefficient, R denotes the ideal gas constant, T denotes the room temperature (294.15 K), n_s denotes the apparent number of osmotically active molecules in the cell, b denotes the non-osmotic volume and $\prod_{ex}$ denotes the osmotic pressure of the external medium which can be calculated as $\prod_{ex} = \prod_0 + 3([Ca_{ex}] + [Mg_{ex}])RT$ where $\prod_0$ denotes the initial osmotic pressure of the external medium, $[Ca_{ex}]$ and $[Mg_{ex}]$ denote extracellular Ca^{2+} concentration and extracellular Mg^{2+} concentration respectively (Please note that we can calculate $A(t) = 4\pi(3V(t)/4/\pi)^{2/3}$ because yeast cells are somewhat spherical).

The initial intracellular osmotic pressure ($\prod_i(0)$) for yeast cells in standard medium is around 0.636 Osm [79], according to Boyle van't Hoff's law, $\prod_i(t) = RT(n_0 + x(t))/(V(t)-b)$ where $x(t)$ denotes cytosolic calcium ion concentration. This means that the initial apparent number of osmotically active molecules n_0 in yeast cell is around 0.636*0.4 mol/l* V_0 = 3.82 *10^{-14}mol (please note that b is 0.4 V_0 and V_0=100μm^3 is the initial volume of the yeast cell [79]). As a common knowledge, $x(t)$ is always <1mM (even under extremely high hypertonic shock) which is small compared with n_0. So we can assume $n_s = n_0 + x(t)$ as a constant.

3.2.2.4 Protein Modeling

Experimental results show that the uptake behavior of the four involved proteins (Transporter X [132], Pmc1 [215], Pmr1 [205] and Vcx1 [159]) conform to the Michaelis-Menten equation, which is a general equation for describing the single site ion uptake behavior of many kinds of transport proteins [5,41]. If we assume that the uptake behavior of Transporter M can also be modeled using this equation and that Mg^{2+} is a competitive inhibitor of this transporter, according to the classical enzyme kinetics theory of competitive inhibition (see Section 1.5.2) [58,178], the uptake rate of Transporter M can be expressed as :

$$J_{MO} = \frac{V_{\max} \times [Ca_{ex}]}{K_m(1 + [Mg_{ex}]/K_{IM}) + [Ca_{ex}]} \tag{3.5}$$

where J_{MO} denotes the uptake rate of Transporter M (without calmodulin inhibition), $[Ca_{ex}]$ and $[Mg_{ex}]$ denote extracellular Ca^{2+} concentration and extracellular Mg^{2+}

concentration respectively, $V_{\max}$ is the maximum uptake rate of Transporter M, K_m is the binding constant and K_{IM} is the inhibition constant. And we can build a similar mathematical model for Transporter X which has been shown to be Mg^{2+}-sensitive [132].

3.2.2.5 A Concise Model

Since now we have built the uptake models for all the five proteins involved in Ca^{2+} transport and models for the relevant feedback regulation, according to the control block diagram (Fig. 3.1B) and by further taking consideration of the effect of cell volume shrinkage, we can derive the main equation of our calcium homeostasis problem as follows [69]:

$$x'(t) = f \times ((J_M + J_X - J_{Pmc1} - J_{Vcx1} - J_{Pmr1}) - x(t)Vol'(t))/Vol(t) \tag{3.6}$$

Where $x'(t)$ denotes the change rate of cytosolic free Ca^{2+} concentration, J_M, J_X, J_{Pmc1} J_{Vcx1} and J_{Pmr1} denote the calcium ion flux through Transporter M, Transporter X, Pmc1, Vcx1 and Pmr1 respectively, $Vol(t)$ denotes the volume of the cytosol at time t which can be roughly calculated as $10\%V(t)$ and $Vol'(t)$ denotes its change rate, f denotes the calcium buffer effect constant [69]. As stated in page 105 of Ref. 69, "f_i (i.e., f) can be interpreted as the fraction of $[Ca^{2+}]_i^{tot}$ (i.e., total cytosolic calcium) which is free. Typical measured values for f_i are 0.01-0.05." In yeast cells, the calcium buffer effect is especially severe (we believe that >99% of total cytosolic calcium is bound).

We can further write the above main equation in fully detailed mathematical form:

$$x'(t) = f \times \Big(\underbrace{\frac{1}{1+k_a m(t)} \frac{V_m \times [Ca_{ex}]}{K_m(1+[Mg_{ex}]/K_{IM}) + [Ca_{ex}]}}_{TransporterM} + \underbrace{\frac{1}{1+k_b m(t)} \frac{V_x \times [Ca_{ex}]}{K_x(1+[Mg_{ex}]/K_{IX}) + [Ca_{ex}]}}_{TransporterX}$$
$$- \underbrace{\frac{V_1 \times x(t)}{K_1 + x(t)}}_{Pmc1} - \underbrace{\frac{V_2 \times x(t)}{K_2 + x(t)}}_{Pmr1} - \underbrace{\frac{V_3 \times x(t)}{K_3 + x(t)}}_{Vcx1} - V'(t)x(t))/V(t) \Big) \tag{3.7}$$

where $x(t)$ denotes cytosolic calcium ion concentration, m(t) denotes the concentration of Ca^{2+}-bound calmoculin, K_m, K_x, K_1, K_2 and K_3 are the Michaelis binding constants of Transporter M, Transporter X, Pmc1, Vcx1 and Pmr1 respectively, V_m, V_x, V_1, V_2 and V_3 are the corresponding rate parameters.

Previously published data [132] show that after 2.5 h of incubation, the maximum Ca^{2+} accumulation due to Transporter X is around 390nmol/10^9 cells. We can roughly calculate parameter V_x in the main equation (Eq. 3.7) as follows (for details, please see Eq. 2.18):

$$V_x = V_{\max}/10\% = 2*390nmol/10^9 cells/\int_0^{2.5h} e^{\alpha t}dt/10\% = 3.2*10^{-17} mol\cdot \min^{-1} \quad (3.8)$$

Where α denotes the growth rate constant the value of which is 0.006 $\min^{-1}$[63].

The main equation (Eq. 3.7) together with the calcium sensing equation (Eq. 3.1) and volume evolution equation (Eq. 3.4) constitute a concise mathematical model for simulating response curves in *yvc1 cch1* yeast cells under hypertonic shocks. The whole set of parameters (except the control parameters $[Ca_{ex}]$ and $[Mg_{ex}]$) in our model which will be used in the subsequent simulations are listed in Table 3.1.

Table 3.1: Model parameters for which all results (except Fig. 3.4C) are calculated unless otherwise stated[9].

Parameter	Value	Description
K_m	505.43 mM	the binding constant of Transporter M
K_x	500 μM	the binding constant of Transporter X [132]
K_1	4.3 μM	the binding constant of Pmc1 [215]
K_2	0.1 μM	the binding constant of Pmr1 [205]
K_3	25 μM	the binding constant of Vcx1 [63]
K_{IM}	149.18 mM	the Mg^{2+} inhibition constant of Transporter M
K_{IX}	3.51*10^{-6} μM	the Mg^{2+} inhibition constant of Transporter X
V_m	1.239*10^{-16} mol·$\min^{-1}$	the rate parameter of Transporter M
V_x	3.2*10^{-17} mol·$\min^{-1}$	the rate parameter of Transporter X (Calculated from [132])
V_1	4.459*10^{-17} mol·$\min^{-1}$	the rate parameter of Pmc1
V_2	4.394*10^{-17} mol·$\min^{-1}$	the rate parameter of Pmr1
V_3	1.682*10^{-15} mol·$\min^{-1}$	the rate parameter of Vcx1

[9] Please note that in Table 3.1, thirteen parameters including $K_m, K_{IM}, K_{IX}, V_m, V_1, V_2, V_3, k_a, k_b, k_M^+, k_M^-, L_{\max}$ and f are estimated values by doing optimal fitting to the experimental data for the two transporters model using an hybrid optimization method (see Section 3.2.3: **Parameter Estimation Method).**

k_a	0.0448	the feedback control constant of Transporter M
k_b	4.319	the feedback control constant of Transporter X
k_M^+	3.751 $(\mu M)^{-3}min^{-1}$	the forward rate constant of Eq. 3.1
k_M^-	0.02445 min^{-1}	the backward rate constant of Eq. 3.1
$[CaM_{total}]$	25 μM	the total concentration of calmodulin [183]
$L_{\max}$	1.9996*10^9 RLUs	the maximal aequorin luminescence
f	0.007626	the calcium buffer effect constant
L_p	6*10^{-12}m·s^{-1} ·Pa^{-1}	the hydraulic membrane permeability [56]
σ	0.035	the reflection coefficient
b	0.4 V_0	the non-osmotic volume of yeast cell [79]
n_s	3.82 *10^{-14}mol	the apparent number of osmotically active molecules in the cell (calculated from [79])
$\prod_0$	0.24 Osm	the initial osmotic pressure of the external medium [79]
V_0	100μm^3	the initial volume of the yeast cell [79]

3.2.2.6 Conversion to Aequorin Luminescence Unit (RLUs)

Here we use the following experimentally reported function [7,88] to convert calcium ion concentration from μM to aequorin luminescence unit (i.e., RLU: relative luminescence unit) so that we can make intuitive comparison between our numerical solutions (in μM) with experimentally obtained aequorin response curves (in RLU):

$$y(x) = \left(\frac{1+7x}{1+118+7x}\right)^3 \times L_{\max} \tag{3.9}$$

Where x denotes Ca^{2+} concentration value in unit μM and $L_{\max}$ denotes the maximal aequorin luminescence.

3.2.3 Parameter Estimation Method

The above described two transporters model (Eqs. 3.1, 3.4, 3.7. We name this model as two transporter model because in this model, it is assumed that there are two influx pathways: Transporters M and X) has 25 parameters, 13 of which ($K_m, K_{IM}, K_{IX}, V_m, V_1, V_2, V_3, k_a, k_b, k_M^+, k_M^-, L_{\max}$ and f) are free parameters which need

to be estimated[10]. Here we use a hybrid optimization algorithm to estimate the model parameters by minimizing the difference between the experimental data and the model prediction. The hybrid optimization algorithm consists of a combination of a stochastic evolutionary algorithm [23, 152] for the global search to find a good initial guess followed by a local search performed using Levenberg-Marquardt algorithm to refine the quality of the fit.

To describe a bit more specifically, the stochastic evolutionary algorithm is a stochastic process that modifies an original population of individuals from iteration to iteration with the aim of minimizing an objective function. In this study, we use a modified (μ, λ)-Evolutionary Strategy (ES), based on stochastic fitness ranking [23, 152]. This method is simple and has proven to be more efficient than most other classical evolutionary algorithms for large parameter estimation problems [147, 180, 181]. The local search was performed using the Matlab (The Mathworks, Inc) function "LSQCURVEFIT" which employs Levenberg-Marquardt algorithm to do the curve fitting for non-linear data.

We simultaneously fit the model to both the wild-type data (see Fig. 3.2B) and the mutant data (see Fig. 3.2C) by minimizing the least square error (LSE). As usual, we proportionally weight the wild-type data based on the maximum amplitude of each data set and take mutant data weight to be 1/3 of the wild-type data because the mutant data is less important than the wild-type data. This leads us to minimize the weighted least square error given as:

$$F(\theta) = \sum_{a=1}^{2} \sum_{m=1}^{5} \sum_{n=0}^{n=Tn} w_{a,m,n} (Y_{a,m}^{n} - F(a,m,n))^2 \tag{3.10}$$

where a denotes the type of data (wild-type or mutant). Let $S = \{0, 0.3\text{mM}, 3\text{mM}, 30\text{mM}, 90\text{ mM}\}$, then m denotes the case in which extracellular $MgCl_2$ is the m th element of S. n denotes the time point and Tn denotes the number of data points in the dataset for a single experimental response curve. Thus $Y_{a,m}^{n}$ denotes the concentration for the data type a with extracellular Mg^{2+} = S[m] at time $t = n * td$ where td denotes the time difference between the consecutive data points (in our case, $td = 0.2s$ and $Tn = 300$), $F(a,m,n)$ is the simulated data and $w_{a,m,n}$ is the associated weight.

In addition to fitting the two transporters model to the experimental data, we also performed fitting for the one transporter model. In this case, Transporter X is assumed to be the only influx pathway (i.e., under the condition of $V_m = 0$, Eqs. 3.1, 3.4, 3.7 constitute the one transporter model) and only 9 parameters ($K_{IX}, V_1, V_2, V_3, k_b, k_M^+, k_M^-, L_{\max}$ and f) are free parameters which need to be estimated. Because of the stochastic nature of the optimization strategy used here, lots of fitting

[10] Here we did not include σ because the solution curve of $x(t)$ is extremely insensitive to the value change of this parameter and this will be further discussed in the sixth paragraph of Section 3.4.

were made for both the one transporter and two transporters model[11]. In order to be able to compare both models, the same parameter boundary was given for each parameter and the optimization was run under the same condition (500 iterations of global search and 10000 iterations of local search). The estimated parameters values together with the remaining parameter values for the best fit of two transporters model are shown in Table 3.1. The simulation results of the best fit for two transporters model and for one transporter model are shown in Fig. 3.4A-C.

3.3 Results

3.3.1 Mg^{2+} Blocks Ca^{2+} Toxicity and Ca^{2+} Influx in Yeast

Yeast mutants lacking the vacuolar Ca^{2+} ATPase Pmc1p grow as well as wild-type yeast strains in standard culture media but they grow much poorer than the wild-type when environmental Ca^{2+} is elevated [50], suggesting that elevated cytosolic free Ca^{2+} can be toxic to yeast. However, we noticed that Ca^{2+} toxicity was blocked by a contaminant present in certain batches of agar (data not shown). The contaminant that blocked Ca^{2+} toxicity was traced to Mg^{2+} because (1) the toxicity blocking activity was abolished by addition of the Mg^{2+} chelator EDTA, (2) crude preparations of agar are known to contain millimolar Mg^{2+}, and (3) pure $MgCl_2$ but not NaCl could block Ca^{2+} toxicity in *pmc1* mutants in standard culture media.

To investigate the mechanism of Mg^{2+} suppression of Ca^{2+} toxicity, the concentration of $CaCl_2$ that caused a 50% inhibition of growth (i.e., the IC_{50} for $CaCl_2$) was determined for *pmc1* mutants after 24 hours of growth standard YPD culture medium supplemented with 0 to 32 mM $MgCl_2$. Remarkably, for *pmc1* knockout mutants the IC_{50} for $CaCl_2$ increased with increasing $MgCl_2$ up to ~8 mM after which the effectiveness of $MgCl_2$ began to decrease (Fig. 3.2A, filled circles). Double mutants lacking both Pmc1 and the vacuolar Ca^{2+}/H^+ exchanger Vcx1 behaved similarly except the IC_{50} values were shifted downward by ~1.6 fold (Fig. 3.2A, open circles). The sole remaining Ca^{2+} transporter Pmr1, a Ca^{2+}/Mn^{2+} ATPase of the Golgi complex, is essential for growth of *pmc1 vcx1* double mutants and is strongly up-regulated by calcineurin [51]. A *pmc1 vcx1 cnb1* triple mutant that also lacks calcineurin exhibited ~2.3 fold lower tolerance to $CaCl_2$ than the *pmc1 vcx1* double mutant and $MgCl_2$ suppressed $CaCl_2$ toxicity over a similar range of concentrations (Fig. 3.2A, filled triangles). A *vcx1 cnb1* double mutant in which Pmc1 and Pmr1 are expressed only at basal levels exhibited ~6.6-fold increase of IC_{50} for $CaCl_2$ as expected and also exhibited $MgCl_2$ suppression of $CaCl_2$ toxicity (Fig. 3.2A, open triangles). These findings demonstrate that $MgCl_2$ suppresses $CaCl_2$ toxicity independent of all known Ca^{2+} transporters, which is consistent with the possibility that Mg^{2+} competitively inhibits one or more Ca^{2+} influx pathways.

[11] Simulation results show that the weighted least square error defined in Eq. 3.10 is quite sensitive to the value of K_{IX}, the reason of which will be further discussed in the second paragraph of Section 3.4. In each optimal fitting, we does not get the same optimal solution. So we choose the best solution with the lowest weighted least square error as defined in Eq. 3.10 after having done a lot of fittings.

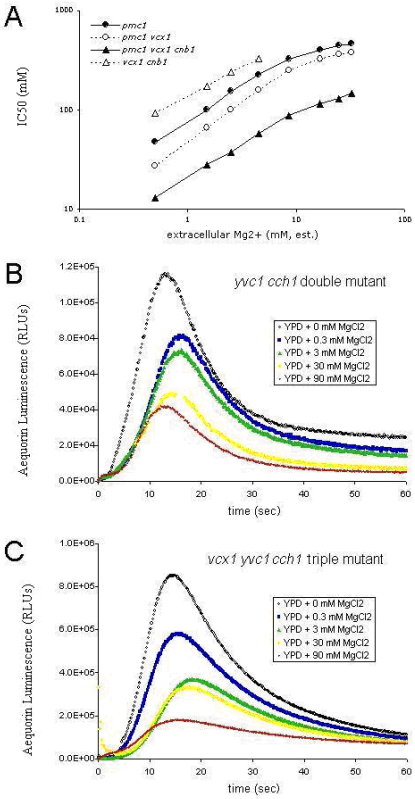

Figure. 3.2. Experimental results. *Panel A*, the concentrations of $CaCl_2$ that caused a 50% inhibition of growth (i.e., the IC_{50} for $CaCl_2$) were shown for *pmc1* (filled circles), *pmc1 vcx1* (open circles), *pmc1 vcx1 cnb1* (filled triangles) and *vcx1 cnb1* (open triangles) mutants after 24 hours of growth standard YPD culture medium supplemented with 0 to 32 mM $MgCl_2$. *Panel B*, A *yvc1 cch1* double mutant expressing apo-aequorin from a plasmid was incubated with coelenterazine co-factor to reconstitute aequorin in situ. The cells bearing reconstituted aequorin were returned to growth medium for an additional 90 minutes, divided into equal aliquots, treated with varying amounts (0, 0.3, 3, 30, 90mM) of $MgCl_2$, placed into a tube luminometer, and monitored for luminescence before and after injection of 800 mM $CaCl_2$. *Panel C,* the corresponding aequorin luminescence curves for *vcx1 yvc1 cch1* mutant.

Two Ca^{2+} channels have been characterized in yeast, the vacuolar Ca^{2+} release channel Yvc1 and the plasma membrane Ca^{2+} influx channel Cch1-Mid1. The *yvc1 cch1 pmc1 vcx1* quadruple mutant exhibited similar levels of $MgCl_2$ suppression of $CaCl_2$ toxicity as the *pmc1 vcx1* double mutants (data not shown), suggesting that Mg^{2+} blocks some other Ca^{2+} influx pathways. To test this possibility directly, cytosolic free Ca^{2+} concentrations were monitored directly after a sudden increase in extracellular $CaCl_2$ by following luminescence of the Ca^{2+}-sensitive photoprotein aequorin. The *yvc1 cch1* double mutant expressing apo-aequorin from a plasmid was incubated with coelenterazine co-factor to reconstitute aequorin in situ. The cells bearing reconstituted aequorin were returned to growth medium for an additional 90 minutes, divided into equal aliquots, treated with

varying amounts of $MgCl_2$, placed into a tube luminometer, and monitored for luminescence before and after injection of 800 mM $CaCl_2$. In the absence of added $MgCl_2$, aequorin luminescence rose quickly after $CaCl_2$ injection, peaked after ~13.3 sec, and declined to a level that was well above the starting level (Fig. 3.2B). Increasing concentrations of $MgCl_2$ progressively lowered the rates of luminescence rise, the maximum achievable luminescence, and the new baseline levels following decline (Fig. 3.2B). Remarkably, the loss of Vcx1 resulted in a dramatic increase in the rate and peak height of aequorin luminescence (Fig. 3.2C). Additionally, the loss of Vcx1 resulted in ~60% slower rate of luminescence decline after the peak regardless of $MgCl_2$ concentration. Though calcineurin inhibits Vcx1 function in long-term growth assays [51], the activity of Vcx1 in these short-term luminescence experiments was not detectably affected by addition of the calcineurin inhibitor FK506 (data not shown). The further loss of Pmc1 also had little effect on aequorin responses (data not shown). These findings identify Vcx1 as the major Ca^{2+}-sequestering transporter in short-term responses to high Ca2+ environments and confirm the hypothesis that Mg^{2+} interferes with one or more novel Ca^{2+} influx pathways. A similar hypothesis was proposed recently to explain the increased Ca^{2+} influx and elevated cytosolic Ca^{2+} concentration observed in yeast upon Mg^{2+} sudden withdrawal [234]. The proteins responsible for Mg^{2+}-sensitive Ca^{2+} influx have not been identified but the Alr, Alr2, and Mnr2 proteins have been identified as hetero-oligomeric proteins required for Mg^{2+} uptake that also promote sensitivity to high environmental Ca^{2+} [134].

3.3.2 Computational Modeling of Ca^{2+} Influx and Sequestration

The multiphasic nature and calcineurin-independence of the aequorin luminescence curves suggested complex dynamics of the novel Ca^{2+} influx pathway(s) as opposed to calcineurin feedback pathways modeled previously (see Chapter 2). To understand these dynamics, a mathematical model was constructed in which the Ca^{2+} transporters Pmr1, Pmc1, and Vcx1 were assumed to function without calcineurin feedback *in vivo* according to standard Michaelis-Menten kinetics. The optimal fitting to the experimental data using a hybrid optimization algorithm (see Section 3.2.3: **Parameter Estimation Method**) shows that simulations assuming two Mg^{2+}-sensitive Ca^{2+} influx transporters (termed transporters M and X) each with distinct properties (as discussed below in more detail) can closely fit the experimental data (see Fig. 3.4A-B and compare them with Fig. 3.2B-C) whereas simulations using just one Mg^{2+}-sensitive Ca^{2+} influx transporter poorly fit the experimental data (see Fig. 3.4C and compare it with Fig. 3.2B).

3.3.2.1 Steady-State Properties

The model for *yvc1 cch1* mutant under hypertonic shock consists of three equations (Eqs. 3.1, 3.4, 3.7, please see Section 3.2.2: **Mathematical modeling**) with three unknowns: $x(t)$, $m(t)$ and $V(t)$. By performing steady state analysis of our model with fixed parameter $[Ca_{ex}]$=800mM, we can first depict the steady state value of $x(t)$ as a function of parameter $[Mg_{ex}]$ as shown in Fig. 3.3A. In general, the resting level of $x(t)$ decreases

almost linearly as $[Mg_{ex}]$ increases. Only in the case of very low $[Mg_{ex}]$ (≤1μM), the curve shows a strange bending.

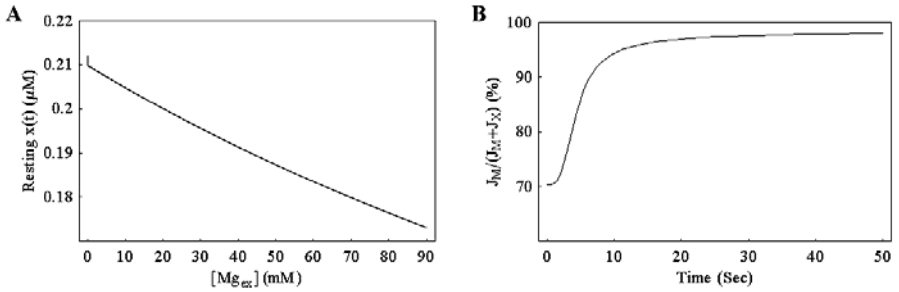

Figure. 3.3. Steady state analysis and flux analysis of the system. *Panel A,* the steady state value of $x(t)$ as a function of parameter $[Mg_{ex}]$ for simulated *yvc1 cch1* mutant in extracellular medium with high calcium concentration (parameter $[Ca_{ex}]$ = 800mM). The simulated cytosolic calcium level of our model *yvc1 cch1* mutant rests within 0.173-0.212μM (regardless of the initial conditions) as the media Mg^{2+} level (parameter $[Mg_{ex}]$) ranges from 0mM to 90mM. *Panel B,* the simulated flux proportion of Transporter M in the total cytosolic Ca^{2+} influx as a function of t for *yvc1 cch1* mutant under hypertonic shock (at $t = 0$, parameter $[Ca_{ex}]$ suddenly increases from 0mM to 800mM and at the same time parameter $[Mg_{ex}]$ suddenly increases from 0 mM to various concentrations. Please note that the curve shown in this graph is for $[Mg_{ex}] = 0mM$. For all the other cases (i.e., $[Mg_{ex}]$ =0.3 mM, 3 mM, 30 mM, 90 mM), the simulated curves coincide with the top frameline (i.e., $J_M/(J_M + J_X) = 100\%$).

3.3.2.2 Transients and Mutant Behavior

By setting reasonable initial conditions ($x(0) = 100nM$, $m(0) = 0M$ and $V(0) = 100\mu M^3$) and then solving the three equations (Eqs. 3.1, 3.4, 3.7, using the parameters listed in Table 3.1) numerically, we can depict the $x(t)$ curves for parameter $[Mg_{ex}]$ suddenly increasing from 0 mM to various concentrations (0 mM, 0.3 mM, 3 mM, 30 mM, 90 mM) at $t = 0$ as shown in Fig. 3.4A (please note that at the same time, parameter $[Ca_{ex}]$ suddenly increases from 0mM to 800mM in these simulations). In general, the simulated $x(t)$ rises due to the hypertonic shock, forms a peak and then declines to a resting value; for higher value of parameter $[Mg_{ex}]$, the peak value of the curve is lower and appears later. For example, by observing the top black curve for parameter $[Mg_{ex}]$=0mM, we can see that due to the hypertonic shock, the simulated $x(t)$ quickly rises (in around 9 seconds) from an initial value of 5,700RLUs (~100nM) to a high peak of around 116,600RLUs (~0.54μM) , then gradually decreases to a value of 46,110RLUs (~0.35μM) when $t = 1\min$. Further investigation shows that it will further decreases to steady state value of 17,500RLUs (~0.21μM). By observing the blue curve for parameter $[Mg_{ex}]$ rising

from 0mM to 0.3mM, we can see that the simulated cytosolic $x(t)$ rises slower than the black curve and its peak value (around 85,200RLUs(~0.47μM)) which appears when $t = 14$ sec is much lower than that of the black curve. However, the green curve for parameter $[Mg_{ex}]$ rising from 0mM to 3mM seems just a little bit lower and slower than the blue curve.

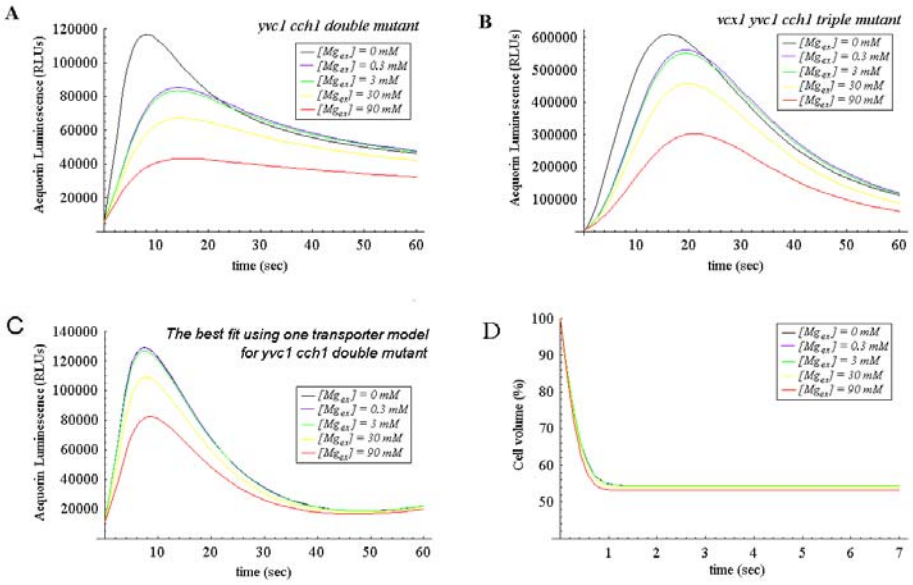

Figure. 3.4. Simulated response curves and volume evolution curves. *Panel A*, the simulated response curves of the best fit using two transporters model for *yvc1 cch1* mutant. The black, blue, green, yellow and red curves depict the simulated $x(t)$ curves for parameter $[Mg_{ex}]$ suddenly increasing from 0 mM to various concentrations (0 mM, 0.3 mM, 3 mM, 30 mM, 90 mM) at $t = 0$ respectively (please note that at the same time $t = 0$ parameter $[Ca_{ex}]$ suddenly increases from 0mM to 800mM in these simulations). *Panel B*, the corresponding simulated response curves using two transporters model for *vcx1 yvc1 cch1* mutant. *Panel C*, the simulated response curves of the best fit using one Mg^{2+}-sensitive transporter model (i.e., in this case we assume that Transporter X is the sole influx pathway) for *yvc1 cch1* mutant. The black, blue, green, yellow and red curves depict the simulated $x(t)$ curves for parameter $[Mg_{ex}]$ suddenly increasing from 0 mM to various concentrations (0 mM, 0.3 mM, 3 mM, 30 mM, 90 mM) at $t = 0$ respectively (please note that at the same time $t = 0$ parameter $[Ca_{ex}]$ suddenly increases from 0mM to 800mM in these simulations). *Panel D*, the simulated volume evolution curves using the two transporters model for *yvc1 cch1* mutant under hypertonic shock (step increase of $[Ca_{ex}]$ from 0mM to 800mM with simultaneous step increase of $[Mg_{ex}]$ to various concentrations). Please note that the black and blue curves coincide with the green curve in this graph.

In Fig. 3.4B, we depict the simulated $x(t)$ curves for *vcx1 yvc1 cch1* triple mutant under hypertonic shock (step increase of $[Ca_{ex}]$ from 0mM to 800mM with simultaneous step increase of $[Mg_{ex}]$ to various concentrations at $t = 0$, please note that V_3 is set to be 0 in these simulations, for the rest parameters please see Table 3.1). By comparison of these

curves with their corresponding curves for simulated *yvc1 cch1* double mutant in Fig. 3.4A, the peak values of these simulated response curves seem much higher. For example, the peak value of the top black curve for $[Mg_{ex}]$=0mM in Fig. 3.4B is around 609,000RLUs (~1.07μM) which is certainly much higher than the peak value 116,600RLUs (~0.54μM) of its corresponding black curve in Fig. 3.4A.

In Fig. 3.4C, the simulated $x(t)$ curves of the best fit using one Mg^{2+}-sensitive transporter model (i.e., Transporter X is assumed to be the only influx pathway) for *yvc1 cch1* mutant under hypertonic shock (step increase of $[Ca_{ex}]$ from 0mM to 800mM with simultaneous step increase of $[Mg_{ex}]$ from 0mM to various concentrations at $t = 0$) are shown. In this figure, the top two curves (i.e., the black curve and the blue curve) coincide with each other. The peak values of the blue, green, yellow, red curves are 129,000RLUs (~0.413μM), 127,000RLUs (~0.41μM), 109,000RLUs (~0.382μM), 82,340RLUs (~0.334μM), respectively. The peaks of both blue and green curves appear when $t = 7.5\,\text{sec}$ whereas the peaks of the yellow and red curves appear at $t = 7.9\,\text{sec}$ and $t = 8.6\,\text{sec}$, respectively.

3.3.2.3 Flux Analysis and Cell Volume Evolution

To discriminate the different influx contributions from two Ca^{2+} influx pathways, in Fig. 3.3B we depict the simulated flux proportion of Transporter M in the total cytosolic Ca^{2+} influx as a function of t for *yvc1 cch1* mutant under hypertonic shock (step increase of $[Ca_{ex}]$ from 0mM to 800mM with simultaneous step increase of $[Mg_{ex}]$ from 0mM to various concentrations at $t = 0$). By observing the black curve for $[Mg_{ex}]$=0mM, we can see that at the beginning, 70.4% of the cytosolic Ca^{2+} influx is contributed by Transporter M and this proportion quickly rises to 98%. The other curves seem to coincide and are flat with a constant value of 100%.

In Fig. 3.4D, the simulated volume evolution curves using to transporters model for *yvc1 cch1* mutant under hypertonic shock (step increase of $[Ca_{ex}]$ from 0mM to 800mM with simultaneous step increase of $[Mg_{ex}]$ from 0mM to various concentrations at $t = 0$) are shown. As we can see in this figure, in general, the cell volume quickly decreases (in about 1 second) to a steady state value of 53-55% percent of the initial volume and the difference among different color curves are quite subtle.

3.3.2.4 Extracellular Mg^{2+} Depletion and Ca^{2+} Challenge

To check the behavior of cytosolic Ca^{2+} level (i.e., $x(t)$) of our model *yvc1 cch1* mutant cell upon extracellular Mg^{2+} depletion, in Fig. 3.5A we depict the simulated $x(t)$ response curve for parameter $[Mg_{ex}]$ suddenly decreasing from 1 mM to 0 mM at $t = 0$ and being reset to 1mM after 90 seconds (parameter $[Ca_{ex}] = 150mM$ in this simulation). From this figure, we can see that when $t = 0$, the simulated cytosolic Ca^{2+} level rises quickly (in 15 seconds) from its original resting level of 0.081μM to a value of 0.099 μM,

almost keeps at that value and recovers quickly to its original resting level of 0.081μM when $t = 1.5\,\text{min}$.

To further check the behavior of cytosolic Ca^{2+} level of our model *yvc1 cch1* mutant cell upon extracellular Ca^{2+} challenge, in Fig. 3.5B we depict the simulated $x(t)$ response curve for parameter $[Ca_{ex}]$ suddenly increasing from 150 mM to 200 mM at $t = 0$ and being reset to 150mM after 90 seconds (parameter $[Mg_{ex}] = 0mM$ in this simulation). From this figure, we can see that the simulated cytosolic Ca^{2+} level rises quickly (in 15 seconds) from its original resting level of 0.091μM to a value of 0.125μM and decreases very gradually to a value of 0.123μM (at $t = 1.5\,\text{min}$), then it decreases quickly to its original resting value.

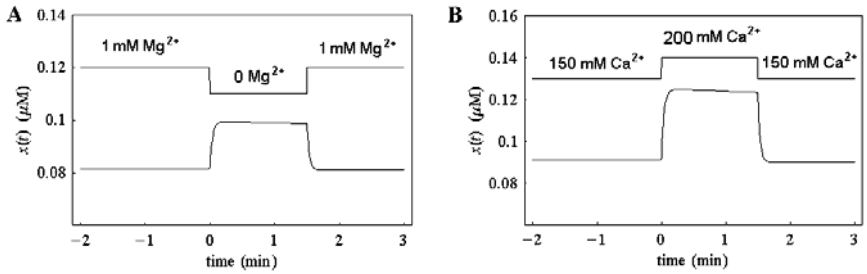

Figure. 3.5. Simulated cytosolic Ca^{2+} level (i.e., $x(t)$) for *yvc1 cch1* mutant increases upon extracellular Mg^{2+} depletion or extracellular Ca^{2+} challenge. *Panel A*, the simulated $x(t)$ response curve (the bottom curve) for parameter $[Mg_{ex}]$ (the top curve) suddenly decreasing from 1 mM to 0 mM at $t = 0$ and being reset to 1mM after 90 seconds (please note that in this simulation, parameter $[Ca_{ex}] = 150mM$). *Panel B*, the simulated $x(t)$ response curve (the bottom curve) for parameter $[Ca_{ex}]$ (the top curve) suddenly increasing from 150 mM to 200 mM at $t = 0$ and being reset to 150mM after 90 seconds (please note that in this simulation, parameter $[Mg_{ex}] = 0mM$). The basal level of $[Ca_{ex}]$ in these two simulations is set to be 150mM instead of 2mM as in Wisenberger's paper [234] because our model is only valid for hypertonic shock (extracellular Ca^{2+} >132mM).

3.4 Discussion

We present experimental data that are consistent with the existence of Mg^{2+}-sensitive Ca^{2+} influx pathways in yeast. Increasing concentrations of extracellular Mg^{2+} increased the concentration of extracellular Ca^{2+} necessary for inhibition of yeast cell growth over a 24 hr period. By extrapolation of log-transformed plots of Mg^{2+} concentration versus IC_{50}, we estimate that standard YPD medium effectively contains 0.5 mM Mg^{2+}, in good agreement with the assayed value of 0.7 mM [2]. Increasing concentrations of extracellular Mg^{2+} also inhibited Ca^{2+} influx as judged by decreasing rates of aequorin luminescence following a sudden increase of extracellular Ca^{2+}. While this work was in

progress, a complementary study also showed that sudden withdrawal of all extracellular Mg^{2+} from synthetic growth medium caused a rapid and reversible influx of Ca^{2+} into yeast cells [234]. An earlier study of $^{45}Ca^{2+}$ influx demonstrated Mg^{2+} inhibition of a constitutive Ca^{2+} influx pathway [132]. Finally, overexpression of the yeast Alr1 or Alr2 Mg^{2+} transporters – homologs of the bacterial CorA Mg^{2+} transporters – resulted in increased sensitivity to high environmental Ca^{2+} [134]. All these results are consistent with a model where Mg^{2+} competitively inhibits one or more Ca^{2+} influx pathways.

As just mentioned, previously published data demonstrate the existence of a constitutive Mg^{2+}-sensitive Ca^{2+} influx pathway, which we called Transporter X [132]. From Fig. 3.2B, we can see that a subtle difference of extracellular Mg^{2+} concentration results in the great difference between the profiles of the black (for $[Mg_{ex}] = 0$) and blue curve (for $[Mg_{ex}] = 0.3mM$). In the case of one transporter model, this can only happen when Transporter X has a very small inhibition constant K_{IX} so that a subtle increase of extracellular Mg^{2+} concentration will have great inhibitory effect on the calcium influx (see Eq. 3.7, please note that $V_m = 0$ for one transporter model. The only influx is through Transporter X which is expressed as $\frac{1}{1+k_b m(t)} \frac{V_x \times [Ca_{ex}]}{K_x(1+[Mg_{ex}]/K_{IX})+[Ca_{ex}]}$. Given fixed V_x, K_x and $[Ca_{ex}]$, smaller K_{IX} can make this influx term more sensitive to the change of $[Mg_{ex}]$). However, a very small K_{IX} will lead to even greater inhibitory effect when $[Mg_{ex}] = 3mM$ or higher concentration. Thus for one transporter model, it either can not reproduce the great difference between the profiles of the black and the blue experimental curves in Fig. 3.2B or can not reproduce the relatively subtle difference between the profiles of the blue and green curves in Fig. 3.2B. However, it is possible for two transporters model to reproduce both differences when in addition to Transporter X with an extremely low K_{IX} which functions only in the case of extremely low extracellular Mg^{2+}, there is another transporter with a high magnesium inhibition constant whose influx is much less sensitive to the change of extracellular Mg^{2+} than that of Transporter X.

As shown in Fig. 3.4C, simulations using just one Mg^{2+}-sensitive Ca^{2+} influx transporter poorly fit the experimental data because the best fit of one Mg^{2+}-sensitive transporter model (see Fig. 3.4C) using hybrid optimization algorithm can not reproduce the great difference between the black and blue experimental curves shown in Fig. 3.2B whereas simulations assuming two Mg^{2+}-sensitive Ca^{2+} influx transporters (termed transporters X and M with very distinct inhibition constants: $K_{IX} = 3.51*10^{-6}$ μM and K_{IM} =149.18 mM) can closely fit the experimental data (see Fig. 3.4A and Fig. 3.4B). All these results confirm the theoretical analysis in the previous paragraph and our simulation results strongly suggest the existence of a new transporter named Channel M on the *yvc1 cch1* mutant. As shown in Fig. 3.3B, for $[Mg_{ex}]$=0 (see the black curve in Fig. 3.3B), both transporters M and X make considerable contribution to the total Ca^{2+} influx whereas for

relatively high $[Mg_{ex}]$ (see Fig. 3.3B) the flux contribution of Transporter X becomes negligible. The strange bending shown in Fig. 3.3A appears because of the opening of Transporter X in the case of extremely low $[Mg_{ex}]$.

A mathematical model of Transporter M and other components of the system was constructed here. By comparison of simulated response curves in Fig. 3.4A with corresponding experimental curve in Fig. 3.2B for *yvc1 cch1* mutant, we can see that the numerical simulations of our model do can quantitatively reproduce the main characteristics of the experimental results such as low levels of extracellular Mg^{2+} can slow Ca^{2+} influx and diminish cytosolic free Ca^{2+} elevation. The model assumed that Transporter M has very low affinity for Ca^{2+} (K_m = 505.43 mM), competitive inhibition by extracellular Mg^{2+} (K_{IM} = 149.18 mM), and rapid feedback inhibition by intracellular Ca^{2+}. The mechanism of feedback was found to be independent of calcineurin but otherwise its components remain wholly unknown. The relatively low affinity for Ca^{2+} relative to Mg^{2+} also suggests that Transporter M may function primarily as a Mg^{2+} transporter in physiological conditions. If so, the cellular response to high extracellular Ca^{2+} may include Mg^{2+} starvation in addition to Ca^{2+} influx, as suggested recently [234]. It is very likely that both transporters M and X are homo/hetero-oligomers of Alr1, Alr2 and Mnr2 - uniporters primarily involved in Mg^{2+} uptake (Please note that uniporter is an inetgral membrane protein that is involved in facilitated diffusion whose uptake behavior can be well described with Michaelis-Menton kinetics [5]). A more realistic understanding of Transporter M and Transporter X should be possible after their genes and regulators are identified and characterized.

The computer simulations (see Fig. 3.4A and Fig. 3.4B) also reproduced the experimentally determined effects of the vacuolar H^+/Ca^{2+} exchanger Vcx1 on cytosolic free Ca^{2+} dynamics. The presence or absence of calcineurin inhibitor had no effect on the aequorin traces in the presence or absence of Vcx1 (data not shown), suggesting no significant inhibition of Vcx1 by calcineurin within three minutes following Ca^{2+} shock. In long-term growth experiments, calcineurin appears to strongly inhibit Vcx1 function in addition to strongly inducing Pmc1 function [51]. Perhaps these effects of calcineurin can be observed in aequorin experiments performed over longer time scales and used to computationally model the long-term effects of Ca^{2+} on yeast growth (Fig. 3.2A).

From Fig. 3.4d, we can see that the shrinkage of our simulated *yvc1 cch1* model cell is quickly accomplished (in less than 1 second). More simulations show that the volume shrinkage rate of our model cell is mainly determined by the reflection coefficient σ, the value of which used here (i.e., 0.035) is actually a value for sorbitol obtained by fitting the experimental curve [56]. Although the reflection coefficient σ for the current solute is not exactly known, further investigations show that the value of σ (in the investigations, we let this value range from 1000 to 0.001) seems to have insignificant influence on our main simulation results shown in Fig. 3.3 and Fig. 3.4A-C.

Wisenberger *et al.* reported in their experimental paper [234] that removal of Mg^{2+} in extracellular medium (with the presence of extracellular Ca^{2+}) resulted in an immediate

increase in free cytoplasmic Ca^{2+} and this signal was reversible. As we can see from Fig. 3.5A, the sudden step decrease of $[Mg_{ex}]$ from 1mM to 0mM at $t = 0$ incurs an immediate quick rise of simulated cytosolic Ca^{2+} level (i.e., $x(t)$) and after parameter $[Mg_{ex}]$ is reset to 1mM at $t = 1.5\,\text{min}$, simulated cytosolic Ca^{2+} drops and recovers to its original resting level. Moreover, by comparison of two simulated response curves shown in Fig. 3.5A and Fig. 3.5B, we can see that the manner of the behavior of the simulated cytosolic Ca^{2+} level under Mg^{2+} depletion is quite similar to that under Ca^{2+} challenge. All these simulation results show that our model can reproduce (although roughly) the relevant experimental results reported by Wisenberger *et al* [234].

Finally there are still two issues worthy of discussion here. The first issue is about the reversibility of Ca^{2+} sequestration through Vcx1 and Pmc1. Intuitively there should exist a Ca^{2+} efflux from the vacuole into the cytosol. However, this is not the case for yeast cells. Dunn *et al.* (1994) ever measured the rate of Ca^{2+} efflux from yeast vacuoles both *in vitro* and *in vivo* [63]. Their experiments indicated that *in vivo* vacuolar Ca^{2+} efflux is very low (essentially zero). We think that it is more appropriate to use standard Michaelis-Menten kinetics (as we did here) rather than reversible Michaelis-Menten kinetics to describe the uptake behavior of Vcx1 and Pmc1 because the later kinetics will introduce an unreal vacuolar Ca^{2+} efflux. The second issue is about the validity of using Michaelis-Menten kinetics for modeling the uptake behavior of the transporters M and X. It is well-known that Michaelis-Menten kinetics assumes a rapid equilibrium between the enzyme and substrate to form an intermediate complex [58]. So we need to check if the uptake of Ca^{2+} and Mg^{2+} through the transporters is fast enough that it could be considered as steady-state at all times. Ion channels enable rapid ($\sim 10^7$ ion s^{-1}) movement of selected ions through pores in biological membranes [19]. Ca^{2+} channel can recognize its substrate and let it permeate within 10-100ns [144]. Carriers (i.e., transporters) are characterized by turnover numbers that are typically 1,000-fold lower than ion channels [117]. This means the average time needed for a Ca^{2+} to pass through the plasma membrane via the help of an ion transporter is within 10-100μs, which is several order smaller than the time frame (in seconds) of the Ca^{2+} peaks shown in Fig. 3.2B and Fig. 3.2C. Moreover, Michaelis-Menten kinetics has been used in a mathematical model for describing the iron uptake behavior of plasma membrane iron transporter in the iron homeostasis system of *E. coli* (see the first term in Eq.1 in Ref. 191). So here we think that it is appropriate to use Michaelis-Menten kinetics for modeling the uptake behavior of the transporters M and X.

As mentioned before, the mathematical model presented here is only valid for a short lapse (about three minutes) following the hypertonic Ca^{2+} shock. This model needs to be modified for low extracellular Ca^{2+} (<132mM) because Eq. 3.4 is only valid for hypertonic shock and it does not include factors such as turgor pressure which will arise in the case of low extracellular Ca^{2+}. Moreover, for simplicity, this model assumes direct inhibition of Ca^{2+}-bound calmodulin on both two transporters M and X, which is not backed by any experimental data. In the real cells, the relevant feedback regulation pathways may be more complicated. And the relative coarseness of the model accounts for the differences (e.g., the noticeable bias in the downward phase of the peak) shown by the comparison of Fig. 3.2B with Fig. 3.4A (also by comparison of Fig. 3.2C with Fig.

3.4B). On the other hand, the novelty of the present work lies in that by combining computational and experimental methodology, we detect the existence of a new Mg^{2+}-sensitive Ca^{2+} transporter named as Transporter M on the yeast plasma membrane of *yvc1 cch1* mutant cell working together with previously found Transporter X under hypertonic Ca^{2+} shock. The eventual accomplishment of a complete and accurate mathematical model of dynamic Ca^{2+} signaling networks in yeast will facilitate similar endeavors in all cell types and organisms, but doing so still requires additional mechanistic insights obtained from the fusion of experimental data and mathematical models.

In this chapter, we have revised and extended the first preliminary model for yeast calcium homeostasis (see Chapter 2) and developed a new mathematical model that omitted calcineurin-dependent feedback and instead included rapid Ca^{2+}-dependent feedback inhibition of Ca^{2+} influx pathways to simulate complex cytosolic free Ca^{2+} dynamics of *yvc1 cch1* yeast cells under hypertonic shock. The validity of the model was confirmed by its ability of reproducing the experimental data (including the experimentally determined effects of Vcx1 on cytosolic free Ca^{2+} dynamics) and simulating the effects of extracellular Mg^{2+} removal. Both models presented in Chapter 2 and Chapter 3 consist of several nonlinear ODEs which seem relatively simple. In Chapter 4, we will describe a much more complicated model for describing calcineurin-dependent calcium signaling network in cardiac myocytes of mice.

Chapter 4 Simulating Complex Calcium-Calcineurin Signaling Networks in Cardiac Myocytes[12]

4.1 Introduction:

As mentioned in Section 1.3.4.1, it has been recently recognized that calcium plays a central role in the control of heart growth through a complex calcium-calcineurin-MCIP-NFAT signaling network (see Fig. 4.1). The heart responds to physiological and pathological stimuli by hypertrophic growth [224, 225]. Cardiac hypertrophy is a thickening of the heart muscle (myocardium) resulting in a decrease in size of the ventricles. Prolonged pathological hypertrophy may progress to heart failure and significantly increase the risk for sudden death. Thus deciphering the details of the signaling pathways involved in cardiac hypertrophy and understanding their quantitative dynamics through computational modeling will be critical for devising therapeutic drugs for the treatment of heart disease [225].

[12] This Chapter is based on: Jiangjun Cui and Jaap Kaandorp, Simulating complex calcium-calcineurin signaling network, in M.T. Bubak; G.D. van Albada; J.J. Dongarra and P.M.A. Sloot, editors, *Computational Science - ICCS 2008: 8th International Conference, Krakow, Poland, Proceedings, Part III*, in series *Lecture Notes in Computer Science*, vol. 5103, pp. 110-119. Springer, Berlin, Heidelberg, June 2008.

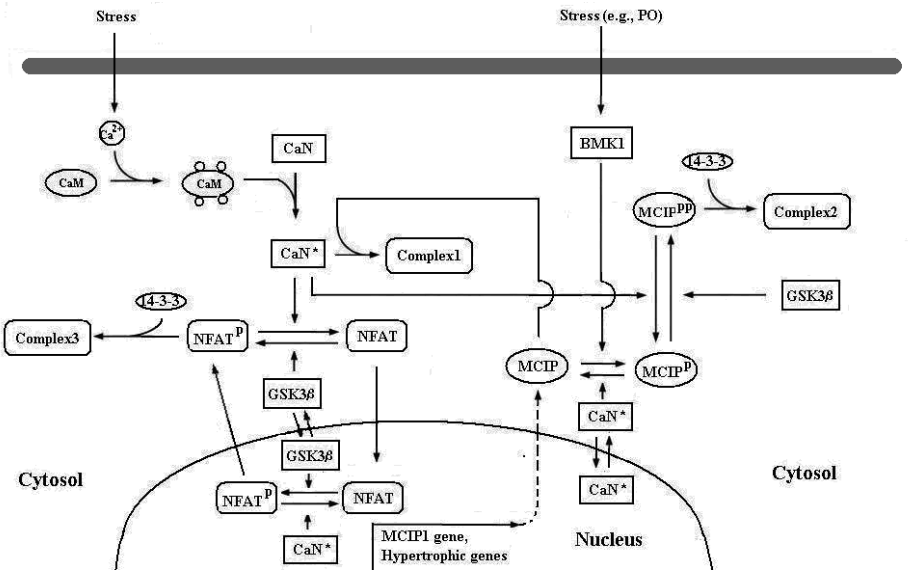

Figure. 4.1. A schematic graph depicting the Ca^{2+}-calcineurin-MCIP-NFAT signaling networks in cardiac myocytes.[13]

As shown in the left-up corner of Fig. 4.1, stress incurs the influx of Ca^{2+}, which binds to CaM (4:1). Ca^{2+}-bound CaM binds to CaN to activate it [175]. CaN^* (i.e., activated CaN) can bind to MCIP to form Complex1 [225,226]. CaN^* can also work as the enzyme to convert $NFAT^P$ into NFAT [148]. Another enzyme GSK3β works in the reverse conversion of NFAT into $NFAT^P$, which can bind to 14-3-3 to form Complex3 [13,130]. Such conversion between NFAT and $NFAT^P$ with the help of two enzymes (GSK3β and CaN^*) also happen in the nucleus [91]. NFAT in the cytosol will be imported into the nucleus and $NFAT^P$ in the nucleus will be exported into the cytosol. The nuclear NFAT can initiate the transcription of the hypertrophic genes and the gene encoding MCIP (more precisely, MCIP1, a form of MCIP) [91,239]. Both GSK3β and CaN^* are shuttled between the nucleus and the cytosol [91, 183]. As shown in the right-up corner of Fig. 4.1, particular stress such as PO can activate BMK1 [214], which catalyzes the conversion of

[13] Abbreviations are as follows: calmodulin (CaM); calcineurin (CaN); activated calcineurin (CaN^*); nuclear factor of activated T-cells (NFAT); phosphrylated NFAT($NFAT^P$); modulatory calcineurin-interacting protein (MCIP); phosphorylated MCIP on serine 112 ($MCIP^P$); phosphorylated MCIP on both serine 112 and serine 108 ($MCIP^{PP}$); big mitogen-activated protein kinase 1 (BMK1); glycogen synthase 3β (GSK3β); the complex formed by MCIP and calcineurin(Complex1); the complex formed by $MCIP^{PP}$ and 14-3-3 (Complex2); the complex formed by $NFAT^P$ and 14-3-3 (Complex3); pressure overload (PO); hypertrophic stimuli (stress).

MCIP into $MCIP^P$ [1], $MCIP^P$ can be converted into $MCIP^{PP}$ by GSK3β. The reverse conversion of $MCIP^{PP}$ into $MCIP^P$ is again catalyzed by CaN^* [226]. $MCIP^{PP}$ will bind with 14-3-3 to form Complex2 [1].

MCIP1 seems to facilitate or suppress cardiac CaN signaling depending on the nature of the stress (see Fig. 4.2a). In the case of CaN^* transgenic mice, the knock-out of MCIP1 gene (i.e., MCIP $^{-/-}$ TG mice) exacerbated the hypertrophic response to CaN^* overexpression. Paradoxically, however, cardiac hypertrophy in response to PO was blunted in normal MCIP $^{-/-}$ mice [101,225].

In 2006, Shin *et al*. [196] published a paper in FEBS Letters using switching feedback mechanism to explain this dual role of MCIP in cardiac hypertrophy. The aim of this Chapter is to propose a much-extended version of Shin's model by including more recent experimental findings. The construction of the model is based on biochemical principles and we use an open source software (Cellerator) to automatically generate the equations. As we will see later, this model can correctly predict the mutant ($MCIP1^{-/-}$) behavior under different stress such as PO and CaN^* overexpression.

4.2 Method:

4.2.1 Cellerator Software

Cellerator™ is a Mathematica® package designed to facilitate biological modeling via automated equation generation [194, 245]. It uses an arrow-based reaction notation to represent biochemical networks and is especially amenable for simulating signal transduction networks.

For example, a catalytic biochemical reaction ($S+E \underset{r2}{\overset{r1}{\rightleftharpoons}} SE \xrightarrow{r3} P+E$, which means enzyme E catalyzes the conversion of S into P, where r1, r2, r3 are the rate constants and SE is the intermediate complex formed by S and E [58]) can be represented as $\left\{S \overset{E}{\rightleftharpoons} P,\ r1,\ r2,\ r3\right\}$ in Cellerator form. The detailed ODEs notation of this reaction are:

$$\frac{dS}{dt} = -r1 * E * S + r2 * SE, \frac{dP}{dt} = r3 * SE, \frac{dE}{dt} = -\frac{dSE}{dt} = -r1 * E * S + (r2 + r3) * SE$$

In our system shown in Fig. 4.1, the conversion of MCIP into $MCIP^P$ catalyzed by BMK1 can be represented as $\left\{MCIP \overset{BMK1}{\rightleftharpoons} MCIPp,\ k7,\ k8,\ k9\right\}$ in Cellerator form where MCIPp denotes $MCIP^P$ and $k7$, $k8$, $k9$ are the relevant rate constants.

4.2.2 Representation of Relevant Reactions

The complex Ca^{2+}-calcineurin signaling network shown in Fig. 4.1 can be represented using 17 reactions in addiction to a transcription control process of MCIP by NFAT. For clarity, we can group all 17 relevant reactions into four categories (simple irreversible,

simple reversible, reversible binding and catalytic binding reactions) which are shown in the following Table 4.1.

Table 4.1: The Representation of relevant reactions of the system [14]

Reaction Category	Biochemical Form	Cellerator Form	Reaction No.	Cellerator Form of Particular Reactions
Simple Irreversible	$A \xrightarrow{r} B$	{A → B, r}	(1)	{NFATc → NFATn, k29}
			(2)	{NFATpn → NFATpc, k30}
Simple Reversible	$A \underset{r2}{\overset{r1}{\rightleftharpoons}} B$	{A ⇄ B, r1, r2}	(3)	{GSK3βc ⇄ GSK3βn, k31, k32}
			(4)	{CaNc* ⇄ CaNn*, k33, k34}
Reversible Binding	$A+B \underset{r2}{\overset{r1}{\rightleftharpoons}} C$	{A+B ⇄ C, r1, r2}	(5)	{CaM + Ca^4 ⇄ CaMCa, k1, k2}
			(6)	{CaMCa + CaNc ⇄ CaNc*, k3, k4}
			(7)	{CaNc* + MCIP ⇄ Comp1, k5, k6}
			(8)	{P1433 + MCIPpp ⇄ Comp2, k19, k20}
			(9)	{NFATpc + P1433 ⇄ Comp3, k27, k28}
Catalytic Binding	$S+E \underset{r2}{\overset{r1}{\rightleftharpoons}} SE$ $SE \xrightarrow{r3} P+E$	$\left\{S \overset{E}{\rightleftarrows} P, r1, r2, r3\right\}$	(10)	$\left\{MCIP \overset{BMK1}{\rightleftarrows} MCIPp, k7, k8, k9\right\}$
			(11)	$\left\{MCIPp \overset{CaNc^*}{\rightleftarrows} MCIP, k10, k11, k12\right\}$
			(12)	$\left\{MCIPp \overset{GSK3\beta c}{\rightleftarrows} MCIPpp, k13, k14, k15\right\}$
			(13)	$\left\{MCIPpp \overset{CaNc^*}{\rightleftarrows} MCIPp, k16, k17, k18\right\}$
			(14)	$\left\{NFATpc \overset{CaNc^*}{\rightleftarrows} NFATc, k21, k22, k23\right\}$
			(15)	$\left\{NFATc \overset{GSK3\beta c}{\rightleftarrows} NFATpc, k24, k25, k26\right\}$
			(16)	$\left\{NFATpn \overset{CaNn^*}{\rightleftarrows} NFATn, k35, k36, k37\right\}$
			(17)	$\left\{NFATn \overset{GSK3\beta n}{\rightleftarrows} NFATpn, k38, k39, k40\right\}$

[14] Abbreviations and synonyms used in this table are as follows: $MCIP^P$ (MCIPp); $MCIP^{PP}$ (MCIPpp); $NFAT^P$ (NFATp); cytosolic NFAT (NFATc); cytosolic NFATp (NFATpc); cytosolic inactive CaN (CaNc); cytosolic CaN^* ($CaNc^*$); cytosolic GSK3β (GSK3βc); nuclear NFAT (NFATn); nuclear NFATp (NFATpn); nuclear CaN^* ($CaNn^*$); nuclear GSK3β (GSK3βn); 14-3-3 protein (P1433); Ca^{2+}-bound CaM (CaMCa); Complex1 (Comp1); Complex2 (Comp2); Complex3 (Comp3).

4.2.3 The Equations of the Model

The model consists of 28 equations concerning 28 unknowns including $Ca(t)$ which denotes the cytosolic Ca^{2+} concentration. Since calcineurin is unique in its specific responsiveness to sustained, low frequency calcium signals [224], we will assume cytosolic Ca^{2+} concentration as a constant in the following simulations as Shin *et al.* [196] did in their simulations. Then we need to further consider modeling the transcription control process of MCIP by NFAT. We have added the following equation to replace the equation of $Ca(t)$ in our model:

$$\frac{dMRNA(t)}{dt} = k41 * NFATn(t) - k42 * MRNA(t) \tag{4.1}$$

Where $MRNA(t)$ denotes the mRNA concentration of MCIP and $k41$ is the control constant, $k42$ is the degradation constant [242]. Moreover, we need to add an additional production term ($k43 * MRNA(t)$) and a degradation term ($(\ln 2 / t_{1/2}) * MCIP(t)$) in the rate equation of $MCIP(t)$ where $t_{1/2}$ denotes the half-life time constant of MCIP. Thus eventually we have completed building of our computational model which consists of 28 ODEs for 28 unknowns. The relevant parameters except parameter Ca ,which denotes cytosolic calcium concentration, are listed in Table 4.2.

Table 4.2: Rate constants and other parameters of the model[15]

Parameters	Value		Parameter	Value
$k1$	5 $\mu M^{-4} \cdot min^{-1}$		$k24$	0.1 $\mu M^{-1} \cdot min^{-1}$
$k2$	100 min^{-1}		$k25$	0.15 min^{-1}
$k3$	2760 $\mu M^{-1} \cdot min^{-1}$ [175]		$k26$	0.1 min^{-1}
$k4$	0.072 min^{-1} [175]		$k27$	0.4 $\mu M^{-1} \cdot min^{-1}$
$k5$	50 $\mu M^{-1} \cdot min^{-1}$		$k28$	0.1 min^{-1}
$k6$	0.0567 min^{-1} [196]		$k29$	0.4 min^{-1} [183]
$k7$	5 $\mu M^{-1} \cdot min^{-1}$		$k30$	0.1 min^{-1} [183]
$k8$	0.1 min^{-1}		$k31$	0.1 min^{-1}

[15] In this table, $t_{1/2}$ denotes the half-life time of MCIP1. $[CaN_{tot}]$ denotes total concentration of calcineurin. $[NFAT_{tot}]$ denotes total concentration of NFAT.

$k9$	0.5 min^{-1}		$k32$	0.05 min^{-1}
$k10$	0.1 $\mu M^{-1} \cdot min^{-1}$		$k33$	0.114 min^{-1} [195]
$k11$	0.1 min^{-1}		$k34$	0.0552 min^{-1} [195]
$k12$	0.1 min^{-1}		$k35$	0.15 $\mu M^{-1} \cdot min^{-1}$
$k13$	0.5 $\mu M^{-1} \cdot min^{-1}$		$k36$	0.1 min^{-1}
$k14$	0.5 min^{-1}		$k37$	0.2 min^{-1}
$k15$	0.1 min^{-1}		$k38$	0.1 $\mu M^{-1} \cdot min^{-1}$
$k16$	0.1 $\mu M^{-1} \cdot min^{-1}$		$k39$	0.1 min^{-1}
$k17$	0.1 min^{-1}		$k40$	0.1 min^{-1}
$k18$	0.1 min^{-1}		$k41$	0.02 min^{-1}
$k19$	0.5 $\mu M^{-1} \cdot min^{-1}$		$k42$	0.03 min^{-1}
$k20$	0.1 min^{-1}		$k43$	0.03 min^{-1}
$k21$	0.15 $\mu M^{-1} \cdot min^{-1}$		$t_{1/2}$	15 min [177]
$k22$	0.15 min^{-1}		$[CaN_{tot}]$	1 μM [24,196]
$k23$	0.1 min^{-1}		$[NFAT_{tot}]$	0.017 μM [15,196]

The initial condition used for the simulations is as follows (Units are in μM):

$$BMK1(0) = 0.012, MRNA(0) = 3.33*10^{-4}, CaM(0) = 25.2, CaMCa(0) = 7.88*10^{-7},$$
$$CaNc(0) = 0.91, CaNc^{*}(0) = 0.0275, CaNn^{*}(0) = 0.0568, Comp1(0) = 5.21*10^{-3},$$
$$Comp2(0) = 0.283, Comp3(0) = 0.014, GSK3\beta c(0) = 0.17, GSK3\beta n(0) = 0.339,$$
$$MCIP(0) = 2.15*10^{-4}, MCIPp(0) = 7.76*10^{-3}, MCIPpp(0) = 0.0798, P1433(0) = 0.708,$$
$$NFATc(0) = 2*10^{-5}, NFATn(0) = 4.99*10^{-4}, NFATpc(0) = 4.94*10^{-3}, NFATpn(0) = 8.01*10^{-5},$$
$$NFATc \cup GSK3\beta c(0) = 1.36*10^{-6}, NFATn \cup GSK3\beta n(0) = 8.46*10^{-5},$$
$$MCIPp \cup GSK3\beta c(0) = 1.1*10^{-3}, MCIP \cup BMK1(0) = 2.14*10^{-5},$$
$$MCIPpp \cup CaNc^{*}(0) = 1.1*10^{-3}, MCIPp \cup CaNc^{*}(0) = 1.07*10^{-4},$$
$$NFATpn \cup CaNn^{*}(0) = 2.27*10^{-6}, NFATpc \cup CaNc^{*}(0) = 8.15*10^{-5}$$

It is easy to verify that this initial conditions satisfies the constraints of $[NFAT_{tot}] = 0.017\mu M$ and $[CaN_{tot}] = 1\mu M$. (Please note that here $MCIP \cup BMK1(0)$ denotes the initial concentration of intermediate complex formed by MCIP and BMK1).

4.3 Results

With this model, the next question is how to simulate the stimulus. Similar as Shin *et al.* did in their paper, we simulate stimulus of PO by setting parameter Ca to a smaller constant (0.2μM). Moreover, at the same time we increase the initial value of $BMK1(t)$ from 0.012μM to 1.2 μM because PO activates BMK1 [214]. The stimulus of CaN^{*} overexpression is simulated by setting parameter Ca to a bigger constant (0.4μM) and simultaneously increasing the initial value of $CaNc^{*}(t)$ from 0.0275μM to 0.825 μM.

4.3.1 Steady-state Property

By numerically solving the equations using the parameters listed in Table 4.2, simulations show that the system does evolve to a steady state. Actually the above initial condition is a selected steady state for simulating the normally growing heart cells with parameter $Ca = 0.05\mu M$. In Fig. 4.2b, the steady-state value increase of nuclear NFAT (i.e., $NFATn^{*}(t)$) under the different stimuli for simulated $MCIP^{+/+}$ and $MCIP^{-/-}$ heart cells are shown. By comparison of the first two bars in this figure, we can see that PO causes greater increase of the steady-state value of nuclear NFAT in simulated normal cells than in simulated MCIP mutant cells. However, the comparison of the third bar with the fourth bar tells us that CaN^{*} overexpression incurs much less increase of the steady state value of nuclear NFAT in simulated normal cells than in simulated $MCIP^{-/-}$ cells.

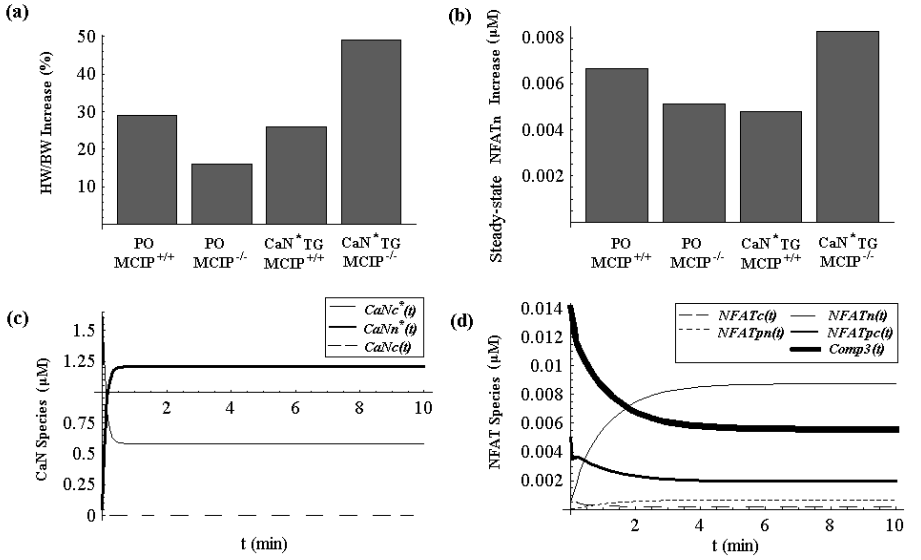

Figure. 4.2. Hypertrophic response and simulated transient curves for CaN* TG animals. (a) The stimuli of pressure overload (PO) caused more severe hypertrophy in normal animals (the first bar) than in MCIP$^{-/-}$ animals (the second bar) whereas the stimuli of CaN* overexpression (expressed from a muscle-specific transgene) incurred much more HW/BW (heart weight normalized to body weight) increase in MCIP$^{-/-}$ transgenic (TG) mice (the fourth bar) than in normal transgenic mice (the third bar). (b) The simulated value increase of steady-state nuclear NFAT under the different stimuli of PO and CaN* overexpression. (c) Simulated CaN species concentration as a function of t in the case of CaN* overexpression for MCIP$^{-/-}$ animals. Thin solid line: $CaNc^*(t)$; thick solid line: $CaNn^*(t)$; Dashed line: $CaNc(t)$. (d) Simulated NFAT species concentration as a function of t in the case of CaN* overexpression for MCIP$^{-/-}$ animals. Thin solid line: $NFATn(t)$; thick solid line: $NFATp(t)$; extremely thick solid line: $Comp3(t)$;sparsely dashed line: $NFATc(t)$; densely dashed line: $NFATpn(t)$.

4.3.2 Transients and Mutant behavior

In Fig. 4.3, critical transient curves in the case of CaN* overexpression for simulated MCIP$^{+/+}$ cells are shown. From Fig. 4.3a, we can see that due to overexpression, cytosolic CaN* quickly (in less than 4 minutes) rises to high peak of 1.3 μM, drops a bit more slowly to around 0.6 μM and then very gradually declines (it eventually rests at a level of 0.353 μM). From Fig. 4.3b, we can see that the concentration of MCIP^{PP} gradually decreases from 0.0798 μM to almost 0, whereas the concentration of MCIP^{P} rapidly rises to a peak value of 0.036 μM and then gradually declines. From Fig. 4.3c, we can see that the concentration of Complex2 gradually declines from 0.283 μM to a resting level of 0.025 μM whereas the concentration of Complex1 increases from almost 0 to around 0.5 μM in 50 hours (it will eventually rests at 0.71 μM). The concentration of 14-3-3 gradually rises from 0.71 μM to 0.97 μM. From Fig. 4.3d, we can see that the concentration of nuclear NFAT quickly rises to a peak value of 7.6 nM and then gradually declines (it will eventually rests at 5.3 nM) whereas cytosolic NFATp

decreases quickly from 4.9 nM to 2 nM and then gradually recovers to a new resting level of 2.5 nM. The concentration of Complex3 quickly decreases from 14nM to 7nM and then gradually recovers to 7.1nM.

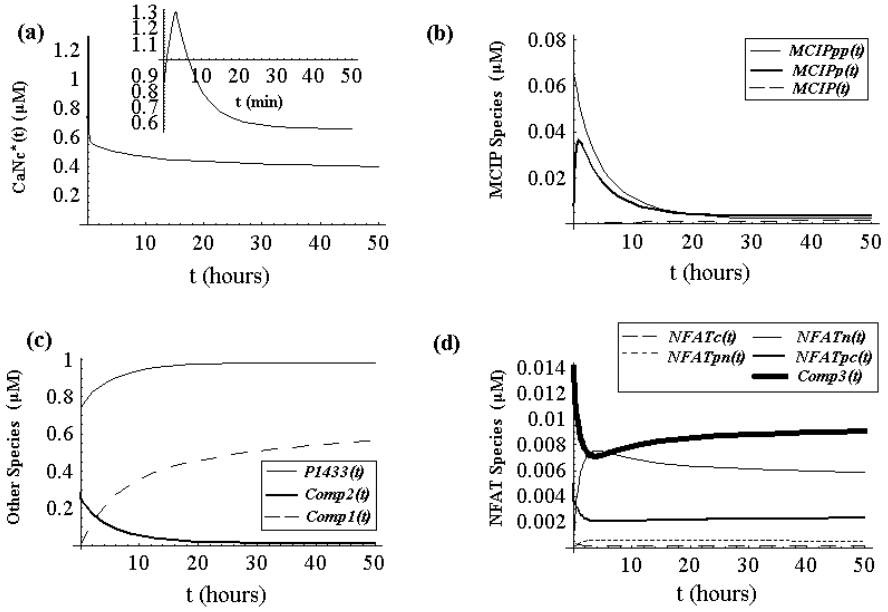

Figure. 4.3. Simulated transient curves for normal animals under the stimulus of CaN* overexpression. (a) Simulated $CaNc^*(t)$ (i.e., cytosolic CaN*) as a function of t. The small figure in the right-up corner shows the detailed change of $CaNc^*(t)$ during the first 50 minutes. (b) Simulated concentration of MCIP species as a function of t. Thin solid line: $MCIPpp(t)$; thick solid line: $MCIPp(t)$; dashed line: $MCIP(t)$; (c) Simulated concentration of some other species as a function of t. Thin solid line: $P1433(t)$; thick solid line: $Comp2(t)$; dashed line: $Comp1(t)$. (d) Simulated NFAT species concentration as a function of t. Thin solid line: $NFATn(t)$; thick solid line: $NFATpc(t)$; extremely thick solid line: $Comp3(t)$;sparsely dashed line (bottom): $NFATc(t)$; densely dashed line: $NFATpn(t)$.

Similarly, we can perform numerical simulations for the MCIP$^{-/-}$ animals. Fig. 4.2c and Fig. 4.2d show the transient curves of the main CaN species and NFAT species under the stimulus of CaN* overexpression. From Fig. 4.2c, we can see that due to CaN* overexpression, cytosolic inactive CaN (i.e., $CaNc(t)$) quickly decreases from 0.091 μM to 0 and cytosolic CaN* rises extreme quickly (actually in less than 0.01 minutes) from 0.825 μM to high peak of more than1.6 μM and then quickly declines to a resting level of 0.58 μM whereas nuclear CaN* quickly rises from 0.057 μM to 1.21 μM. From Fig. 4.2d, we can see that nuclear NFAT steadily increases from 0.5nM to a resting level of 8.8 nM whereas cytosolic NFATp extreme quickly drops from 4.9 nM to 3.8 nM and then gradually declines to 1.9nM.

4.4 Discussion

The decrease of Complex2 shown in Fig. 4.3C indicates the accelerated dissociation of Complex2 which should produce more $MCIP^{PP}$ (see Reaction 8 in Table 4.1). However, from Fig. 4.3b, we can see that $MCIP^{PP}$ is actually decreasing. Since only two reactions (Reaction 8 and 13) can cause the decrease of $MCIP^{PP}$, so the only feasible explanation is that the initial sudden rise of cytosolic CaN^{*} catalyzes the conversion of $MCIP^{PP}$ to $MCIP^{P}$ and then to MCIP and the resultant depletion of $MCIP^{PP}$ promotes the dissociation of Complex2 which also causes the concentration rise of 14-3-3 as seen in Fig. 4.3c. Similarly, the sudden decrease of Comp3 should release more $NFAT^{P}$ (see Reaction 9 in Table 4.1). However, as we can see from Fig. 4.3d, $NFAT^{P}$ concentration is at first rapidly decreasing. So the only feasible explanation is the initial sudden rise of cytosolic CaN^{*} catalyzes the conversion of cytosolic $NFAT^{P}$ to NFAT and the resultant depletion of cytosolic $NFAT^{P}$ promotes the dissociation of Complex3. The accelerated cytosolic $NFAT^{P}$ to NFAT also results in the translocation of NFAT into the nucleus which explains the increases of nuclear NFAT which will promotes the expression of MCIP. The increasing formation of Complex1 shown in Fig. 4.3c indicates that the MCIP converted from $MCIP^{P}$ and the newly expressed MCIP associate with cytosolic CaN^{*}, which leads to its depletion as shown in Fig. 4.3a (obviously the intial rise of cytosolic CaN^{*} concentration in the first several minutes is due to the increased level of cytosolic Ca^{2+} which binds with calmodulin to further activate cysolic CaN). Since in first 50 hours, the total increase of Complex1 concentration (about 0.5 μM) is greater than the total decrease (less than 0.4 μM) of the concentrations of three MCIP species shown in Fig. 4.3b and Complex2, we can conclude that a significant source of MCIP consumed in the process of increasing formation of Complex1 is from newly expressed MCIP. The increasing formation of Complex1 also consumes cytosolic CaN^{*} and realizes the inhibition of MCIP on calcineurin (CaN) activity. In simulated MCIP $^{-/-}$ cells, due to the lack of MCIP, nuclear NFAT increases to a much higher level (8.8nM) than in MCIP $^{+/+}$ cells (5.3 nM) as shown in Fig. 4.2d. Also it takes much less time for the system to evolve to new steady state.

Similarly, the simulations in the case of PO stimulus show that in normal cells, PO causes the increase of Comlex2 formation (from 0.28 μM to 0.96 μM) and the decrease of free 14-3-3 concentration (from 0.71 μM to 0.048 μM). The formation of Complex2 consumes $MCIP^{PP}$ and promotes the conversion of MCIP to $MCIP^{P}$ then to $MCIP^{PP}$. In simulated MCIP $^{-/-}$ cells, due to the existence of large quantity of free 14-3-3, nuclear NFAT increases from 0.5 nM to a less higher level (5.6 nM) than in MCIP $^{+/+}$ cells (7.2 nM) as shown in Fig. 4.2b.

By comparison of the experimental and simulated hypertrophic response to different stimuli shown in Fig. 4.2a and Fig. 4.2b, we can see both two second bars are lower than the corresponding first bars, which means that our model does reproduce the seemingly facilitating function of MCIP on hypertrophic response under the stimuli of PO. Moreover, The two fourth bars are higher than the corresponding third bars which means

that our model does reproduce the inhibitory function of MCIP on hypertrophic response under the stimuli of CaN^* overexpression.

Finally there is still an issue worth discussion. In the current model, we assume that CaN^* overexpression causes the simultaneous increase of cytosolic calcium concentration and the increase of cytosolic active calcineurin concentration. In the real case, there will be some time difference (typically several minutes) between these two events. After including a time delay into our model accounting for this time difference, further investigations show that although the simulated dynamics (especially the short term dynamics of $CaNc^*(t)$) shows some difference, the steady state value of simulated nuclear NFAT concentration remains the same. Similar is the case for the simulations for PO stimulus.

To summarize, we have built a computational model for the complex calcium-calcineurin-MCIP-NFAT signaling network in cardiac myocytes. Our model can correctly predict the mutant ($MCIP^{-/-}$) behavior under different stress such as PO and CaN^* overexpression (compare Fig. 4.2b with Fig. 4.2a). Our simulation results suggest that in the case of PO, the seemingly facilitating role of MCIP is due to activated BMK1 that promotes the conversion of MCIP to $MCIP^P$ and then to $MCIP^{PP}$ which associates with 14-3-3 to relieve the inhibitory effect of 14-3-3 on hypertrophic response. In the case of CaN^* TG mice, the overexpressed CaN^* causes the dissociation of Complex2 by promoting the conversion of $MCIP^{PP}$ to $MCIP^P$ then to MCIP, which associates with CaN^* to inhibit its activity. Moreover, the feedback loop of MCIP expression controlled by NFAT contributes significantly to this inhibition.

In this chapter and previous two chapters, we presented several mathematical models for calcium homeostasis and signaling systems in yeast cells and mammalian cardiac myocytes. As mentioned in Section 1.3.4.7, similar as Ca^{2+}, Zn^{2+} also functions as an important signaling molecule in various organisms. In Chapter 5, we will present a mathematical model developed for simulating the *in vitro* transcriptional response of zinc homeostasis in *E. coli*.

Chapter 5 Simulating *In Vitro* Transcriptional Response of Zinc Homeostasis System in *E. coli*[16]

5.1 Introduction

Zinc is essential for life. It serves as a structural or catalytic cofactor in a large number of proteins such as RNA polymerase and zinc finger proteins [42,66,77,92,149,155,168,172,182]. Zinc also plays an important signalling role in various biological processes such as neurotransmission, cell proliferation, and apoptosis (see Section 1.3.4.7) [43,219]. However, due to the potential toxicity of zinc, intracellular zinc concentrations must be kept under tight control. For example, a high intracellular Zn^{2+} concentration can inhibit the aerobic respiratory chain in *E. coli* [155,168,172].

E. coli achieves zinc homeostasis by regulating the uptake and efflux of zinc across the plasma membrane [42,172]. As we can see in Fig. 5.1a, extracellular zinc ions are transported into the cytoplasm through ZnuABC (an ABC-type transporter) and ZupT (a zinc permease), while the efflux of zinc is accomplished by ZntA (a P-type ATPase) and ZitB (a cation diffusion facilitator) [12,18,33,41,42,85-87,167,168,172,176]. Within the cytoplasm, similar to copper, it is thought that zinc trafficking may involve chaperone-like proteins [163,202]. However, despite considerable experimental effort [64,125,198,237], the zinc chaperone protein in *E. coli* has yet to be identified [66,155]. The ZnuABC transporter (encoded by the *znuACB* gene cluster) is composed of the periplasmic binding protein ZnuA, the ATPase ZnuC, and the integral membrane protein ZnuB [240]. This zinc uptake system is regulated by Zur, a dimer protein which binds at least 2 zinc ions. Zur is sensitive to the intracellular zinc concentration, and zinc-bound Zur (presumably the Zn_4Zur form, the Zur dimer which contains 2 zinc ions per monomer and it is denoted as Zn_2Zur in [163]) can compete with RNA polymerase to bind to the *znu* operator and act as a repressor [167,168,172].

[16] This Chapter is based on: Jiangjun Cui, Jaap Kaandorp and Catherine M. Lloyd, Simulating *in vitro* transcriptional response of Zn^{2+} homeostasis system in *Escherichia coli*, *BMC Systems Biology* 2:89, (2008).

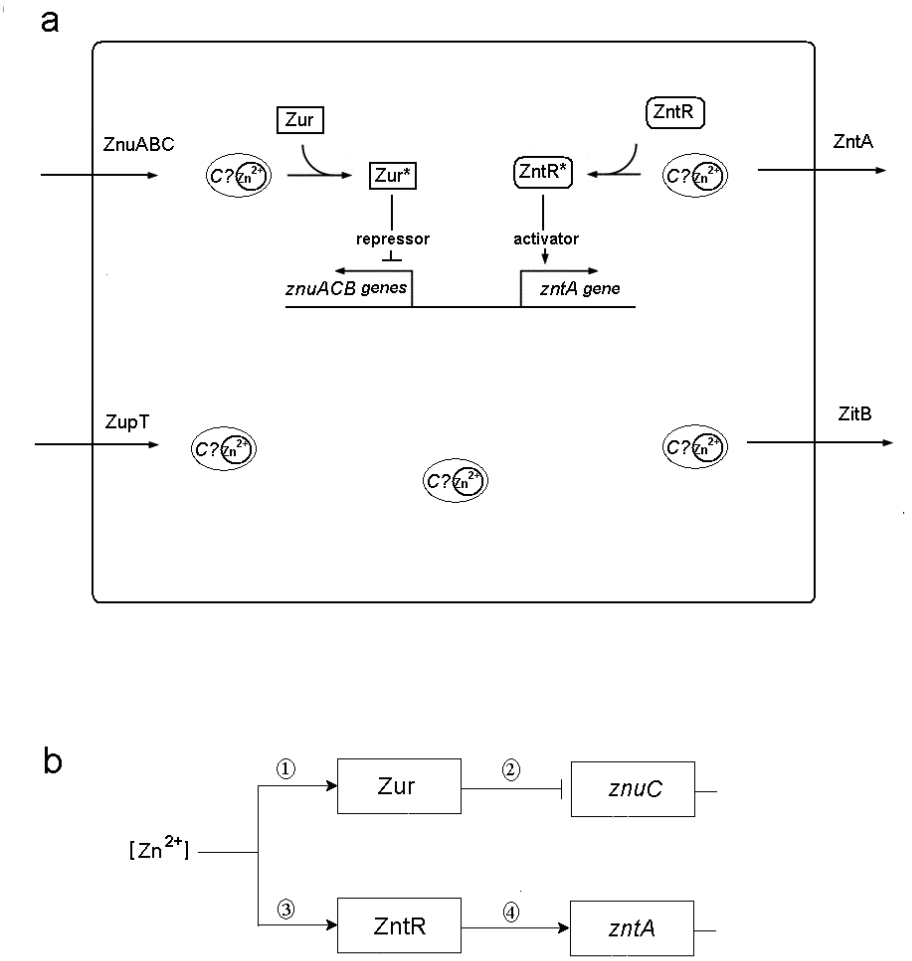

Figure 5.1 Schematic Representations of *E. coli* Zinc Homeostasis System and the *in vitro* Sub-processes.

(a) A schematic graph depicts the Zn^{2+} homeostasis system in *Escherichia coli.* Extracellular Zn^{2+} enters the cytoplasm through ZnuABC and ZupT [87,168]. In the presence of zinc, Zur binds to the *znu* operator and represses the transcription of *znuACB* gene cluster [167,172]. Excess intracellular zinc ions are exported by ZntA and ZitB [41,85,176]. Intracellular zinc can bind with protein ZntR and convert it into a strong transcriptional activator of the *zntA* gene [33,164,172]. The cytoplasmic zinc trafficking may involve chaperone-like proteins [163]. Abbreviations used in this graph are as follows: Zur^* (active Zur); $ZntR^*$ (active ZntR); C? (zinc chaperone whose existence is still under debate [66,163]). (b) A schematic graph depicts the main sub-processes which we need to model for simulating *in vitro* transcriptional response: (i) Zn^{2+}-sensing by Zur, (ii) transcriptional repression of *znuC* gene by Zur, (iii) Zn^{2+}-sensing by ZntR and (iv) transcriptional activation of *zntA* gene by ZntR. (Please note that here we only model the transcription of *znuC* gene rather than of the whole *znuACB* gene cluster because we only have reported data for *znuC* transcripts available for comparison [163]).

In contrast to this mechanism, zinc efflux through ZntA is regulated by ZntR, a zinc-responsive MerR-like transcriptional regulator [33,104,164,172]. ZntR is a dimer protein which can bind one or two zinc ions per monomer depending on the buffer conditions [164]. A metal occupancy assay of ZntR, monitored by changes in tyrosine fluorescence, shows non-cooperative 1:1 binding of Zn(II) to the ZntR dimer [103]. ZntR in its apo form[17] only slightly activates *zntA* transcription [33,164,172]. The binding of zinc-bound ZntR to the promoter introduces conformational changes in the DNA, which apparently make the promoter a better substrate for RNA polymerase, thus strongly activating the transcription of the *zntA* gene and increasing the efflux of zinc from the cell [164].

During 1999-2001, Outten CE and her colleagues presented some results on *in vitro* transcription and metal-binding competition experiments of *E.coli* zinc homeostasis system and showed that both ZntR and Zur are extremely avid zinc sensors and are both saturated at femtomolar free zinc concentrations [103,163,164]. In these experiments, the Zn(II) concentration was precisely controlled by using *N*,*N*,*N*',*N*'-tetrakis(2-pyridylmethyl) ethylenediamine (TPEN) as a zinc buffer [163]. The various assays relevant to this paper include the Zur-DNA interaction assay, Zur transcription assay and two ZntR transcription assays. In the Zur-DNA interaction assay the DNase I footprinting technique was used and the Zur-DNA interaction was found to correlate with the concentration of free Zn(II) (see the black dots in Fig. 5.2). In the Zur transcription assay, *in vitro* run-off transcription experiments with Zur and the *znu* Zn(II) uptake system were conducted, and the levels of the *znuC* RNA transcript were reported to correlate with the free Zn(II) concentration (see the red dots in Fig. 5.3d) [163]. In these real run-off transcription experiments, various reactants (including *znuC* DNA template, Zur, Zn(II), RNA polymerase (RNAP) and heparin, etc.) were added sequentially and allowed to equilibrate first (~30 min total). Then nucleoside triphosphates (NTPs) were added and the reaction was stopped for 15 min (Outten CE, personal communication). Similar run-off transcription experiments (the ZntR transcription assay (I)) were conducted with ZntR and the *zntA* promoter and the levels of the *zntA* RNA transcript were reported to correlate with the free Zn(II) concentration (see the blue dots in Fig. 5.3d) [163]. Similarly in ZntR transcription assay (II), the levels of the *zntA* RNA transcript were reported to correlate with the total ZntR concentration, both with added Zn(II) and without Zn(II) (see the red and blue dots in Fig. 5.9a, respectively). Moreover, it was also reported that the levels of the *zntA* RNA transcript correlated with the total zinc concentration (see the black dots in Fig. 5.9b) [164].

Although the transcriptional regulation of the zinc homeostasis system in *E. coli* seems to be well characterized, and despite the fact that detailed *in vitro* experimental data on this system are also available [103,163,164], as yet there is no mathematical model to help interpret these data. The principal aim of this paper is to present a mathematical model which is capable of simulating this regulatory system and can be used to help interpret various experimental data.

We will present a unified mathematical model composed of 14 reactions (see the following Table 5.1) and use it to simulate the *in vitro* transcriptional response of zinc

[17] The apo form of ZntR (i.e., apo-ZntR) means that ZntR without the binding of Zn(II).

homeostasis system in *E. coli.* The construction of the model is based on biochemical principles and we use an open source software (Cellerator) to automatically generate the equations (see Section 4.2.1) [194,245]. We validate our model by comparing the simulation results with the corresponding *in vitro* experimental data.

Table 5.1: The reactions of the model.[18]

Sub-Process Name	Reaction No.	Cellerator Form of Particular Reactions	Description
Zn^{2+}-Sensing by ZntR	(1)	$\{Px + Zn \rightleftarrows Px_1, r_1, r_2\}$	apo-ZntR binding with zinc to become active ZntR
Transcriptional Activation of *zntA* Gene by ZntR	(2)	$\{Dz + Rz \rightleftarrows Qz_1, k_{2a}, k_{-2}\}$	DNA of ZntA binding with RNA polymerase
	(3)	$\{Qz_1 \rightleftarrows Dz + Mz + Rz, k_3, 0\}$	transcription of complex Qz_1
	(4)	$\{Dz + Px \rightleftarrows Qz_4, k_{1b}, k_{-1}\}$	apo-ZntR binding with DNA
	(5)	$\{Qz_4 + Rz \rightleftarrows Qz_5, k_{2b}, k_{-2}\}$	apo-ZntR-DNA complex binding with RNA polymerase
	(6)	$\{Qz_5 \rightleftarrows Qz_4 + Mz + Rz, k_3, 0\}$	transcription of complex Qz_5
	(7)	$\{Dz + Px_1 \rightleftarrows Qz_2, k_1, k_{-1}\}$	active ZntR binding with DNA

[18] Abbreviations and synonyms used in this table are as follows: Zn (free zinc ion); Px (apo-ZntR); Px_1 (active ZntR, i.e., ZnZntR); Py (the Zur dimer which contains two zinc ions per dimer, here we denote it as Zn_2Zur and it is denoted as Zn_1Zur in [26]); Py_1 (active Zur, i.e., the Zur dimer which contains four zinc ions per dimer, here we denote it as Zn_4Zur and it is denoted as Zn_2Zur in [26]); z (ZntA); Dz (DNA of ZntA); Rz (RNA polymerase for zntA transcription); Mz (mRNA of ZntA); Qz_1 (transcription initiation complex formed by Dz and Rz); Qz_2 (ZnZntR-DNA complex); Qz_3 (transcription initiation complex formed by Qz_2 and Rz); Qz_4 (apo-ZntR-DNA complex); Qz_5 (transcription initiation complex formed by Qz_4 and Rz); w (ZnuC); Dw (DNA of ZnuC); Rw (RNA polymerase for *znuC* transcription); Mw (mRNA of ZnuC); Qw_1 (transcription initiation complex of ZnuC); Qw_2 (Zn_4Zur-DNA complex which can not further bind with Rw); Tp (free TPEN not bounded by zinc); Tp_1 (zinc-bound TPEN).

	(8)	$\{Qz_2 + Rz \rightleftarrows Qz_3, k_{2c}, k_{-2}\}$	ZnZntR-DNA complex binding with RNA polymerase
	(9)	$\{Qz_3 \rightleftarrows Qz_2 + Mz + Rz, k_3, 0\}$	transcription of complex Qz_3
Zn^{2+}-Sensing by Zur	(10)	$\{Zn^2 + Py \rightleftarrows Py_1, r_3, r_4\}$	Zn_2Zur binding with zinc to become active Zur (i.e., Zn_4Zur)
Transcriptional Repression of *znuC* Gene by Zur	(11)	$\{Dw + Py_1 \rightleftarrows Qw_2, k_{1a}, k_{-1}\}$	active Zur binding with DNA to form complex Qw_2 which can not bind with RNA polymerase
	(12)	$\{Dw + Rw \rightleftarrows Qw_1, k_2, k_{-2}\}$	DNA of ZnuC binding with RNA polymerase
	(13)	$\{Qw_1 \rightleftarrows Dw + Mw + Rw, k_3, 0\}$	transcription of complex Qw_1
Zn^{2+}-Binding by TPEN	(14)	$\{Zn + Tp \rightleftarrows Tp_1, r_5, r_6\}$	TPEN binding with zinc to form a complex

5.2 Methods

5.2.1 Representation of Relevant Reactions

As we can see in Fig. 5.1b, in order to simulate the *in vitro* transcriptional response, we need to model the four involved sub-processes in addition to the process of zinc buffering by TPEN, namely: (i) Zn^{2+}-sensing by Zur, (ii) transcriptional repression of the *znuC* gene by Zur, (iii) Zn^{2+}-sensing by ZntR and (iv) transcriptional activation of the *zntA* gene by ZntR.

1) Zn^{2+}-Sensing by ZntR

ZntR is a dimer protein which can bind one or two zinc ions per dimer depending on the buffer conditions [164,172]. However, metal occupancy assay of ZntR monitored by changes in tyrosine fluorescence shows non-cooperative 1:1 binding of Zn(II) to the ZntR dimer [103]. The zinc-bound form of ZntR has been reported to contain 0.75 ± 0.075 zinc/monomer [172], neither favoring 1:1 binding nor 1:2 binding. However, this result was obtained under the condition of excessive ZntR protein (5μM) [172]. Since the free zinc concentration and total ZntR concentration are both extremely low (in sub-nM and nM range, respectively) in all the relevant real assays (except the ZntR transcription assay (II) related to Fig. 5.9a) of this paper [163,164], here we assume that the active form of ZntR is ZnZntR (i.e. there is a 1:1 binding). We use Reaction (1) (see Table 5.1) to describe this sub-process.

2) Transcriptional Activation of zntA Gene by ZntR

Experimental results have shown that there is constitutive transcription activity of the *zntA* promoter [33]. According to Hayot *et al.*[19], this constitutive transcription can be described by Reactions (2-3) (see Table 1) [96].

In the absence of Zn(II), apo-ZntR binds to the promoter and distorts the DNA which appears to result in an approximately fourfold induction [33]. According to Hayot *et al.* [96], this apo-ZntR activated transcription can be described by Reactions (4-6) (see Table 5.1) and we have the relation: $k_{2b} = 4 * k_{2a}$.

The binding of Zn(II) to ZntR converts it into a transcriptional activator protein that introduces conformational changes in the DNA which apparently make the promoter a better substrate for RNA polymerase [164]. According to Hayot *et al.* [96], this ZnZntR activated transcription can be described by Reactions (7-9) (see Table 5.1).

3) Zn^{2+}-Sensing By Zur

Zur is a dimer protein which binds at least 2 zinc ions [163,167]. Experimental results have established that the DNA binding of Zur presumably involves the Zn_4Zur form (i.e., the Zur dimer which contains 2 zinc ions per monomer and it is denoted as Zn_2Zur in [163]) rather than the Zn_2Zur form (the Zur dimer which contains one zinc ion per monomer and it is denoted as Zn_1Zur in [163]). Similar as Eq. 2.1 for modeling the binding of calmodulin with calcium ions [163], we use Reaction (10) (see Table 5.1) to describe this sub-process under the assumption of strong cooperativity existing between the two active sites of Zn_2Zur (please note that the purified Zur dimer which contains one zinc ion per monomer is used in the relevant assays [163]).

---

[19] Please note that the justification for the specific parameter values used in Hayot's model can be found in [36]. Hayot's model is later used by Ingram *et al.* to study the dynamics of the bi-fan motif [109].

4) Transcriptional Repression of znuC Gene by Zur

The genes *znuA* and *znuCB* are transcribed divergently and both promoters of *znuA* and *znuCB* are active *in vivo* [163,168]. Since we only have reported data for *znuC* transcripts available for comparison [163], here we choose to model the transcription of the *znuC* gene only. In the absence of Zn(II), Zur does not compete for DNA binding. The addition of excessive Zn(II) allows Zur to bind to the *znuC* promoter and prevents its binding with RNA polymerase [163]. According to Hayot *et al.* [96], we can use Reactions (11-13) (see Table 5.1) to describe this process.

5) Zinc Binding by TPEN

As mentioned before, TPEN is used as a zinc buffer to precisely control the free zinc concentration in the relevant assays [163,164] and this process can be apparently described by Reaction 14 (see Table 5.1) [163]. Normally the free zinc concentration (i.e., parameter Zn) is regarded as a constant and it can be simply calculated from the total zinc concentration (i.e., parameter Zn_{tot}) according to the following buffer equation:

$$Zn * (TPEN_{tot} - (Zn_{tot} - Zn)) / (Zn_{tot} - Zn) = 1 / K'_{Zn-TPEN}$$

However, in more complicated cases such as the ZntR transcription assay (II), it is wiser to perform numerical simulations by including this reaction and the free zinc concentration is no longer regarded as a constant.

5.2.2 The Equations of the Model and the Numerical Solver

The detailed equations used for simulating different assays are shown as below. We use Mathematica's differential equation solver "NDSolve" to solve the relevant ODEs. If the studied ODEs are stiff as is the case for the relevant simulations of Fig. 5.9, we set the method option of NDSolve to be "StiffnessSwitching".

5.2.2.1 Equations for Zur-DNA Interaction

$$\frac{dPy(t)}{dt} = -r_3 Zn^2 Py(t) + r_4 Py_1(t)$$

$$\frac{dPy_1(t)}{dt} = r_3 Zn^2 Py(t) - r_4 Py_1(t) - k_{1a} Dw(t) Py_1(t) + k_{-1} Qw_2(t)$$

$$\frac{dDw(t)}{dt} = -k_{1a} Dw(t) Py_1(t) + k_{-1} Qw_2(t)$$

$$\frac{dQw_2(t)}{dt} = k_{1a} Dw(t) Py_1(t) - k_{-1} Qw_2(t)$$

By imposing all the derivatives to be 0, we get four steady state equations which contain only two independent equations. Therefore, in order to derive the steady state values, two conservation constraints need to be included:

$$Py(t) + Py_1(t) + Qw_2(t) = Py_{tot} = 25nM, Dw(t) + Qw_2(t) = D_0 = 1nM$$

By solving the two independent steady state equations with the above conservation constraints, we can get the steady state concentration value of Zn_4Zur-DNA complex (i.e., Qw_2^s) as a function of parameter Zn as follows:

$$\begin{aligned} Qw_2^s &= f(Zn) \\ &= Py_{tot} + \frac{Zn^2 D_0 k_{1a} r_3 + Zn^2 k_{-1} r_3 - Zn^2 Py_{tot} k_{1a} r_3 + D_0 k_{1a} r_4 + 2k_{-1} r_4 - Py_{tot} k_{1a} r_4}{2(Zn^2 k_{1a} r_3 + k_{1a} r_4)} \\ &- \frac{\sqrt{4Zn^2 k_{-1} k_{1a} r_3 Py_{tot} (Zn^2 r_3 + r_4) + (Zn^2 D_0 k_{1a} r_3 + Zn^2 k_{-1} r_3 - Zn^2 Py_{tot} k_{1a} r_3 + k_{-1} r_4)^2}}{2(Zn^2 k_{1a} r_3 + k_{1a} r_4)} \\ &+ \frac{k_{-1} r_4^{\,2} - r_4 \sqrt{4Zn^2 k_{-1} k_{1a} r_3 Py_{tot} (Zn^2 r_3 + r_4) + (Zn^2 D_0 k_{1a} r_3 + Zn^2 k_{-1} r_3 - Zn^2 Py_{tot} k_{1a} r_3 + k_{-1} r_4)^2}}{2Zn^2 r_3 (Zn^2 k_{1a} r_3 + k_{1a} r_4)} \end{aligned}$$

5.2.2.2 Equations for Zur Transcription Assay

(1) Equations for preliminary equilibrium of reactants before NTPs were added

$$\frac{dPy(t)}{dt} = -r_3 Zn^2 Py(t) + r_4 Py_1(t)$$

$$\frac{dPy_1(t)}{dt} = r_3 Zn^2 Py(t) - r_4 Py_1(t) - k_{1a} Dw(t) Py_1(t) + k_{-1} Qw_2(t)$$

$$\frac{dDw(t)}{dt} = -k_{1a} Dw(t) Py_1(t) + k_{-1} Qw_2(t) + k_{-2} Qw_1(t) - k_2 Dw(t) Rw(t)$$

$$\frac{dRw(t)}{dt} = k_{-2} Qw_1(t) - k_2 Dw(t) Rw(t)$$

$$\frac{dQw_1(t)}{dt} = -k_{-2} Qw_1(t) + k_2 Dw(t) Rw(t)$$

$$\frac{dQw_2(t)}{dt} = k_{1a} Dw(t) Py_1(t) - k_{-1} Qw_2(t)$$

(2) Equations for Zur run-off transcription after NTPs were added

$$\frac{dPy(t)}{dt} = -r_3 Zn^2 Py(t) + r_4 Py_1(t)$$
$$\frac{dPy_1(t)}{dt} = r_3 Zn^2 Py(t) - r_4 Py_1(t) - k_{1a} Dw(t) Py_1(t) + k_{-1} Qw_2(t)$$
$$\frac{dDw(t)}{dt} = -k_{1a} Dw(t) Py_1(t) + k_{-1} Qw_2(t) + k_3 Qw_1(t) + k_{-2} Qw_1(t) - k_2 Dw(t) Rw(t)$$
$$\frac{dRw(t)}{dt} = k_3 Qw_1(t) + k_{-2} Qw_1(t) - k_2 Dw(t) Rw(t)$$
$$\frac{dQw_1(t)}{dt} = -k_3 Qw_1(t) - k_{-2} Qw_1(t) + k_2 Dw(t) Rw(t)$$
$$\frac{dQw_2(t)}{dt} = k_{1a} Dw(t) Py_1(t) - k_{-1} Qw_2(t)$$
$$\frac{dMw(t)}{dt} = k_3 Qw_1(t)$$

5.2.2.3 Equations for ZntR Transcription Assay (I)

(1) Equations for preliminary equilibrium of reactants before NTPs were added

$$\frac{dPx(t)}{dt} = -r_1 ZnPx(t) + r_2 Px_1(t) - k_{1b} Dz(t) Px(t) + k_{-1} Qz_4(t)$$
$$\frac{dPx_1(t)}{dt} = r_1 ZnPx(t) - r_2 Px_1(t) - k_1 Dz(t) Px_1(t) + k_{-1} Qz_2(t)$$
$$\frac{dDz(t)}{dt} = -k_{1b} Dz(t) Px(t) - k_1 Dz(t) Px_1(t) + k_{-1} Qz_2(t) + k_{-2} Qz_1(t) + k_{-1} Qz_4(t) - k_{2a} Dz(t) Rz(t)$$
$$\frac{dRz(t)}{dt} = k_{-2} Qz_1(t) + k_{-2} Qz_3(t) + k_{-2} Qz_5(t) - k_{2a} Dz(t) Rz(t) - k_{2b} Qz_4(t) Rz(t) - k_{2c} Qz_2(t) Rz(t)$$
$$\frac{dQz_1(t)}{dt} = -k_{-2} Qz_1(t) + k_{2a} Dz(t) Rz(t)$$
$$\frac{dQz_2(t)}{dt} = k_1 Dz(t) Px_1(t) - k_{-1} Qz_2(t) + k_{-2} Qz_3(t) - k_{2c} Qz_2(t) Rz(t)$$
$$\frac{dQz_3(t)}{dt} = -k_{-2} Qz_3(t) + k_{2c} Qz_2(t) Rz(t)$$
$$\frac{dQz_4(t)}{dt} = k_{1b} Dz(t) Px(t) - k_{-1} Qz_4(t) + k_{-2} Qz_5(t) - k_{2b} Qz_4(t) Rz(t)$$
$$\frac{dQz_5(t)}{dt} = -k_{-2} Qz_5(t) + k_{2b} Qz_4(t) Rz(t)$$

(2) Equations for ZntR run-off transcription (I) after NTPs were added

$$\frac{dPx(t)}{dt} = -r_1 ZnPx(t) + r_2 Px_1(t) - k_{1b} Dz(t) Px(t) + k_{-1} Qz_4(t)$$

$$\frac{dPx_1(t)}{dt} = r_1 ZnPx(t) - r_2 Px_1(t) - k_1 Dz(t) Px_1(t) + k_{-1} Qz_2(t)$$

$$\frac{dDz(t)}{dt} = -k_{1b} Dz(t) Px(t) - k_1 Dz(t) Px_1(t) + k_{-1} Qz_2(t) + k_3 Qz_1(t)$$

$$+ k_{-2} Qz_1(t) + k_{-1} Qz_4(t) - k_{2a} Dz(t) Rz(t)$$

$$\frac{dRz(t)}{dt} = k_3 Qz_1(t) + k_{-2} Qz_1(t) + k_3 Qz_3(t) + k_{-2} Qz_3(t) + k_3 Qz_5(t) + k_{-2} Qz_5(t)$$

$$- k_{2a} Dz(t) Rz(t) - k_{2b} Qz_4(t) Rz(t) - k_{2c} Qz_2(t) Rz(t)$$

$$\frac{dQz_1(t)}{dt} = -k_3 Qz_1(t) - k_{-2} Qz_1(t) + k_{2a} Dz(t) Rz(t)$$

$$\frac{dQz_2(t)}{dt} = k_1 Dz(t) Px_1(t) - k_{-1} Qz_2(t) + k_3 Qz_3(t) + k_{-2} Qz_3(t) - k_{2c} Qz_2(t) Rz(t)$$

$$\frac{dQz_3(t)}{dt} = -k_3 Qz_3(t) - k_{-2} Qz_3(t) + k_{2c} Qz_2(t) Rz(t)$$

$$\frac{dQz_4(t)}{dt} = k_{1b} Dz(t) Px(t) - k_{-1} Qz_4(t) + k_3 Qz_5(t) + k_{-2} Qz_5(t) - k_{2b} Qz_4(t) Rz(t)$$

$$\frac{dQz_5(t)}{dt} = -k_3 Qz_5(t) - k_{-2} Qz_5(t) + k_{2b} Qz_4(t) Rz(t)$$

$$\frac{dMz(t)}{dt} = k_3 Qz_1(t) + k_3 Qz_3(t) + k_3 Qz_5(t)$$

5.2.2.4 Equations for ZntR Transcription Assay (II) - Including TPEN Reaction

(1) Equations for preliminary equilibrium of reactants before NTPs were added

$$\frac{dPx(t)}{dt} = -r_1 Zn(t)Px(t) + r_2 Px_1(t) - k_{1b} Dz(t)Px(t) + k_{-1} Qz_4(t)$$

$$\frac{dPx_1(t)}{dt} = r_1 Zn(t)Px(t) - r_2 Px_1(t) - k_1 Dz(t)Px_1(t) + k_{-1} Qz_2(t)$$

$$\frac{dTp(t)}{dt} = -r_5 Zn(t)Tp(t) + r_6 Tp_1(t)$$

$$\frac{dTp_1(t)}{dt} = r_5 Zn(t)Tp(t) - r_6 Tp_1(t)$$

$$\frac{dZn(t)}{dt} = -r_1 Zn(t)Px(t) + r_2 Px_1(t) - r_5 Zn(t)Tp(t) + r_6 Tp_1(t)$$

$$\frac{dDz(t)}{dt} = -k_{1b} Dz(t)Px(t) - k_1 Dz(t)Px_1(t) + k_{-1} Qz_2(t) + k_{-2} Qz_1(t) + k_{-1} Qz_4(t) - k_{2a} Dz(t)Rz(t)$$

$$\frac{dRz(t)}{dt} = k_{-2} Qz_1(t) + k_{-2} Qz_3(t) + k_{-2} Qz_5(t) - k_{2a} Dz(t)Rz(t) - k_{2b} Qz_4(t)Rz(t) - k_{2c} Qz_2(t)Rz(t)$$

$$\frac{dQz_1(t)}{dt} = -k_{-2} Qz_1(t) + k_{2a} Dz(t)Rz(t)$$

$$\frac{dQz_2(t)}{dt} = k_1 Dz(t)Px_1(t) - k_{-1} Qz_2(t) + k_{-2} Qz_3(t) - k_{2c} Qz_2(t)Rz(t)$$

$$\frac{dQz_3(t)}{dt} = -k_{-2} Qz_3(t) + k_{2c} Qz_2(t)Rz(t)$$

$$\frac{dQz_4(t)}{dt} = k_{1b} Dz(t)Px(t) - k_{-1} Qz_4(t) + k_{-2} Qz_5(t) - k_{2b} Qz_4(t)Rz(t)$$

$$\frac{dQz_5(t)}{dt} = -k_{-2} Qz_5(t) + k_{2b} Qz_4(t)Rz(t)$$

(2) Equations for ZntR run-off transcription (II) after NTPs were added

$$\frac{dPx(t)}{dt} = -r_1 Zn(t)Px(t) + r_2 Px_1(t) - k_{1b} Dz(t)Px(t) + k_{-1} Qz_4(t)$$

$$\frac{dPx_1(t)}{dt} = r_1 Zn(t)Px(t) - r_2 Px_1(t) - k_1 Dz(t)Px_1(t) + k_{-1} Qz_2(t)$$

$$\frac{dTp(t)}{dt} = -r_5 Zn(t)Tp(t) + r_6 Tp_1(t)$$

$$\frac{dTp_1(t)}{dt} = r_5 Zn(t)Tp(t) - r_6 Tp_1(t)$$

$$\frac{dZn(t)}{dt} = -r_1 Zn(t)Px(t) + r_2 Px_1(t) - r_5 Zn(t)Tp(t) + r_6 Tp_1(t)$$

$$\frac{dDz(t)}{dt} = -k_{1b} Dz(t)Px(t) - k_1 Dz(t)Px_1(t) + k_{-1} Qz_2(t) + k_3 Qz_1(t)$$
$$+ k_{-2} Qz_1(t) + k_{-1} Qz_4(t) - k_{2a} Dz(t)Rz(t)$$

$$\frac{dRz(t)}{dt} = k_3 Qz_1(t) + k_{-2} Qz_1(t) + k_3 Qz_3(t) + k_{-2} Qz_3(t) + k_3 Qz_5(t) + k_{-2} Qz_5(t)$$
$$- k_{2a} Dz(t)Rz(t) - k_{2b} Qz_4(t)Rz(t) - k_{2c} Qz_2(t)Rz(t)$$

$$\frac{dQz_1(t)}{dt} = -k_3 Qz_1(t) - k_{-2} Qz_1(t) + k_{2a} Dz(t)Rz(t)$$

$$\frac{dQz_2(t)}{dt} = k_1 Dz(t)Px_1(t) - k_{-1} Qz_2(t) + k_3 Qz_3(t) + k_{-2} Qz_3(t) - k_{2c} Qz_2(t)Rz(t)$$

$$\frac{dQz_3(t)}{dt} = -k_3 Qz_3(t) - k_{-2} Qz_3(t) + k_{2c} Qz_2(t)Rz(t)$$

$$\frac{dQz_4(t)}{dt} = k_{1b} Dz(t)Px(t) - k_{-1} Qz_4(t) + k_3 Qz_5(t) + k_{-2} Qz_5(t) - k_{2b} Qz_4(t)Rz(t)$$

$$\frac{dQz_5(t)}{dt} = -k_3 Qz_5(t) - k_{-2} Qz_5(t) + k_{2b} Qz_4(t)Rz(t)$$

$$\frac{dMz(t)}{dt} = k_3 Qz_1(t) + k_3 Qz_3(t) + k_3 Qz_5(t)$$

5.2.3 Translating the Model into CellML

CellML is an XML-based modelling language which provides an unambiguous method of defining models of biological processes [131,254]. The model described above has been translated into two CellML versions [255,256]: the first version (please visit the webpage [255] for downloading the detailed code) is for ZntR transcription assay (I) which excludes the buffering equation of TPEN (i.e., Reaction 14); the second version (please visit the webpage [256] for downloading the detailed code) is for ZntR transcription assay (II) which includes the buffering reaction of TPEN.

5.2.4 The Image Analysis Method

The original figures are imported into the Paint tool of Windows system. The pixel coordinates are recorded for the axis origin, two tick points (one tick point on the horizontal axis and one tick point on the vertical axis) and all experimental data points. Then by simple algebraic calculations we can get the real coordinate values of the reported data points. For example, imagine that we need to analyze an image with x coordinate (in logarithm) and normal y coordinate. Assume the measured pixel coordinates of the axis origin (its real coordinate values are $\{10^a, b\}$) and tick points (their real coordinate values are $\{10^a, c\}$ and $\{10^d, b\}$) are (p_{x0}, p_{y0}), (p_{x0}, p_{y1}), (p_{x1}, p_{y0}), respectively. For a data point with measured pixel coordinates (p_{x2}, p_{y2}), we can calculate its real coordinate values {f, g} as follows:

$$f = 10^{(d-a)*(p_{x2}-p_{x0})/(p_{x1}-p_{x0})}$$
$$g = (c-b)*(p_{y2}-p_{y0})/(p_{y1}-p_{y0})$$

The relative error of such data reconstruction is estimated to be (0.5-3)% depending on the image size.

5.3 Results

As shown in Table 5.1, we use 14 reactions to represent the involved sub-processes. Here we present our simulation results for simulating various *in vitro* assays including Zur-DNA interaction assay, Zur transcription assay and two ZntR transcription assays[20] .

5.3.1 Zur-DNA Interaction

The Zur-DNA interaction assay [163] involves only two reactions (Reactions 10 and 11, see Table 5.1), which are expressed as 4 ODEs (for the detailed equations, see Section 5.2.2.1). By imposing the conservation constraints $(Py(t) + Py_1(t) + Qw_2(t) = Py_{tot} = 25nM, Dw(t) + Qw_2(t) = D_0 = 1nM)$ (as in the real experiment [163]) and solving the relevant steady state equations (for the parameters, please see Table 5.2)[21], we can depict the simulated ratio of steady state concentrations of the Zn_4Zur-DNA complex (denoted by Qw_2^s) and the total concentration of *znuC* DNA

[20] Please note that the main differences between ZntR transcription assay (I) and assay (II) are the differences in the initial conditions and in that in assay (II), we take consideration of the competition between ZntR and TPEN for zinc binding by including Reaction 14 whereas in assay (I), Reaction 14 is not included.

[21] Note that in the real experiment the total concentration of Zur monomer is 50 nM, here we need to divide this value by half which means that $Py_{tot} = 25nM$ because in solution, Zur exists in dimer form [168] and in similar way we can calculate Px_{tot}.

($D_0 = 1nM$ in this case) as a function of the logarithm of parameter Zn as shown in Fig. 5.2 (the black curve). From this figure, we can see that when the simulated free zinc concentration (Zn) ranges from 10^{-18} M to 10^{-14} M, the simulated protection ratio (denoted by Qw_2^s / D_0 *100%) rises from 0.00014% to 96.4% . This means that in the presence of higher free zinc concentrations, more Zn_2Zur molecules become active and bind with *znuC* DNA molecules to protect them from the binding of RNA polymerase. The simulated sigmoidal curve (the black curve in Fig. 5.2) seems to fit well with the corresponding experimental data (the black dots in Fig. 5.2) [163].

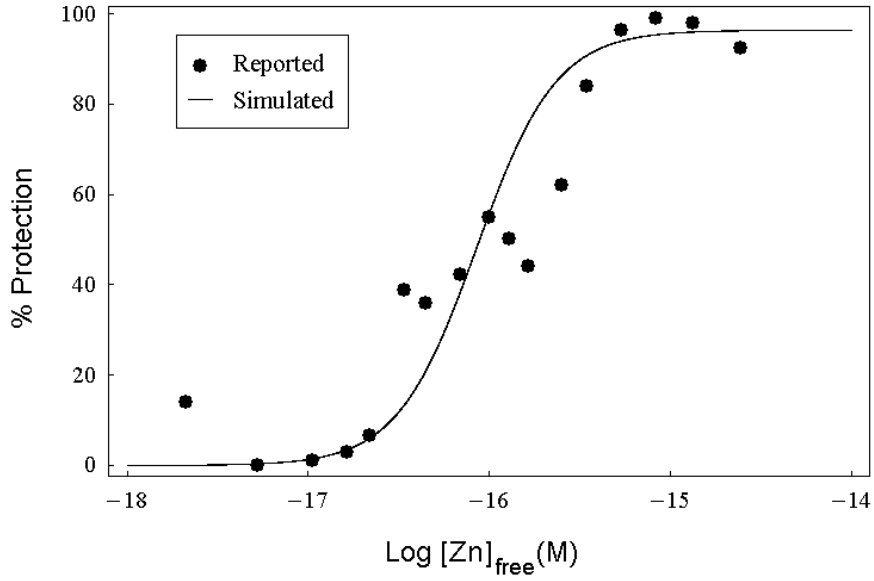

Figure 5.2. Simulation of Zur-DNA Interaction.

The black dots are reconstructed from the reported data in the original figure (the right graph in Fig. 3 in Ref. 163) using image analysis. The black curve is the simulated ratio (i.e., Qw_2^s / D_0 *100%) of the final steady state concentration values of Zn_4Zur-DNA complex (denoted by Qw_2^s) and the total concentration of DNA (i.e., $D_0 = 1nM$ in this case) as a function of the logarithm of parameter Zn which denotes the simulated free zinc concentration.

Table 5.2: Model parameters for which all results are calculated unless otherwise stated.[22]

Parameter	Value	Description
k_d	$10^{-14.9}$ M	the Zn(II) dissociation constant for ZnZntR when pH=8.0 [103]
k_{d1}	$10^{-15.2}$ M	the Zn(II) dissociation constant for the ZnZntR-DNA complex when pH=8.0 [103]
$K'_{Zn-TPEN}$	$1.99*10^{15}$ M^{-1}	the apparent association constant for Zn-TPEN at pH=8.0, 0.1M ionic strength (calculated from [163])
k_1	0.025 $(nM)^{-1}s^{-1}$	the forward rate parameter of Reaction (7)
k_{1a}	1 $(nM)^{-1}s^{-1}$	the forward rate parameter of Reaction (11)
k_{1b}	$1.253*10^{-2}$ $(nM)^{-1}s^{-1}$	the forward rate parameter of Reaction (4)
k_{-1}	0.9 s^{-1}	the backward rate parameter of Reactions (4,7,11)
k_2	0.02 $(nM)^{-1}s^{-1}$	the forward rate parameter of Reaction (12)
k_{2a}	0.00005 $(nM)^{-1}s^{-1}$	the forward rate parameter of Reaction (2)
k_{2b}	0.0002 $(nM)^{-1}s^{-1}$	the forward rate parameter of Reaction (5)
k_{2c}	0.0037 $(nM)^{-1}s^{-1}$	the forward rate parameter of Reaction (8)
k_{-2}	0.3 s^{-1}	the backward rate constant of Reactions (2,5,8,12)
k_3	0.011 s^{-1}	the transcription rate parameter

[22] Please note that $k_{2b} = 4 * k_{2a}$. Moreover, according the equilibrium theory of chemical reactions, $r_2 = k_d r_1$, $r_6 = r_5 / K'_{Zn-TPEN}$ and $k_{1b} = k_1 k_d / k_{d1}$. The values of four parameters (k_1, k_{-1}, k_2, k_{-2}) are taken from Hayot's model [96]. These parameters origin from measured rate constants of the λ repressor gene cI in *E. coli* [36,96] and are also quoted as physiologically reasonable values by Ingram *et al.* [109]. $K'_{Zn-TPEN}$ is calculated in the same way as shown in [163] (please note the pH value difference).

r_1	$2.73*10^2$ $(nM)^{-1}s^{-1}$	the forward rate parameter of Reaction (1)
r_2	$3.437*10^{-4}$ s^{-1}	the backward rate parameter of Reaction (1)
r_3	$4.41*10^{10}$ $(nM)^{-2}s^{-1}$	the forward rate parameter of Reaction (10)
r_4	$9*10^{-3}$ s^{-1}	the backward rate parameter of Reaction (10)
r_5	$3*10^4$ $(nM)^{-1}s^{-1}$	the forward rate parameter of Reaction (14)
r_6	$1.506*10^{-2}$ s^{-1}	the backward rate parameter of Reaction (14)
t_{d0}	30 min	the time duration for preliminary equilibrium of reactants before NTPs (i.e., nucleoside triphosphates) were added in run-off transcription experiments [158,163,164]
t_d	15 min	the time duration for run-off transcription after NTPs were added in transcription experiments [158,163,164]
t_{d1}	30 min	the time duration for Zur-DNA interaction assay [163]
Px_{tot}	25 nM	the total concentration of ZntR dimer which is half of the concentration of ZntR monomer denoted as $[ZntR]_{total}$ [163]
Py_{tot}	25 nM	the total concentration of Zur dimer [163]
R_0	50 nM	the total concentration of RNA polymerase [163]
D_0	4 nM	the total concentration of DNA [163]
Zn_{tot}	Vary in different assays	the total concentration of Zn(II), also denoted as $[Zn]_{total}$
$TPEN_{tot}$	Vary in different assays	the total concentration of TPEN

We derive the same simulation results by directly solving the 4 relevant ODEs with $Py(0) = Py_{tot} = 25nM, Dw(0) = D_0 = 1nM, Dw_2(0) = 0, Py_1(0) = 0$ as the initial conditions and depicting the simulated ratio of the final concentration of the Zn_4Zur-DNA complex ($Qw_2(t = t_{d1})$) and D_0. This is because the system reaches equilibrium before $t = t_{d1} = 30\,\text{min}$.

5.3.2 Zur Transcription Assay

As mentioned in the legend of Fig. 5.1b, here we only simulate the transcription of the *znuC* gene. We approximate the *in vitro* Zur run-off transcription assay by a two-phase (namely, the preliminary equilibrium phase and the transcription phase) sub-model. In the first phase, the preliminary equilibrating process of reactants involves 3 reactions (Reactions 10-12) which are expressed as 6 ODEs (see Section 5.2.2.2). In the second phase, the run-off transcription involves 4 reactions (Reactions 10-13 because now the real transcription happens after the addition of the NTPs) which are expressed as 7 ODEs (see Section 5.2.2.2).

By setting the initial conditions of the model simulation to be the same as those in the real experiment ($Py(0) = Py_{tot} = 25nM, Dw(0) = D_0 = 4nM, Rw(0) = R_0 = 50nM$ and all the remaining initial concentrations are set to be 0) and numerically solving the 6 equations for the first phase and then solving the 7 ODEs for the second phase (obviously we need to use the end concentration values of the reactants in the first phase as the initial concentration values of reactants in the second phase), we can depict the relevant transient curves for $Zn = 10^{-5}\,nM$ as shown in Fig. 5.3a-c (for the values of the remaining parameters, please see Table 5.2).

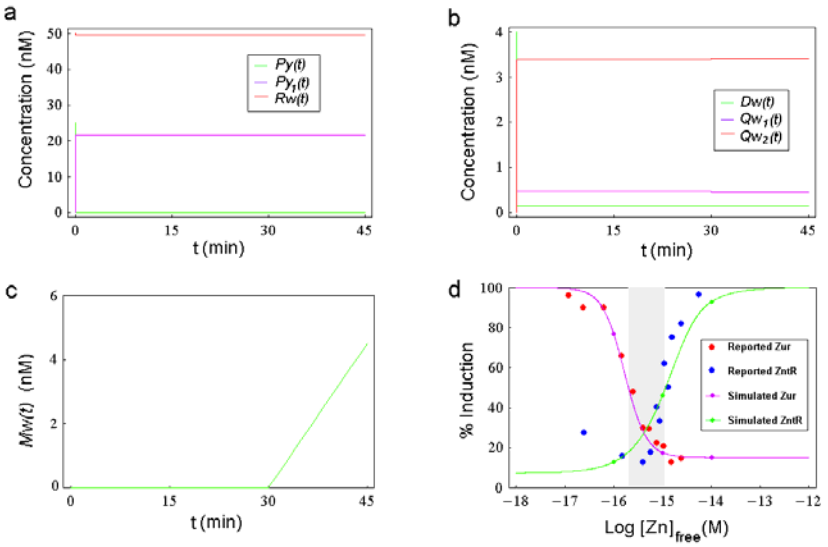

Figure 5.3. Transient Curves of Simulated Zur Transcription Assay for $Zn = 10^{-5}\,nM$ and Data Comparison (I).

(a) The green, purple and red curves denote the simulated transient curves of Zn_2Zur (Py), Zn_4Zur (Py_1), RNA polymerase (Rw) concentrations as a function of t, respectively. (b) The green, purple and red curves denote the simulated transient curves of free *znuC* DNA (Dw), *znuC* transcription initiation

complex (Qw_1) and Zn_4Zur-DNA complex (Qw_2) concentrations as a function of t , respectively. (c) The simulated concentration of the mRNA of ZnuC (i.e., $Mw(t)$) is depicted as a function of t . (d) Data comparison for Zur and ZntR transcription assays. Big red dots for the Zur transcription assay and big blue dots for the ZntR transcription assay (I) are reconstructed from the reported data in the original figure (Fig. 4 in Ref. 163) using image analysis method (please refer to Section 5.2.4 for more details). The purple curve and the green curve are the corresponding simulated normalized final concentrations of the mRNA of ZnuC (i.e., $Mw(t = t_{d0} + t_d)$) and the mRNA of ZntA (i.e., $Mz(t = t_{d0} + t_d)$) as a function of the logarithm of parameter Zn , respectively. The small purple dots on the purple curve are simulated data points for $Zn = 10^{-5} nM, 10^{-6} nM, 10^{-7} nM$, respectively[23]. The three small green dots on the green curve are simulated data points for $Zn = 10^{-5} nM, 10^{-6} nM, 10^{-7} nM$, respectively. The area highlighted in gray is the range of parameter Zn between the half maximal induction points on the two simulated curves.

As shown in Fig. 5.3a, due to the binding of free zinc, the simulated concentration of Zn_2Zur ($Py(t)$, the Zur dimer which contains two zinc ions per dimer and it is used in the corresponding real assay [163]) quickly decreases from 25 nM to a steady state value of 0.044 nM whereas the simulated concentration of active Zur ($Py_1(t)$, the Zur dimer which contains four zinc ions per dimer) quickly rises from 0 to 21.6 nM. The simulated concentration of RNA polymerase ($Rw(t)$) decreases slightly from 50 nM to 49.5 nM due to the effect of its binding with *znuC* DNA.

As we can see from Fig. 5.3b, the simulated free *znuC* DNA concentration ($Dw(t)$) decreases rapidly (in 0.4 seconds) from 4 nM to a steady state of 0.14 nM during the first phase due to the binding of active Zur and RNA polymerase. The simulated concentration of the transcription initiation complex ($Qw_1(t)$) rapidly increases (in 0.4 seconds) from 0 to a steady state value of 0.47 nM whereas the simulated concentration of Zn_4Zur-DNA complex ($Qw_2(t)$) quickly increases (in 0.6 seconds) from 0 to 3.39 nM. The initiation of the second phase seems to only have a small influence on the afore mentioned steady state values (e.g., the steady state values of $Qw_1(t)$ and $Qw_2(t)$ change from 0.47 nM and 3.39 nM at the end of first phase to 0.45 nM and 3.4 nM at the end of the second phase, respectively). From Fig. 5.3c, we can see that in the first 30 minutes, the concentration of mRNA of ZnuC ($Mw(t)$) remains at 0 because the real transcription has not happened yet, and then in the subsequent 15 minutes it increases linearly from 0 to a final concentration of 4.49 nM.

The rapid decrease in the concentration of free *znuC* DNA ($Dw(t)$) shown in Fig. 5.3b is due to the binding of *znuC* DNA with active Zur (Zn_4Zur) and RNA polymerase. Since in the whole process, the total increase in the simulated concentration of Zn_4Zur-DNA complex ($Qw_2(t)$) is 3.4 nM, whereas the total decrease of the simulated free *znuC* DNA concentration is about 3.86 nM, we can conclude that when $Zn = 10^{-5} nM$, the binding of

[23] The simulated transient curves of Zur and ZntR transcription assays for $Zn = 10^{-5} nM$ are shown in Fig. 5.3a-c and Fig. 5.6, respectively. More simulated transient curves for $Zn = 10^{-6} nM, 10^{-7} nM$ are show in Fig. 5.4, Fig. 5.5, Fig. 5.7 and Fig. 5.8.

active Zur consumes the majority of the *znuC* DNA to form the Zn_4Zur-DNA complex, which can not further bind with RNA polymerase, and in this way the transcription of *znuC* is repressed.

We performed many simulations for various values of Zn (in the range of 10^{-18} M to 10^{-12} M) and recorded the final values of the simulated mRNA concentration ($Mw(t = t_{d0} + t_d)$). After normalizing these concentration values, depicting them as a function of Zn (in logarithm), and smoothly connecting these simulated data points, we obtained the purple curve in Fig. 5.3d (please note that only three simulated data points for Zur assay are shown as small purple dots in this figure to avoid confusion with the experimental data points).

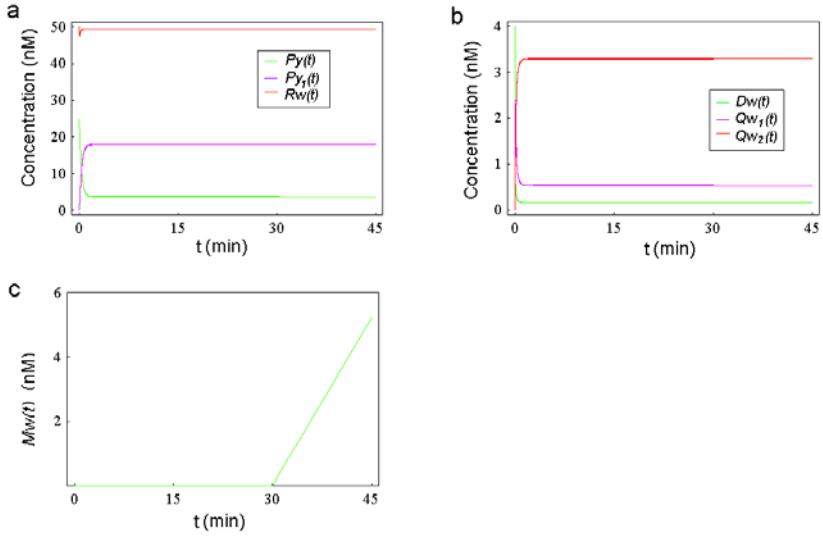

Figure 5.4. Transient Curves of Simulated Zur Transcription Assay for $Zn = 10^{-6} nM$.

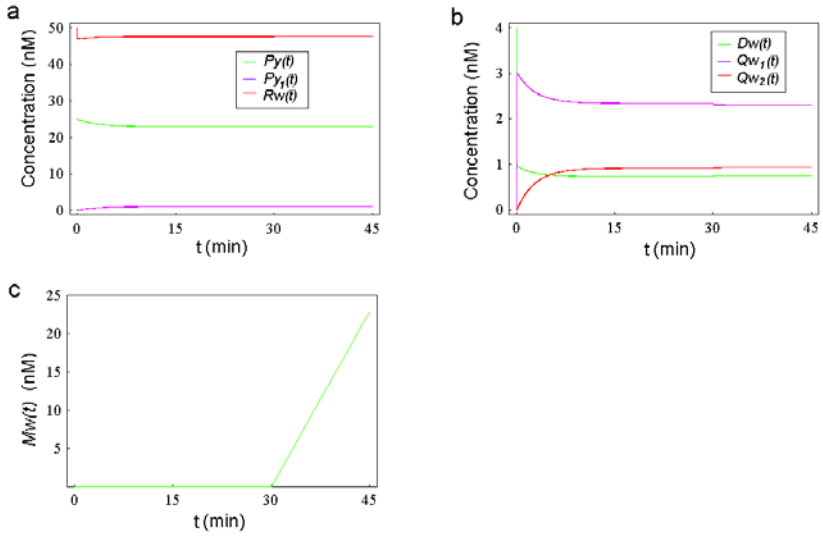

Figure 5.5. Transient Curves of Simulated Zur Transcription Assay for $Zn = 10^{-7}\,nM$ **.**

5.3.3 ZntR Transcription Assay (I)

Similarly, the ZntR run-off transcription assay can also be simulated by a two-phase sub-model. The first phase (the preliminary equilibrium phase) involves 6 reactions (Reactions 1,2,4,5,7,8), which are expressed as 9 ODEs (see Section 5.2.2.3). The second phase (the transcription phase) involves 9 reactions (Reactions 1-9), which are expressed as 10 ODEs (see Section 5.2.2.3). By setting the initial conditions of the simulation to be the same as those used in the real experiment ($Px(0) = Px_{tot} = 25nM, Dz(0) = D_0 = 4nM, Rz(0) = R_0 = 50nM$ and setting all the remaining initial concentrations to be 0), and subsequently solving the relevant equations of the two-phase sub-model, we can depict the relevant transient curves for $Zn = 10^{-5}\,nM$ as shown in Fig. 5.6 (for the remaining parameters, please see Table 5.2). In this assay, Reaction 14 is not included in the sub-model because the ZntR concentration is too low to challenge the buffering capacity of TPEN (of course we can also perform numerical simulations by including Reaction 14, although further investigations have shown that we essentially get the same results).

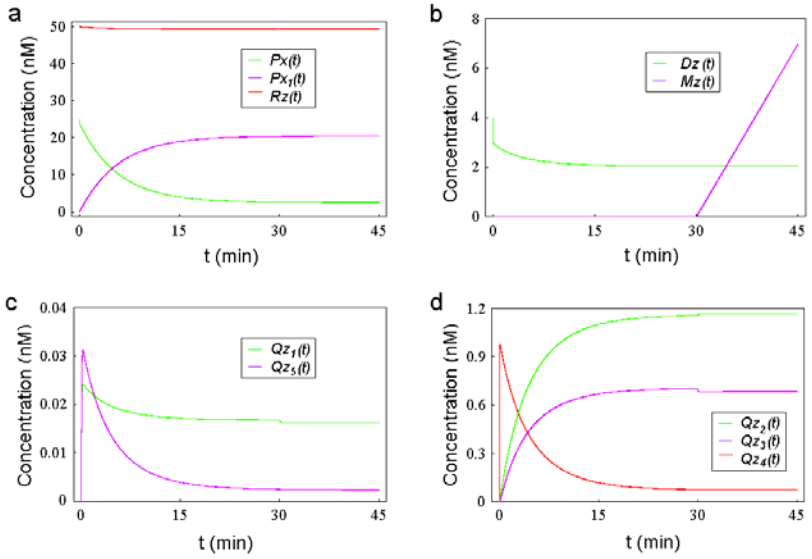

Figure 5.6. Transient curves of simulated ZntR transcription assay (I) for $Zn = 10^{-5}\,nM$.

(a) The green, purple and red curves denote the simulated transient curves of apo-ZntR (Px), ZnZntR (Px_1), RNA polymerase (Rz) concentrations as a function of t, respectively. (b) The simulated concentrations of the free *zntA* DNA (i.e., Dz, green curve) and mRNA of ZntA (i.e., Mz, purple curve) are depicted as a function of t. (c) The green and purple curves denote the simulated transient curves of transcription initiation complexes (Qz_1 and Qz_5) concentrations as a function of t, respectively. (d) The green, purple and red curves denote the simulated transient curves of ZnZntR-DNA complex (Qz_2), transcription initiation complex (Qz_3) and apo-ZntR-DNA complex (Qz_4) as a function of t, respectively.

From Fig. 5.6a we can see that due to the binding with free zinc, the simulated concentration of apo-ZntR ($Px(t)$) decreases from 25 nM to 2.59 nM, whereas the simulated concentration of active ZntR ($Px_1(t)$) rises from 0 to 20.5 nM, and the simulated concentration of RNA polymerase ($Rz(t)$) decreases slightly from 50 nM to 49.3 nM. In the first phase, due to the binding with ZntR and RNA polymerase, the simulated unbound *zntA* DNA concentration ($Dz(t)$) decreases rapidly (in 0.04 minutes) from 4 nM to 3.03 nM and then decreases gradually to 2.04 nM at the end of the first phase (Fig. 5.6b, green curve); in the second phase, the free *zntA* DNA concentration remains at roughly the same level (2.05 nM). The simulated *zntA* mRNA concentration ($Mz(t)$) remains at 0 nM during the first phase, as there is no transcription happening, and then increases seemingly linearly to a final concentration of 6.96 nM during the second phase after NTPs have been added (Fig. 5.6b, purple curve).

The simulated transients curves in Fig. 5.6c show that $Qz_1(t)$ rapidly rises (in 0.3 minutes) from 0 to a peak value of 0.024 nM and then gradually decreases to 0.017 nM during the first 30 minutes whereas $Qz_5(t)$ rapidly rises (in 0.26 minutes) from 0 to a peak value of 0.031 nM and then gradually decreases to a 0.0025 nM during the first phase. The initiation of the second phase causes a small decrease in the values of $Qz_1(t)$ and $Qz_5(t)$ (to 0.016 nM and to 0.0023 nM, respectively). As shown in Fig. 5.6d, both $Qz_2(t)$ and $Qz_3(t)$ rise first (from 0 to 1.16 nM and 0.7 nM, respectively) during the first phase whereas $Qz_4(t)$ first dramatically increases up to a peak value of 0.97 nM and then gradually decreases to its final value of 0.076 nM. The initiation of the second phase causes a small decrease in the value of $Qz_3(t)$ and a slight increase in the value of $Qz_2(t)$, as judged by the small kinks in the corresponding two curves, whereas it has insignificant influence of the value of $Qz_4(t)$.

Using similar methods we can obtain the green curve in Fig. 5.3d for the final values of the simulated mRNA concentration ($Mz(t = t_{d0} + t_d)$) as a function of the value of Zn (in logarithm). The results shown in Fig. 5.3d indicate that when the simulated free zinc concentration ranges from 10^{-18} M to 10^{-12} M, the simulated normalized final concentrations of mRNA of ZnuC ($Mw(t = t_{d0} + t_d)$) decreases from 100% to 15.05%, whereas the simulated normalized final concentration of mRNA of ZntA ($Mz(t = t_{d0} + t_d)$) increases from 7.4% to 100%. The half-maximal induction of *znuC* transcripts and the half maximal induction of *zntA* transcripts occur at $Zn = 2 * 10^{-16} M$ and $Zn = 1.15 * 10^{-15} M$ respectively, which are the same as previously reported values [163]. The simulated purple curve (for the Zur transcription assay) agrees with corresponding experimental data (the red dots) extremely well. Similarly the simulated green curve (for the ZntR transcription assay) also agrees with the corresponding experimental data (the blue dots), although to a slightly lesser degree [163].

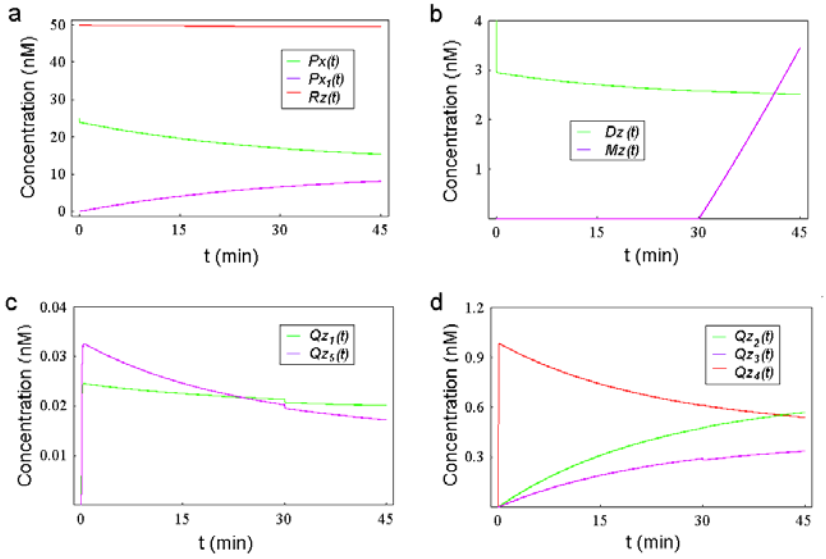

Figure 5.7. Transient Curves of Simulated ZntR Transcription Assay (I) for $Zn = 10^{-6}\,nM$ **.**

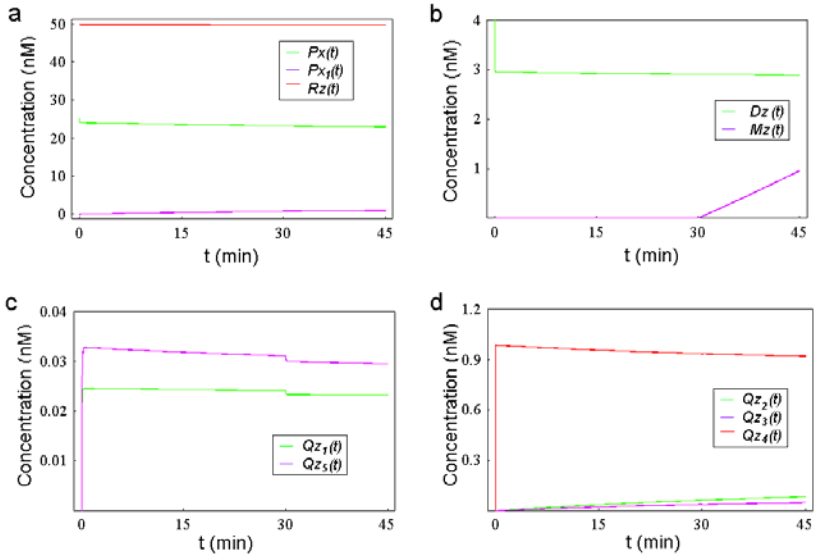

Figure 5.8. Transient Curves of Simulated ZntR Transcription Assay (I) for $Zn = 10^{-7}\,nM$ **.**

5.3.4 ZntR Transcription Assay (II)

In this assay, we take into consideration the competition between ZntR and TPEN for zinc binding by including Reaction 14 (see Table 5.1). Again, we will use a two-phase sub-model to simulate the real assay. The first phase (the preliminary equilibrium phase) of the assay (II) involves 7 reactions (Reactions 1,2,4,5,7,8,14), which are expressed as 12 ODEs (see Section 5.2.2.4). The second phase (the transcription phase) involves 10 reactions (Reactions 1-9,14), which are expressed as 13 ODEs (see Section 5.2.2.4). By setting the initial conditions of the simulation equal to those used in the experiment [164] ($\begin{matrix} Tp(0) = TPEN_{tot} = 10\mu M, Zn(0) = Zn_{tot}, Px(0) = Px_{tot}, \\ Dz(0) = D_0 = 2nM, Rz(0) = R_0 = 100nM \end{matrix}$ and all the remaining initial concentrations are set to 0) and solving the two-phase model, we depict the simulated final concentrations (in nM) of mRNA of ZntA ($Mz(t = t_{d0} + t_d)$) for $Zn_{tot} = 10\mu M$ and $Zn_{tot} = 0$ as a function of the logarithm of the doubled value of parameter Px_{tot} (i.e., $[ZntR]_{total}$ which denotes the total concentration of the ZntR monomer) and we obtain the purple and green curves shown in Fig. 5.9a.

We also perform many simulations under the following initial conditions:
($\begin{matrix} Tp(0) = TPEN_{tot} = 10\mu M, Zn(0) = Zn_{tot}, Px(0) = Px_{tot} = 50nM, \\ Dz(0) = D_0 = 2nM, Rz(0) = R_0 = 100nM \end{matrix}$
and all the remaining initial concentrations are set to 0) for various values of Zn_{tot} within the range of 100nM to 100μM and eventually obtain the black curve shown in Fig. 5.9b which describes the final values of the simulated mRNA concentration ($Mz(t = t_{d0} + t_d)$) as a function of the value of Zn_{tot} (in logarithm).

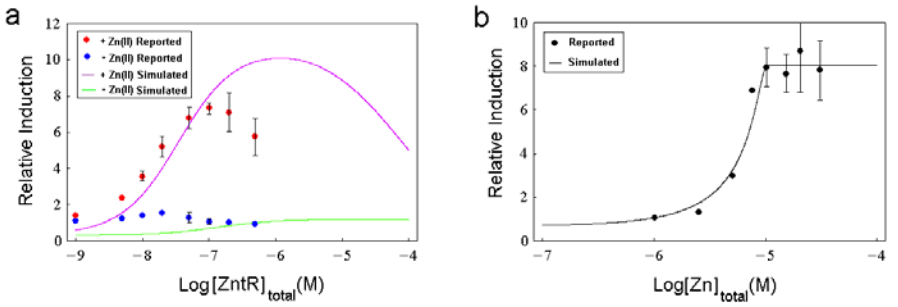

Figure 5.9. Comparison of simulated results and experimental data (II).

(a) ZntR transcription assay with Zn(II) or without Zn(II). Red dots for the case of with Zn(II) and green dots for the case of without Zn(II) are reconstructed from the reported data in the original figure (Fig. 6B in Ref. 164) using image analysis. *Error bars* indicate a standard deviation both above and below the average values of two separate experiments. The purple line and the green line are the corresponding simulated final concentrations (in nM) of mRNA of ZntA (i.e., $Mz(t = t_{d0} + t_d)$) in the cases of

parameter $Zn_{tot} = 10\mu M$ and $Zn_{tot} = 0$ as a function of the logarithm of $[ZntR]_{total}$ (i.e., $2 * Px_{tot}$), respectively. (b) ZntR transcription assay with varying total zinc concentration. The black dots are reconstructed from the reported data in the original figure (Fig. 6C in Ref. 164) using image analysis. The black curve is the simulated final concentration (in nM) of mRNA of ZntA (i.e., $Mz(t = t_{d0} + t_d)$) as a function of the logarithm of parameter Zn_{tot} (also denoted as $[Zn]_{total}$).

5.4 Discussion

The simulation results shown in Fig. 5.6 indicate the complex interactions among three transcription processes of *zntA* (the constitutive transcription, the apo-ZntR activated transcription and the ZnZntR activated transcription). If we compare the dynamics of the simulated concentrations of three transcription initiation complexes involved in the ZntR transcription assay (i.e., $Qz_1(t), Qz_3(t)$ and $Qz_5(t)$) as shown in Fig. 5.6c and Fig. 5.6d, we find that the dynamics of $Qz_1(t)$ and $Qz_5(t)$ are quite similar. Initially, they both increase rapidly, form low peaks (the peak values are 0.024 nM and 0.031 nM, respectively), and then gradually decrease. In contrast, the dynamics of $Qz_3(t)$ only demonstrates a gradual increase to 0.7 nM in the first 30 minutes. The observation that the final steady state value of $Qz_3(t)$ (0.69 nM) is much higher than those of $Qz_1(t)$ and $Qz_5(t)$ (0.016 nM and 0.0023 nM, respectively) indicates that for $Zn = 10^{-5} nM$, when the system (excluding $Mz(t)$) enters its final equilibrium, the dominating transcription process is ZnZntR activated transcription rather than the other two transcription processes (i.e., the constitutive transcription and the apo-ZntR activated transcription, please refer to Section 5.2.1 for more details).

To explain why the dynamics of $Qz_1(t)$ shows a peak, we suggest that the initial increase of $Qz_1(t)$ is due to the binding of *zntA* DNA with RNA polymerase. Then following the conversion of apo-ZntR to active ZntR by zinc-binding (see the green and purple curves in Fig. 5.6a), active ZntR binds with *zntA* DNA to form the ZnZntR-DNA complex (see the green curve in Fig. 5.6b and the green curve in Fig. 5.6d). This competitive binding of active ZntR causes a sudden decrease in the free *zntA* DNA concentration (see the green curve in Fig. 5.6b) and the reversible Reaction 2 (see Table 5.1) becomes dominated by its reverse side and $Qz_1(t)$ begins to decrease after forming a small peak. Similarly, we can explain the dynamics of $Qz_5(t)$.

By comparing the dynamics of the simulated Zur and ZntR transcription assays shown in Fig. 5.3a-c and Fig. 5.6, we can see that when $Zn = 10^{-5} nM$, during the first phase, the simulated Zur transcription system reaches its steady state in less than 20 seconds, much faster than the simulated ZntR transcription system which takes more than 20 minutes. As shown in Fig. 5.3c and Fig. 5.6b, the seemingly linear increase of the simulated concentrations of mRNA ($Mw(t)$ and $Mz(t)$) during the second phase indicates the progress of the relevant transcription processes. If we calculate the slope of the linear curve in Fig. 5.3c as follows:

$Mw(t = t_{d0} + t_d) / Qw_1^s / t_d = 4.49nM / 0.45nM / 15\min = 0.011s^{-1}$ where Qw_1^s denotes the final steady state value of $Qw_1(t)$, we derive the same value as that of the transcription rate parameter k_3 (see Table 5.2). Obviously the simulated final concentrations of mRNA ($Mw(t = t_{d0} + t_d)$ and $Mz(t = t_{d0} + t_d)$) are generally proportional to t_d, which is in accordance with the experimental observation that the harvest of run-off transcription assay is related to the duration time of its transcription phase (t_d).

The purple curve in Fig. 5.9a indicates that for $Zn_{tot} = 10\mu M$, when the simulated total ZntR monomer concentration ($[ZntR]_{total}$ which is twice the value of Px_{tot}) ranges from 10^{-9} M to 10^{-4} M, the simulated final concentrations of *zntA* mRNA ($Mz(t = t_{d0} + t_d)$) increases from 0.59 nM to a peak value of 10.09 nM when $[ZntR]_{total} = 10^{-5.92} M$ and then decreases to 4.99 nM. If we look at the corresponding experimental data (the red dots) [164], we can see that the relative induction of the *zntA* transcripts increases, forms a peak (when $[ZntR]_{total} = 10^{-7} M$), and eventually declines. Thus our simulation successfully simulates the peak behaviour of the relative induction of the *zntA* transcripts for increasing values of $[ZntR]_{total}$ in the presence of zinc. Further investigations show that if we perform the simulations excluding Reaction 14, then we can only reproduce the increasing behaviour rather than the peak behaviour. Thus one potential explanation for the peak behaviour is that, for low ZntR concentrations, TPEN is strong enough to buffer the zinc and more ZntR will promote the transcription of *zntA* gene; while for high ZntR concentrations, the buffering capacity of TPEN is exceeded and the free zinc concentration can not be maintained as a constant anymore and it subsequently decreases due to the binding of over-abundant ZntR molecules, which in turn limits the transcription processes. A similar comparison can be made for the case when $Zn_{tot} = 0$ (i.e., in the absence of zinc, please see the green curve and the blue dots in Fig. 5.9a). However, in the latter case, our model can only simulate the initial increase, but fails to reproduce the decline.

As described in detail in Section 5.2.1**,** in this model, we assume that the active form of ZntR is ZnZntR because metal occupancy assays of ZntR monitored by changes in tyrosine fluorescence show noncooperative 1:1 binding of Zn(II) to the ZntR dimer [103]. This assumption is valid only when the free zinc concentration and total ZntR concentration are both extremely low (in sub-nM and nM range, respectively). When the total ZntR concentration goes to the μM range, the binding kinetics of Zn(II) to the ZntR dimer will be more complicated because ZntR can bind one or two zinc ions per dimer depending on the buffer conditions [164,172]. This explains why, as shown in Fig. 5.9a in the case of with Zn(II), there is a disagreement between the simulation results (the purple curve) and the corresponding experimental data (the red dots) when ZntR molecules are relatively abundant. Intuitively, we can think of it in this way: in the real case, the competitive ability of ZntR for Zn(II) binding is stronger than the model prediction because at high ZntR concentrations, ZntR, on average, binds with more than one ion per dimer. This results in a smaller and earlier peak because the buffering

capacity of TPEN is now easier to exceed. In the absence of Zn(II), the eventual abnormal decline in the experimental data (see the blue dots in Fig. 5.9a) may be due to the normal deviations of the different experiments because the levels of *zntA* transcript are very low in this case[24] or perhaps this is due to some novel, unknown mechanisms [164].

As we can see from Fig. 5.9b, when the simulated total zinc concentration (Zn_{tot}) ranges from 10^{-7} M to 10^{-4} M, the simulated final concentration of mRNA of ZntA ($Mz(t = t_{d0} + t_d)$) increases from 0.72 nM to 8.04 nM (saturation occurs when $Zn_{tot} = 10^{-5} M$) which means that more abundant free zinc ions bind with ZntR to promote activation of the transcription of the *zntA* gene. The simulated curve (the black curve) fits the experimental data (the black dots) [164] quite well.

As previously mentioned, cytoplasmic zinc trafficking in *E. coli* may involve chaperone-like proteins whose existence is still being debated [66,155,163]. Outten *et al.* demonstrated *in vitro* that ZntR and Zur are sensitive to very low concentrations (femtomolar) of free zinc (also see Fig. 5.3d), therefore they proposed that free zinc in the cytosol of *E. coli* is not physiologically available under normal growth conditions [163]. Our simulation results further confirm their experimental data and support their proposal. However, in order to better understand the *in vivo* transcriptional regulation mechanisms of zinc homeostasis, further investigations are required to simulate the *in vivo* transcription processes and their responses to various environmental conditions.

Up until now, performing well-designed *in vitro* experiments has been one of the common ways used to infer the various characteristics of the corresponding *in vivo* systems. The current work provides a good example of how to use a unified mathematical model to explain complicated datasets obtained from *in vitro* metal-binding and transcription experiments which have been widely performed for metal ion homeostasis and detoxification systems [103,158,163,164]. The repression of Zur on the transcription of *znuACB* gene cluster and the activation of ZntR on the *zntA* transcription constitute the critical parts of the regulatory mechanisms of the zinc homeostasis system in *E. coli* (see Fig. 5.1a). This means that if we want to make predictive and useful model for the *in vivo* zinc homeostasis system, we need to model these transcriptional regulations. Although the current model only simulates the *in vitro* kinetics, together with its fitted rate constants it can be used as a good basis and reference for the future modelling of the corresponding *in vivo* system. Moreover, the quantitative distinguishment of the three transcription processes of *zntA* (the constitutive transcription, the apo-ZntR activated transcription and the ZnZntR activated transcription) in our model will be quite meaningful for modelling the *in vivo* system and it provides the possibility of including any additional regulations on these three processes which do happen *in vivo* [33,164].

[24] Please note that the error bars shown in Fig. 5.9a indicate the standard deviation from the average values of only two separate experiments and there are only two data points having error bars for the case of without Zn(II).

To conclude, we have built a mathematical model for simulating the *in vitro* transcriptional response of zinc homeostasis system in *E. coli.* Simulation results show that our model can quantitatively reproduce the various results of the *in vitro* experiments conducted by Outten CE and her colleagues. Our model gives a detailed insight into the involved system dynamics and provides a general framework for simulating *in vitro* metal-binding and transcription experiments and interpreting relevant experimental data.

Coupled feedback loops have been recently recognized as essential building blocks (i.e., network motifs) of cellular networks [115]. The zinc homeostasis system in *E. coli* is a good example of such a building block because it follows from Fig. 5.1a that Zur and ZnuC form a 'negative circuit', since active Zur represses *znuC* (negative action) while zinc influx via ZnuC leads to larger amounts of active Zur molecules (positive action). Similar considerations point towards the negative circuit wiring betwen ZntR and ZntA (also see Fig. 6.3a). It is believed that such coupled negative feedback loops are quite helpful for enhancing homeostasis (see Table 6.1) [115]. Besides feedback loops, many other network motifs have been defined in cellular networks. In Chapter 6, we will enumerate various network motifs found in metal ion and homeostasis systems and try to give a preliminary study of the general design principles of these systems.

Chapter 6 Network Motifs and Their Functions[25]

6.1 Introduction

Networks arise naturally in biology for describing the intricate interactions of biological entities. To uncover the design principle of dauntingly complex networks and understand their dynamics, Uri Alon and his colleagues (2002) defined "network motifs" which can be thought of as recurring circuits of interactions and regarded as the building blocks of complex networks [193]. Just as each door or window, which is the building block of normal buildings, has its specific structure and functions, each network motif has its specific structure and is believed to carry out specific information-processing functions. Since these networks motifs are typically small size circuits of interactions and are relatively easy to analyze using mathematical models, the understanding of the specific functions of network motifs has been believed by Alon *et al.* and many other people to be a nice way to help illuminate the dynamics of much more complex systems in which each motif appears [10,11,115].

Network motifs were first systematically defined in the transcription network of *E. coli* and have later been found in organisms from bacteria and yeast to plants and animals. An incomplete summary of network motifs and their functions is shown in Table 6.1.

Table 6.1: Network motifs and their functions.

Name		Pattern	Functions	Description
Auto-regulation	Positive autoregulation (PAR)		In transcription networks, PAR slows down the response time of gene circuits and can usually enhance cell-cell variation [10,11].	Component X regulates itself.
	Negative autoregulation (NAR)		In transcription networks, NAR speeds up the response time of gene circuits and can reduce cell–cell	

[25] This Chapter is based on: Jiangjun Cui and Jaap Kaandorp, The modulation on the properties of signaling cycle motif by an inhibitor (in preparation).

			variation in protein levels [10,11].	
Feed-Forward Loop (FFL)	Coherent type-1 FFL (C1-FFL)		In transcription networks, the C1-FFL is a 'sign-sensitive delay' element and a persistence detector [10].	Component X regulates component Y and both of them regulate Z.
	Incoherent type-1 FFL (I1-FFL)		In transcription networks, the I1-FFL is a pulse generator and response accelerator [10].	
	Other FFLS	See Fig. 6.1	Not totally defined	
Single-Input Module (SIM)		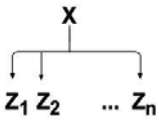	In transcription networks, SIM allows coordinated expression of a group of genes with shared function. It can generate a temporal expression program, with a defined order of activation of each of the target promoters [10,11,193].	Component X regulates a group of other components (Z_1, Z_2,…, Z_n).
Bifan		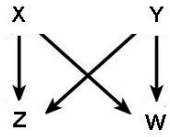	Not well defined [109]	Component X regulates both Z and W. At the same time, component Y regulates both Z and W.
Diamond		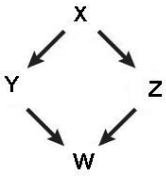	Not totally defined	Both components Y and Z are regulated by X and at the same time,

				both Y and Z regulate W.
Feedback Loop with Two nodes	Positive feedback loops (PFL)	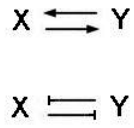	In signal transduction networks, PFL amplifies the signal and results in slower response. It can also lead to bistability and hysteresis [115].	Components X and Y regulate each other. In PFL, both X and Y positively regulate each other; or both of them negatively regulate each other. In NFL, only one regulation is positive and the other one is negative.
	Negative feedback loops(NFL)	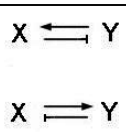	NFL helps maintaining homeostasis and plays important role in signal adaptation or desensitization to sustained stimulation. It functions as noise filters and accelerates signal responses [115].	
Coupled Feedback Loops	Two positive feedback loops (PP)	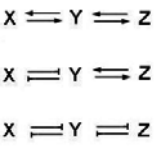	PP induces a slower but amplified signal response and enhances bistability [115].	Components X and Y regulate each other. At the same time, Y and Z regulate each other.
	A positive feedback loop and a negative feedback loop (PN)	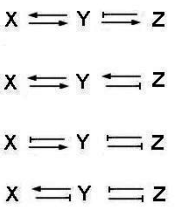	PN guarantees reliable decision-making by properly modulating signal responses and effectively dealing with noise [114,115].	
	Two negative feedback loops (NN)	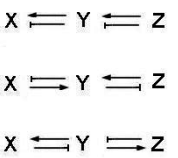	NN enhances sustained oscillations and homeostasis [115].	

Signaling Cycle (SC)	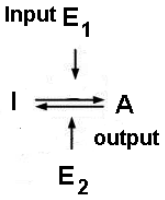	SC can amplify the response to a certain stimulus and provide additional sensitivity in biological control. (Typically, the concentration of E_1 is regarded as input and the concentration of active protein is regarded as output) [83,84]	Enzyme 1 (E_1, a kinase) activates a protein (I denotes the its inactive state and A denotes its active state) whereas Enzyme 2 (E_2, a phosphatase) deactivates the protein.

Although numerous papers have discussed network motifs and their functions in various kinds of networks including transcription networks (sensory transcription networks and developmental networks), neuronal networks and signal transduction networks, there is no systematic study reported for discussing networks motifs and their functions in metal ion homeostasis and signaling systems. The aim of this Chapter is to present a preliminary study on this topic. Hopefully such a study will help us to gain some insight into the general designing principles of metal ion homeostasis and signaling systems.

6.2 Network Motifs in Metal Ion Homeostasis and Signaling Systems

As mentioned in Section 1.3.3.2 and 1.3.3.3, metal ion homeostasis systems frequently contain transcriptional regulations on various proteins (ion channels or transporters, metal-using proteins, chaperones and regulatory proteins). Moreover, metal ion signaling systems are specific types of signal transduction systems. Therefore, it is not surprising that many network motifs found in the transcription networks and signal transduction networks also exist widely in the metal ion homeostasis and signaling systems. Here we will give a number of examples and then mainly focus on the signaling cycle motif and study the modulation on its properties by an inhibitor using mathematical model.

6.2.1 Examples of Network Motifs

Autoregulation motif is the simplest motif firstly defined in transcription networks. Positive autoregulation occurs when a transcription factor X activates the transcription of its own gene. In contrast, negative autoregulation occurs when X represses the

transcription of its own gene [10,11,193]. In metal ion homeostasis and signaling systems, many central transcriptional regulators have autoregulations. For instance, the activator Zap1 in yeast zinc homeostasis system (see Fig. 1.2) has positive autoregulation [133]. Fur, the critical repressor in the iron homeostasis system of *E. coli*, has weak negative autoregulation although Fur concentrations do not change significantly in response to iron availability [55]. The repressor CopY in *E. hirae* copper homeostasis system represses the transcription of its own gene [202]. However, no autorgulation of Zur, the critical repressor in the zinc homeostasis system in *E. coli*, was observed [167].

The second important family of network motifs is the feedforward loop. Because each of the three regulatory interactions (see Table 6.1, the regulations of X on Y, Y on Z and X on Z) in the FFL can be either activation or repression, there are totally eight possible structural types of FFL which can be classified into two groups (coherent and incoherent FFLs) as shown in Fig. 6.1 [10,11].

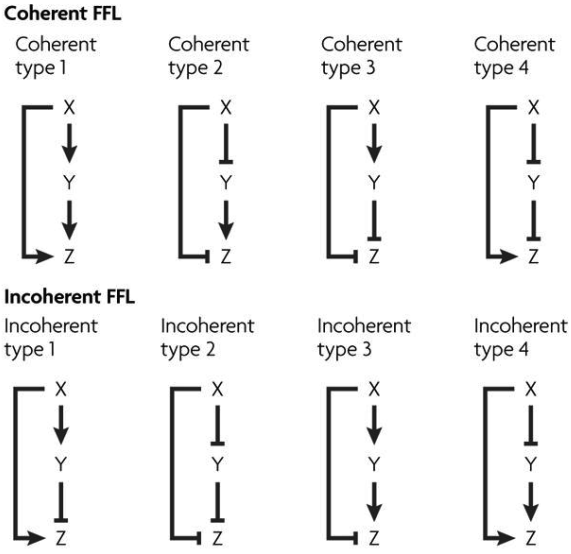

Figure 6.1. Coherent and incoherent FFLs. In coherent FFLs, the indirect regulation of X on Z through Y is coherent with its direct regulation on Z. For example, in coherent type 1 FFL, X activates Y and Y activates Z, thus the indirect regulation of X on Z through Y is activation, which is coherent with the directly activating regulation of X on Z (this figure is taken from [11]).

FFL appears in hundreds of gene systems in various organisms. However, in metal ion homeostasis and signaling systems, FFL is not common. One example of FFL can be found in the zinc homeostasis system in *S. cerevisiae* (see Fig. 1.2), in which cytoplasmic zinc regulates the membrane concentration of Zrt1 both directly (excessive cytoplasmic zinc results in the inactivation of Zrt1 through endocytosis and vacuolar degradation) and indirectly (through Zap1) [133].

The third family of network motifs, SIM motif, exists extreme widely in metal ion and homeostasis and signaling systems because in these systems, it is very common that a single regulator has multiple targets. A good example of SIM motif found in yeast zinc homeostasis system has been described in Fig. 1.7d. Another SIM motif example is that Crz1, the central transcription factor in yeast calcium homeostasis/signaling system, regulates multiple target genes including *PMC1* and *PMR1* [208]. There are many other examples, for instance, in *E. hirae* copper homeostasis system, CopY represses the expression of genes encoding CopA (the uptake ATPase), CopB (the efflux ATPase), CopZ (the chaperone) and itself [202].

Feedback loop motifs are very common in metal ion homeostasis systems. In addition to the example described in Fig. 1.7b, here we give more examples of feedback loop motifs as shown in Fig. 6.2.

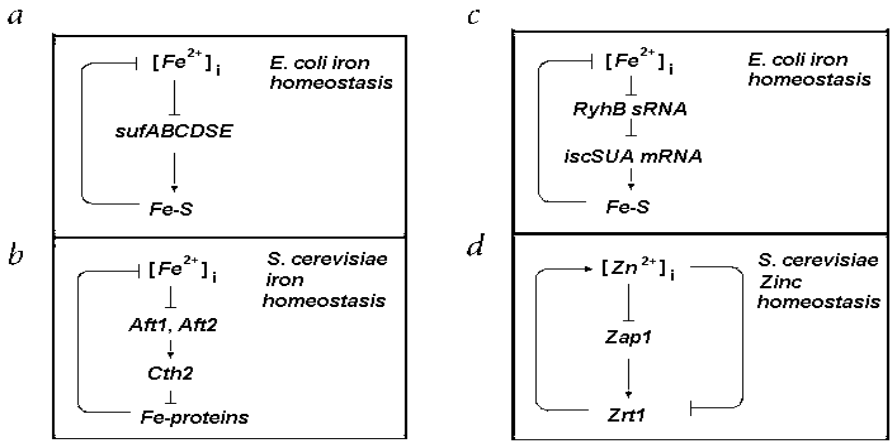

Figure 6.2. More examples of feedback loop motifs. (a). An example of feedback loop motif found in *E. coli* iron homeostasis system. Cytoplasmic Fe^{2+} (i.e., $[Fe^{2+}]_i$) in *E. coli* represses the *suf* operon (encoded by *sufABCDSE*) which is involved in [Fe-S] cluster formation [191]. (b). A feedback loop example found in *E. coli* iron homeostasis system. Cytoplasmic Fe^{2+} in *E. coli* represses a small RNA (sRNA) named as RyhB, which facilitates the degradation of *iscSUA* transcripts. iscSUA are parts of the *isc* operon (encoded by *iscRSUA*) which are involved in [Fe-S] cluster formation [191]. (c). A feedback loop motif example found in the iron homeostasis system in *S. cerevisiae*. In response to iron starvation, the iron-responsive transcription factors Aft1 and Aft2 activate Cth2 which facilitates the degradation of mRNAs encoding Fe-using proteins [142]. (d). A coupled negative feedback loop motif example found in the zinc homeostasis system in *S. cerevisiae*. Under zinc-limiting conditions, zinc-responsive transcription factor Zap1 activates Zrt1. Moreover, excessive cytoplasmic zinc results in the inactivation of Zrt1 through endocytosis and vacuolar degradation [202].

Very frequently, biological cells use coupled feedback loop pathways for the regulations of metal ion and homeostasis and signaling systems. For example, the feedback loops shown in Fig. 1.7b and Fig. 6.2a-c are all coupled with each other and function together to maintain iron homeostasis in *E. coli*. Fig. 6.2d shows a good example of coupled negative feedback loops motif (i.e., coupled NN motif; for the definition of NN, please

see Table 6.1) found in the yeast zinc homeostasis system. More examples of PN and NN network motifs are shown in Fig. 6.3.

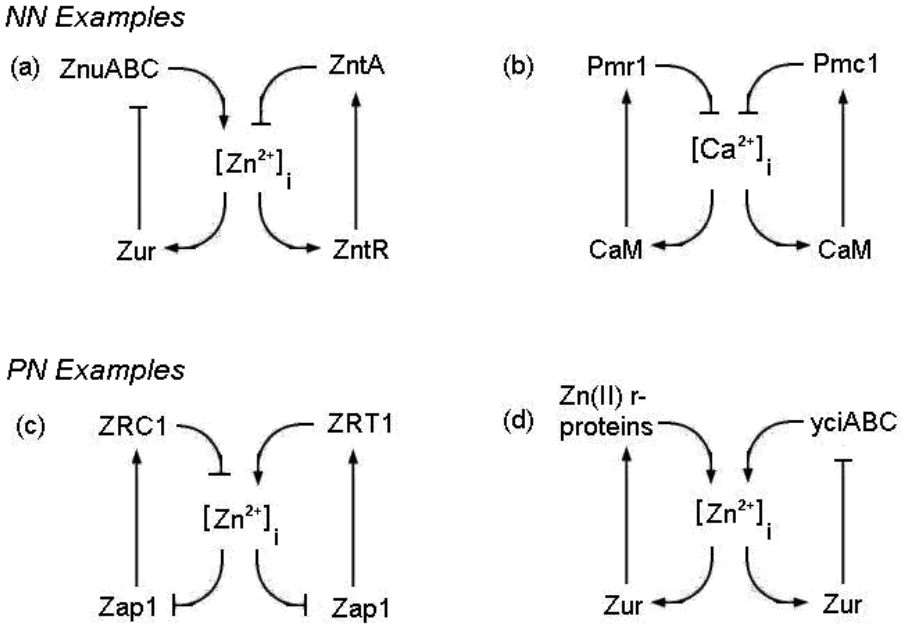

Figure 6.3. Examples of coupled feedback loops (NN and PN) motifs. (a). NN example found in *E. coli* zinc homeostasis system: the Zur-ZnuABC pathway is a negative feedback loop (NFL) and the ZntR-ZntA pathway is another NFL [163,172]. (b). NN example found in *S. cerevisiae* calcium homeostasis system: the CaM-Pmc1 pathway (more precisely, CaM-calcineurin-Crz1-Pmc1 pathway) is one NFL and the CaM-Pmr1 (more precisely, CaM-calcineurin-Crz1-Pmr1 pathway) pathway is another NFL [51,132]. (c). PN example found in *S. cerevisiae* zinc homeostasis system: the Zap1-ZRC1 pathway is a positive feedback loop (PFL) and the Zap1-ZRT1 pathway is a NFL [202]. (d) PN example found in *Bacillus subtilis* zinc homeostasis system: the Zur- Zn(II) r-proteins pathway is a PFL because Zur promotes mobilization of Zn(II) stored in Zn(II) r-proteins. In contrast, the Zur-yciABC pathway is a NFL [149]. CaM: calmodulin; yciABC: Zinc uptake transporter; Zn(II) r-proteins: Zn(II) containing ribosomal proteins.

6.2.2 Signaling Cycle Motif

Signaling cycle motif (see Table 6.1) is a cycle of covalent modification which is a ubiquitous building block of signaling pathways [83,84,213]. For example, in the Ca^{2+}-calcineurin-MCIP-NFAT signaling network shown in Fig. 4.1, there are 8 enzyme catalytic binding reactions (see Reactions 10-17 in Table 4.1) which constitute 4 signaling cycle motifs (e.g., Reactions 10 and 11 forms a signaling cycle: $\mathrm{MCIP} \underset{\mathrm{CaNc^*}}{\overset{\mathrm{BMKi}}{\rightleftharpoons}} \mathrm{MCIPp}$. Similarly, three other signaling cycles are formed by Reactions 12 and 13, Reactions 14 and 15, Reactions 16 and 17, respectively).

Although several modeling studies have been previously published about the properties of the signaling cycle motif [83,84], it is rarely noticed that in many cases, the appearance of signaling cycle is accompanied with an inhibitor as described in Fig. 6.4a. A good example (as described in Fig. 6.4b) is that protein 14-3-3 inhibits the NFAT signaling cycle formed by Reactions 14 and 15 in Table 4.1. Another example found in the signaling network shown in Fig. 4.1 is that protein 14-3-3 inhibits the $MCIP^{PP}$ signaling cycle formed by Reactions 12 and 13 in Table 4.1. What we are particularly interested in is how the accompanying inhibitor will modulate the properties of the signaling cycle motif.

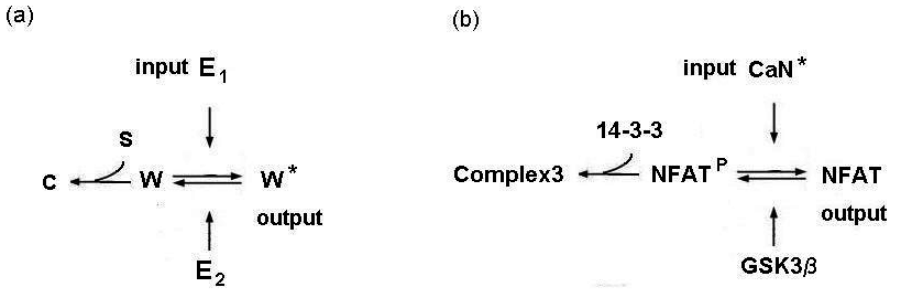

Figure 6.4. Signaling cycle with an inhibitor. (a). In signaling cycle motif, Enzyme E_1 activates protein W (to produce W^* which is the active form of W) and E_2 deactivates it. The inhibitor S binds with W to form a complex C which can not be activated by E_1. (b) An example of signaling cycle with an inhibitor found in Fig. 4.1. Here, protein 14-3-3 acts as the inhibitor.

The signaling cycle with an inhibitor can be represented as a set of three reactions in Cellerator form as follows:

$$\left\{\left\{W \overset{E_1}{\rightleftarrows} W^*,\ k_1,\ k_{-1},\ k_2\right\},\ \left\{W^* \overset{E_2}{\rightleftarrows} W,\ k_3,\ k_{-3},\ k_4\right\},\ \{S + W \rightleftarrows C,\ k_5,\ k_{-5}\}\right\}$$

The ordinary differential equations used for simulating the signaling cycle with an inhibitor are generated automatically using Cellerator. The detailed 8 equations are:

$$\frac{dC(t)}{dt} = -k_{-5}C(t) + k_5 S(t)W(t)$$

$$\frac{dE_1(t)}{dt} = -k_1 E_1(t)W(t) + k_2 W \cup E_1(t) + k_{-1} W \cup E_1(t)$$

$$\frac{dE_2(t)}{dt} = -k_3 E_2(t)W^*(t) + k_4 W^* \cup E_2(t) + k_{-3} W^* \cup E_2(t)$$

$$\frac{dS(t)}{dt} = k_{-5}C(t) - k_5 S(t)W(t)$$

$$\frac{dW(t)}{dt} = k_{-5}C(t) - k_5 S(t)W(t) - k_1 E_1(t)W(t) + k_4 W^* \cup E_2(t) + k_{-1} W \cup E_1(t)$$

$$\frac{dW^*(t)}{dt} = -k_3 E_2(t)W^*(t) + k_{-3} W^* \cup E_2(t) + k_2 W \cup E_1(t)$$

$$\frac{dW^* \cup E_2(t)}{dt} = k_3 E_2(t)W^*(t) - k_4 W^* \cup E_2(t) - k_{-3} W^* \cup E_2(t)$$

$$\frac{dW \cup E_1(t)}{dt} = k_1 E_1(t)W(t) - k_2 W \cup E_1(t) - k_{-1} W \cup E_1(t)$$

Where $C(t), S(t), W(t), W^*(t), E_1(t)$ and $E_2(t)$ denote the concentrations of species C, S, W, W^*, E_1 and E_2 respectively. $W \cup E_1(t)$ denotes the concentration of the intermediate complex formed by W and E_1. $W^* \cup E_2(t)$ denotes the concentration of the intermediate complex formed by W^* and E_2. $k_1, k_{-1}, k_2, k_3, k_{-3}, k_4, k_5, k_{-5}$ are rate parameters.

We numerically solve the above equations for various values of the total concentrations of the inhibitor (i.e., S^{tot}) and depict the steady state concentration of W^* (i.e., W^{*ss}) as a function of the total concentration of E_1 (i.e., E_1^{tot}) as shown in Fig. 6.5a.

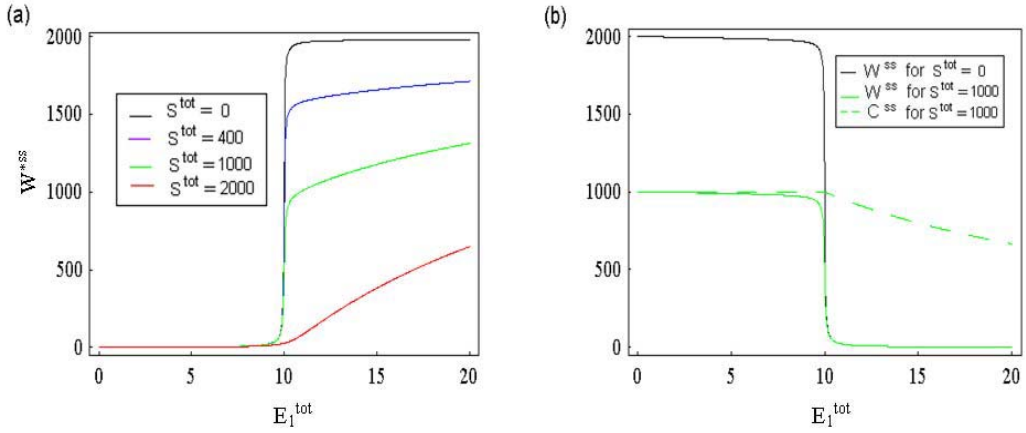

Figure 6.5. Modulation on the steady-state response of the signaling cycle by an inhibitor. (a) The black, blue, green and red curves describe the steady-state response curves

(W^{*ss} as a function of E_1^{tot}) for $S^{tot} = 0,400,1000,2000$, respectively. The rest parameter values are as follows: $k_1 = k_{-1} = k_2 = k_3 = k_{-3} = k_4 = k_5 = k_{-5} = 1, E_2^{tot} = 10, W^{tot} = 2000$. W^{tot} denotes the total concentration of W. In the simulations, the following initial conditions are used: $E_1(0) = E_1^{tot}, E_2(0) = E_2^{tot}, S(0) = S^{tot}, W(0) = W^{tot}$ and the initial values of all the rest variables are 0. (b) The black and green solid curves describe the steady-state concentration of W (i.e., W^{ss}) as a function of E_1^{tot} for $S^{tot} = 0$ and $S^{tot} = 1000$, respectively. The dashed green line describes the steady-state concentration of C (i.e., C^{ss}) as a function of E_1^{tot} for $S^{tot} = 1000$.

From Fig. 6.5a, we can see that for various values of S^{tot}, W^{*ss} hardly increases (from 0) when $E_1^{tot} < 9$. For $S^{tot} = 0$, W^{*ss} rises to less than 200 when E_1^{tot} increases from 9 to 9.9, then increases extreme rapidly to more than 1800 when E_1^{tot} increases from 9.9 to 10.1 and finally rises very gradually in a hyperbolic way to approximate its limit value (i.e., 2000) when E_1^{tot} increases from 10.1 to 20. We name the narrow range of E_1^{tot} ($9.9 \le E_1^{tot} \le 10.1$) as the critical region. For $S^{tot} = 400$, the end value of W^{*ss} during this critical region is around 1500, which is lower than that for $S^{tot} = 0$. For $S^{tot} = 1000$, the end value of W^{*ss} during this critical region is even lower (less than 1000) whereas for $S^{tot} = 2000$, there is little change of W^{*ss} during this critical region.

From Fig. 6.5b, we can see that for the signaling cycle without inhibitor (i.e., $S^{tot} = 0$, the black curve), the steady-state profile of W^{ss} is almost mirror symmetrical to that of W^{*ss} (i.e., the black curve in Fig. 6.5a) along the horizontal line $W^{*ss} = 1000$. This is because in this case, $W(t) + W^*(t) \approx W^{tot} = 2000$ (Please note that $W(t) + W^*(t) + W \cup E_1(t) + W^* \cup E_2(t) = W^{tot} = 2000$ and $W \cup E_1(t) + W^* \cup E_2(t) \le E_1^{tot} + E_2^{tot} \le 30$). For the signaling cycle with an inhibitor (i.e., $S^{tot} = 1000$, the green curve in Fig. 6.5b), when E_1^{tot}<9, both W^{ss} and C^{ss} are around 1000. Then W^{ss} extreme rapidly decreases to almost 0 during the critical region whereas C^{ss} gradually decreases when E_1^{tot} increases from 9.9 to 20 and the decreasing rate of C^{ss} is almost equal to the increasing rate of W^{*ss} shown in Fig. 6.5a (the green curve) because in this case, $W(t) + W^*(t) + C(t) \approx W^{tot} = 2000$.

6.3 Discussion

As we can see from Section 6.2.1, several kinds of network motifs such as autoregulation motif, SIM motif, feedback loop motif and coupled feedback loop motifs do exist widely in metal ion homeostasis and signaling systems. It is interesting to notice that relatively simple network motifs can be embedded in more complex network motifs, for instance, the coupled NN motif shown in Fig. 6.2d contains a FFL motif ($[Zn^{2+}]_i$ regulates Zrt1 both directly and indirectly). The coupled NN motif shown in Fig. 6.3a contains a SIM motif ($[Zn^{2+}]_i$ regulates both Zur and ZntR).

The great number of negative feedback loops shown in Fig. 6.2b-d and Fig. 6.3 confirms our previous statement that negative feedback controls constitute the central scheme for maintaining homeostasis. The various strategies used by biological cells for maintaining homeostasis as discussed in Section 1.3.3.2 and 1.3.3.3 can be represented in the framework of network motifs (especially feedback loop motifs). Thus investigations of the properties of the network motifs are quite important in order to gain insight into the general designing principle of metal ion homeostasis and signaling systems.

The most well-known characteristic of signaling cycle is that the steady-state response of this basic cycle can be in a highly sigmoidal (ultrasensitive) regime as can be clear seen in the behavior of the black curve in Fig. 6.5a during the critical region [83,84]. Inhibitor S can modulate the steady-state response of the signaling cycle by suppressing the amplitude of the value change of W^{*ss} during the critical region and increasing the rate of the value change of W^{*ss} after the critical region (see Fig. 6.5a). The investigations shown here can help us understand why signaling cycle can function as the pivot where the interaction of multiple signaling pathways happens (e.g., the interaction between 14-3-3-NFAT pathway and calcineurin-NFAT pathway takes place through the signaling cycle shown in Fig. 6.4b. The interaction between the BMK1/ERK5[26] signaling pathway and calcineurin-MCIP pathway happens through the $MCIP^P$ signaling cycle formed by Reactions 10 and 11 in Table 4.1). It is known that three simple systems (activator-inhibitor system, substrate-deplete system and delayed negative feedback system) containing a signaling cycle can generate oscillating behavior [213]. We will further investigate the modulating effect on the oscillating behavior of these systems after adding an inhibitor to the signaling cycle in these systems.

In this Chapter, we gave a concise summary of the functions of various network motifs in cellular networks and enumerated those found in metal ion hoemoestasis and signaling systems. Particularly, we used simulation results of an ODE model to show the modulation effect on the properties of the signaling cycle motif by an inhibitor. In Chappter 7, we will summarize the thesis, do some final discussions and indicate the future work.

[26] ERK5 is a synonym of BMK1 [95].

Chapter 7 Final Discussion and Future Work

The modeling work presented in this thesis is done for metal ion homeostasis and signaling systems in various organisms, including both prokaryotes (e.g., *E. coli*) and eukaryotes (yeast, mice). More specifically, Chapter 2 and 3 are about yeast calcium homeostasis and signaling, Chapter 4 is about complex calcium signaling network in cardiac myocytes in mice, Chapter 5 is related to zinc homeostasis system in *E. coli* and Chapter 6 is about the general design principles of these metal ion homeostasis and signaling networks.

The work demonstrated in Chapter 2 and 3 shows that yeast has both fast feedback pathway (i.e., the quick inhibition on the influx transporters possibly by calmodulin, see the dashed lines in Fig. 3.1B) responsible for the short-term calcium response and slow feedback pathway (i.e., the calcineurin-dependent feedback pathway, see Fig. 2.1C) to regulate the long term calcium homeostasis. This finding in yeast cell is consistent with the specific responsiveness of calcineurin to sustained, low frequency calcium signals as found in animal cells ([224], also see Section 4.2.3). In the short-term response, Vcx1 is the main transporter responsible for rapidly sequestering cytosolic calcium (please compare Fig. 3.2B with Fig. 3.2C) whereas in the long-term calcium homeostasis, Pmc1 becomes the most critical transporter because calcineurin is activated to increase the expression of *PMC1* and *PMR1* and inhibit the activity of Vcx1.

As mentioned in Section 1.3.4.6, Scrase-Field *et al.* (2003) ever proposed that calcium may work merely as an essential chemical switch rather than an encoder of signal specifity as the calcium signature hypothesis assumes [189]. Their arguments for the calcium switch proposal include experimentally found phenomena in plant calcium signaling such as similar calcium signaures with different end reponses, similar end responses with different calcium signatures. For example, osmotic shock and salt shock induce very similar calcium signatures within both the cell and the whole plant. If calcium signature hypothsis is right, these two stimuli should induce the same end responses. However, the calcium signature induced by non-ionic osmotic shock does not induce the SOS3-SOS2-SOS1[27] complex as the signature induced by salt stress does [189].

Similar phenomena are also experimentally found in yeast cells. For example, Wiesenberger *et al.* (2007) reported that Mg^{2+} starvation and Ca^{2+} stress can induce very similar cytosolic calcium transients in yeast (this is also confirmed by our simulations, see Section 3.3.2.4) and a striking portion of genes including *ENA1* (encoding a P-type ATPase sodium pump) and *PHO89* (encoding a sodium/phosphate cotransporter) up-regulated under Mg^{2+} depletion are also induced by Ca^{2+} stress. However, lots of other genes (e.g., SUL1, ARA1, MDH2, STF2) up-regulated under Mg^{2+} depletion are not induced by Ca^{2+} stress [234].

---

[27] In response to the salt shock, both SOS3 and SOS2 are important in stimulating the plasma membrane Na^+/H^+ exchange activity of SOS1. SOS3: Salt Overly Sensitivity3.

As stated in Section 1.3.4.6 and also above, both calcium signature hypothesis and chemical switch seem to have their respective supporting experimental evidence. Thus it will be quite important to discriminate the cases in which calcium is responsible for signal specificity with those in which it only functions as a switch. From the viewpoint that the end response is usually the result of the cross-interaction of multiple signaling pathways, we can understand more easily why the signal specificity can be encoded by signaling components other than calcium. Actually our work presented in Chapter 4 shows an example of how different stimuli can cause their respective end response through the complex cross-interaction of different signaling pathways (e.g., PO induces cardiac hypertrophy by activating both the calcium-calcineruin-NFAT pathway and the BMK1/ERK5 signaling pathway [95] whereas the BMK1/ERK5 signaling pathway is not activated in the case of CaN^{*} overexpression). The eventual accurate mathematical approximation of the calcium signaling systems will help us uncover the mystery of encoding signal specificity.

On one hand, the quantitative agreement of our simulation results with the corresponding experimental data (e.g., compare Fig. 3.4A-B with Fig. 3.2B-C; also see Fig. 5.2, Fig. 5.3d, Fig. 5.9) and the ability of our models of predicting certain mutant behavior (e.g., see Fig. 2.4a-b, Fig. 3.4B, Fig. 4.2b) show the usefulness of mathematical modeling. On the other hand, we need to realize that to accurately approximate the studied systems, lots of work remain to be done. Many missing components of the relevant networks need to be identified, a number of rate parameters need to determined and the exact *in vivo* concentrations of many relevant proteins need to be quantified, which illustrates the great challenges imposed by systems biology (see Section 1.1.3). Close cooperation between biologists and computational scientists through iterative procedure of systems biology (experiment→model→experiment) is necessary for devising realistic models (see Section 1.2.1) [72]. The work presented in Chapter 3 gives an example showing effective cooperation between biologists and modelers indeed can help detect the existence of new components of the metal ion homeostasis and signaling networks and to push forward our understanding of these complex systems.

Compared with those systems in more complicated organisms such as mice and human, metal ion homeostasis and signaling systems in simpler organisms (e.g., yeast and *E. coli*) are easier to approximate. As shown in Chapter 2 and 3, yeast cell (*Saccharomyces cerevisiae*) has an elaborate calcium homeostasis/signaling system whose components (except the H^{+}/Ca^{2+} antiporter) have corresponding homologues in animal cells (see Table 1.3). Surprisingly, most of the these factors operate similarly in human cells, for example, NFAT translocation in human cells is strikingly similar as Crz1 translocation in yeast [208], MCIP signaling in human cells is similar as Rcn1 signaling in yeast [100,116]. Thus the understanding of calcium homeostasis/signaling system in the budding yeast *Saccharomyces cerevisiae*, a simple organism that affords powerful genetic and genomic tools, can be a shortcut to help understand calcium homeostasis/signaling systems in human and treat relevant human diseases such as pathological cardiac hypertrophy and heart failure.

In order to gain a more complete understanding of calcium homeostasis/signaling system in *S. cerevisiae* as shown in Fig. 3.1A, the first critical thing is that we need to identify the missing components of the network. Genome-wide high-throughput screens and comparative genomics can be helpful for locating the possible candidates [40,76,81]. Recently, proteomics has developed into such stage that it can determine the cellular response to any perturbation at the level of protein activation (e.g, phosphorylation) [3,45,54,121,160]. Thus mass-spectrometry-based proteomics can be a very powerful technique for searching the missing components and for detecting and determining the protein interactions as well. Moreover, the theory of network motifs may help determine the local network structure. The second critical thing is that we need to quantify the concentrations of proteins and measure the rate constants. Again, the former task can be achieved by mass-spectrometry-based proteomics [45,54]. In order to measure the rate constants, various existent methods (e.g., surface plasmon resonance analysis [171]) can be used. The third critical thing is that we need to accurately approximate the electrophysiological properties of ion channels (e.g., Cch1-Mid1 [48,132]). Electrophysiological recordings of ion channels in the plasma membrane of live yeast cells have been proven to be quite difficult [174]. An alternative way to achieve such task is to express the corresponding genes into mammalian cells where electrophysiological recordings become much easier. Finally, mass-spectrometry-based proteomics can also be used to measure the nucleocytoplasmic transport of relevant proteins (e.g., Crz1 and calcineurin) [161,216]. As mentioned before, the greatest advantages of yeast are that this simple unicellular organism is so small that certain spatial effects (e.g. diffusion) can be neglected and that it affords powerful genetic and genomic tools as well. As shown in Chapter 2 and 3, functional assays based on gene-knockout techniques provide powerful check for the validity of the models [99]. Effective collaborations among scietists who are proficient in genetics, proteomics and computational science via high-throughput experimental and computational methods will not only result in the eventual completion of the whole yeast calcium homeostasis/signaling system and the understanding of its dynamics in the near future, but also help push forward our understanding of the calcium homeostasis/signaling systems in all other organisms.

In order to further our understanding of the zinc homeostasis in *E. coli*, the most critical thing is to identify the intracellular zinc chaperone which is very likely to exist (see the second last paragraph in Section 5.4). Again, mass-spectrometry-based proteomics and genome-wide high-throughput screens can be used to search the possible candidates. Once the zinc chaperone is identified, the next step will be to measure the interactions between the zinc chaperone and the membrane transport proteins (ZnuABC, ZupT, ZntA and ZitB) and the interactions between the zinc chaperone and the metalloregulatory proteins (ZntR and Zur). Since similar work has been done already for the copper homeostasis system in *E. hirae* [202], the same technical equipments and methods used there (e.g., surface plasmon resonance analysis [171]) can be used to measure the kinetics of these interactions. Then we need to further take into consideration the zinc storage and zinc using proteins in the *E. coli* cell and quantify the concentrations of the relevant proteins, DNAs and mRNAs. Finally, the subtle details of relevant regulations (e.g., proteolysis which has been proven to play a role [172]) need to be further investigated. In this way, step by step we will acquire a complete map of the zinc homeostasis system in

E. coli and the full understanding of its dynamics.

As mentioned before, all the models presented in this thesis are represented in nonlinear ODEs which ignore the spatial effects and stochastic effects of biological events (see Section 1.2.2) [69]. In some cases when the stochastic effects are not negligible, stochastic simulation methods are needed. For example, Monte Carlo simulation methods have been used to simulate the stochastic gating of ion channels which can be expressed as an ensemble of Markov processes [69,197]. In some other cases when the spatial effects are important, partial differential equations become more amenable tool for approximating biological systems [65,151]. For example, PDE models are necessary to capture the spatial effects of calcium signaling such as calcium sparks and waves in animal cells [69,71,197]. Moreover, to simulate complex calcium signaling events as those in embryogenesis (see Fig. 1.3), multi-scale modeling based on PDE modeling becomes inevitable (see Section 1.2.3). For example, if we want to build a comprehensive model for simulating the hypertrophic growth of mammalian heart in response to certain hypertrophic stimuli such as pressure overload, we need to extend the intracellular calcium signaling model presented in Chapter 4 to an organ-level model and then couple it with a spatial growth model of heart. Finally, calcium signaling has been proven to happen within nanodomain of calcium sources [129]. In order to capture the subtle details of these nanodomain signaling events, particle-based modeling techniques such as molecular dynamics become inevitable [75,187]. In the past decades, molecular dynamics methods have been used to simulate the gating of ion channels and help gain important insights into the underlying mechanisms [19]. In these cases, more computational power is usually demanded and special techniques (including new mathematics and new computational methodologies) need to be developed to tackle great difficulties such as the highly irregular boundaries.

References:

1. S. Abbasi, J.D. Lee, B. Su, X. Chen, J.L. Alcon, J. Yang, R.E. Kellems and Y. Xia, Protein kinase-mediated regulation of calcineurin through the phosphorylation of modulatory calcineurin-interacting protein 1*, J. Biol. Chem.* 281: 7717–7726, (2006).
2. L. Abelovska, M. Bujdos, J. Kubova, S. Petrezselyova, J. Nosek, L. Tomaska, Comparison of element levels in minimal and complex yeast media, *Canadian Journal of Microbiology* 53: 533-535, (2007).
3. R. Aebersold and M. Mann, Mass spectrometry-based proteomics, *Nature* 422: 198-207, (2003).
4. D.P. Aiello, L. Fu, A. Miseta, D.M. Bedwell, Intracellular glucose 1-phosphate and glucose 6-phosphate levels modulate Ca^{2+} homeostasis in *Saccharomyces cerevisiae*, *J. Biol. Chem.* 277: 45751-45758, (2002).
5. B. Alberts, A. Johnson, J. Lewis, M. Raff, K. Roberts, P. Walter, Molecular biology of the cell, Garland Publishing, Inc., New York, 2002.
6. D. Allemand, C. Ferrier-Pagès, F. Furla, F. Houlbrèque, S. Puverel, S. Reynaud, É. Tambutté, S. Tambutté and D. Zoccola, Biomineralisation in reef-building corals: from molecular mechanisms to environmental control, *C. R. Palevol* 3: 453-467, (2004).
7. D.G. Allen, J.R. Blinks, F.G. Prendergast, Aequorin luminescence: relation of light emission to calcium concentration - a calcium-independent component, *Science* 195: 996-998, (1977).
8. G.J. Allen, S.P. Chu, C.L. Harrington, K. Schumacher, T. Hoffmann, Y.Y. Tang, E. Grill & J.I. Schroeder, A defined range of guard cell calcium oscillation parameters encodes stomatal movements**,** *Nature* 411: 1053-1057, (2001).
9. G.J. Allen, S.P. Chu, K. Schumacher, C.T. Shimazaki, D. Vafeados, A. Kemper, S.D. Hawke, G. Tallman, R.Y. Tsien, J.F. Harper, J. Chory, and J.I. Schroeder, Alteration of stimulus-specific guard cell calcium oscillations and stomatal closing in *Arabidopsis* det3 mutant, *Science* 289: 2338–2342, (2000).
10. U. Alon, An introduction to systems biology: design principles of biological circuits, CRC Press, 2007.
11. U. Alon, Network motifs: theory and experimental approaches, *Nature Reviews Genetics* 8: 450-461, (2007).
12. A. Anton, A. Weltrowski, C.J. Haney, S. Franke, G. Grass, C. Rensing and D.H. Nies, Characteristics of zinc transport by two bacterial cation diffusion facilitators from *Ralstonia metallidurans* CH34 and *Escherichia coli*, *J. Bacteriol.* 186: 7499-7507, (2004).
13. C.L. Antos, T.A. McKinsey, N. Frey, W. Kutschke, J. McAnally, J.M. Shelton, J.A. Richardson, J.A. Hill and E.N. Olson, Activated glycogen synthase-3β suppresses cardiac hypertrophy *in vivo*, *Proc. Natl. Acad. Sci. USA* 99: 907–912, (2002).
14. C. H. Arnaud, Systems biology's clinical future, *Chemical and engineering news*, 84: 17-26, (2006).
15. J.R. Arron, M.M. Winslow, A. Polleri, C.P. Chang, H. Wu, X. Gao, J.R. Neilson, L. Chen, J.J. Heit, S.K. Kim, N. Yamasaki, T. Miyakawa, U. Francke, I.A. Graef

and G.R. Crabtree, NFAT dysregulation by increased dosage of DSCR1 and DYRK1A on chromosome 21, *Nature* 441: 595–600, (2006).
16. N. Barkai and S. Leibler, Robustness in simple biochemical networks, *Nature* 387: 913-917, (1997).
17. A.F. Batiza, T. Schulz, P.H. Masson, Yeast respond to hypotonic shock with a calcium pulse, *J. Biol. Chem.* 271: 23357-23362, (1996).
18. S.J. Beard, R. Hashim, J. Membrillo-Hernandez, M.N. Hughes and R.K. Poole, Zinc(II) tolerance in *Escherichia coli* K-12: evidence that the zntA gene (o732) encodes a cation transport ATPase, *Mol. Microbiol.* 25: 883-891, (1997).
19. O. Beckstein, P.C. Biggin, P. Bond, J.N. Bright, C. Domene and A. Grottesi *et al.*, Ion channel gating: insights via molecular simulations, *FEBS Letters* 555: 85-90, (2003).
20. M.J. Berridge, M.D. Bootman and P. Lipp, Calcium - a life and death signal, *Nature* 395: 645-648, (1998).
21. M.J. Berridge, M.D. Bootman and H.L. Roderick, Calcium signaling: dynamics, homeostasis and remodeling, *Nature Reviews Molecular Cell Biology* 4: 517-529, (2003).
22. M.J. Berridge, P. Lipp and M.D. Bootman, The versatility and universality of calcium signaling, *Nature Reviews Molecular Cell Biology* 1: 11-21, (2000).
23. H.-G. Beyer, Toward a Theory of Evolution Strategies: Self-Adaptation, *Evolutionary Computation* 3: 311–347, (1996).
24. U.S. Bhalla and R. Iyengar, Emergent properties of networks of biological signaling pathways, *Science* 203: 381–387, (1999).
25. A.J. Bird, H. Zhao, H. Luo, L.T. Jensen, C. Srinivasan, M. Evans-Galea, D.R. Winge and D.J. Eide, A dual role for zinc fingers in both DNA binding and zinc sensing by the Zap1 transcriptional activator, *EMBO J.* 19: 3704–3713, (2000).
26. D.K. Blencowe and A.P. Morby, Zn(II) metabolism in prokaryotes, *FEMS Microbiol. Rev.* 27: 291-311, (2003).
27. M. Bonilla and K.W. Cunningham, Calcium release and influx in yeast: TRPC and VGCC rule another kingdom, *Science's STKE* 127: pe17, (2002).
28. M. Bonilla and K.W. Cunningham, MAP kinase stimulation of Ca^{2+} signaling is required for survival of endoplasmic reticulum stress in yeast, *Mol. Biol. Cell* 14: 4296–4305, (2003).
29. L.M. Boustany, M.S. Cyert, Calcineurin-dependent regulation of Crz1 nuclear export requires Msn5p and a conserved calcineurin docking site, *Genes & Dev.* 16: 608-619, (2002).
30. J.M. Bower and H. Bolouri, Computational modeling of genetic and biochemical networks, MIT Press, 2001.
31. R. Bozym, R. Thompson, A. Stoddard, C. Fierke, Measuring picomolar intracellular exchangeable zinc in PC-12 cells using a ratiometric fluorescence biosensor, *ACS Chem. Biol.* 1: 103–111, (2006).
32. O. Brandman, J.E. Ferrell, R. Li, T. Meyer, Interlinked Fast and Slow Positive Feedback Loops Drive Reliable Cell Decisions, *Science* 310: 496 – 498, (2005).
33. K.R. Brocklehurst, J.L. Hobman, B. Lawley, L. Blank, S.J. Marshall, N.L. Brown and A.P. Morby**,** ZntR is a Zn(II)-responsive MerR-like transcriptional regulator of zntA in *Escherichia coli*, *Mol. Microbiol.* 31: 893-902, (1999).

34. C. Brownie, Plant signaling: calcium first and second, *Current biology* 13: R923-R924, (2003).
35. F.J. Bruggeman and H.V. Westerhoff, The nature of systems biology, *Trends in Microbiology* 15: 45-50, (2007).
36. R. Bundschuh, F. Hayot and C. Jayaprakash, The role of dimerization in noise reduction of simple genetic networks, *J. Theor. Biol.* 220: 261-269, (2003).
37. A.M. Campbell and L.J. Heyer, Discovering genomics, proteomics, and bioinformatics, Pearson Education Inc., 2007.
38. W.B. Cannon, Wisdom of the body, Peter Smith Pub Inc, Rev. and Enl. Ed edition, 1963.
39. E. Carafoli, Calcium signaling: a tale for all seasons, *Proc. Natl. Acad. Sci. USA* 99: 1115–1122, (2000).
40. A.E. Carpenter and D.M. Sabatini, Systematic genome-wide screens of gene function, *Nat. Rev. Genet.* 5: 11-22, (2004).
41. Y. Chao and D. Fu, Kinetic study of the antiport mechanism of an *Escherichia coli* zinc transporter, ZitB, *J. Biol. Chem*. 279: 12043-50, (2004).
42. P.T. Chivers, A Galvanizing Story—Protein Stability and Zinc Homeostasis, *J. Bacteriol.* 189: 2953-2954, (2007).
43. R.A. Colvin, C.P. Fontaine, M. Laskowski and D. Thomas, Zn^{2+} transporters and Zn^{2+} homeostasis in neurons, *Eur. J. Pharmacol.* 479: 171–185, (2003).
44. S. Cooper, What is the bacterial growth law during the division cycle? *J. Bacteriology* 170: 5001-5005, (1988).
45. J. Cox and M. Mann, Is proteomics the new genomics? *Cell* 130 (2007) 395 – 398.
46. G.R. Crabtree, Calcium, calcineurin and the control of transcription, *J. Biol. Chem.* 276: 2313-2316, (2001).
47. S.R. Cronin, R. Rao, R.Y. Hampton, Cod1p/Spf1p is a P-type ATPase involved in ER function and Ca^{2+} homeostasis, *J. Cell Biol.* 157: 1017-1028, (2002).
48. P. Csutora, Z. Su, H.Y. Kim, A. Bugrim, K. W. Cunningham, R. Nuccitelli, J. E. Keizer, M. R. Hanley, J. E. Blalock, R. B. Marchase, Calcium influx factor is synthesized by yeast and mammalian cells depleted of organellar calcium stores. *Proc. Natl. Acad. Sci., USA* 96: 121-126, (1999).
49. K.W. Cunningham, Calcium signaling and homeostasis determined by genome-wide functional networking in yeast, Presentation slides on ISNB2006: Third International Symposium on Networks in Bioinformatics, Amsterdam, 2006.
50. K.W. Cunningham, G.R. Fink, Calcineurin-dependent growth control in *Saccharomyces cerevisiae* mutants lacking *PMC1*, a homolog of plasma membrane Ca^{2+} ATPases, *J. Cell Biol.* 124: 351-363, (1994).
51. K.W. Cunningham, G.R. Fink, Calcineurin inhibits *VCX1*-dependent H^+/Ca^{2+} exchange and induces Ca^{2+} ATPases in *Saccharomyces cerevisiae*, *Mol. Cell. Biol.* 16: 2226-2237, (1996).
52. K.W. Cunningham, G.R. Fink, Ca^{2+} transport in *Sacchromyces cerevisiae*, *J. Exp. Biol.* 196: 157-166, (1994).
53. M.S. Cyert, Genetic analysis of calmodulin and its targets in *Sacchromyces cerevisiae*, *Annu. Rev. Genet.* 35: 647-672, (2001).

54. L.M. de Godoy, J.V. Olsen, G.A. de Souza, G. Li, P. Mortensen and M. Mann, Status of complete proteome analysis by mass spectrometry: SILAC labeled yeast as a model system, *Genome Biology* 7: R50, (2006).
55. V. De Lorenzo, M. Herrero, F. Giovannini and J.B. Neilands, Fur ferric uptake regulation protein and CAP catabolite-activator protein modulate transcription of *fur* gene in *Escherichia coli*, *Eur. J. Biochem.* 173: 537–546, (1988).
56. I.M. De Maran˜ón, P. Gervais, Determination of cells' water membrane permeability: unexpected high osmotic permeability of *Saccharomyces cerevisiae. Biotechnol. Bioeng.* 56: 62-70, (1997).
57. G.W. De Young and J. Keizer, A single-pool inositol 1,4,5-triphosphate-receptor-based model for agonist-stimulated oscillations in Ca^{2+} concentration, *Proc. Natl. Acad. Sci. USA* 89: 9895-9899, (1992).
58. M. Dixon, Enzymes, Longman Group Limited London, Third edition, 1979.
59. R.E. Dolmetsch, R.S. Lewis, C.C. Goodnow and J.I. Healy, Differential activation of transcription factors induced by Ca^{2+} response amplitude and duration, *Nature* 386: 855 – 858, (1997).
60. D.C. Dominguez, Calcium signalling in bacteria, *Molecular Microbiology* 54: 291-297, (2004).
61. J. Doyle, B. Francis and A. Tannenbaum, Feedback control theory, Macmillan Publishing Co., 1990.
62. N. Dubi, L. Gheber, D. Fishman, I. Sekler and M. Hershfinkel, Extracellular zinc and zinc-citrate, acting through a putative zinc sensing receptor, regulate growth and survival of prostate cancer cells, *Carcinogenesis* 29: 1692-1700, (2008).
63. T. Dunn, K. Gable, T. Beeler, Regulation of cellular Ca^{2+} by yeast vacuoles, *J. Biol. Chem.* 269: 7273-7278, (1994).
64. J.A. Easton, P.Thompson and M.W. Crowder, Time-dependent translational response to *E. coli* to excess Zn(II), *J. Biomol. Tech.* 17: 303-307, (2006).
65. L. Edelstein-Keshet, Mathematical models in biology, Random House, Inc., 1988.
66. D.J. Eide, Zinc transporters and the cellular trafficking of zinc, *Biochimica et Biophysica Acta* 1763: 711-722, (2006).
67. S.P. Ellner and J. Guckenheimer, Dynamic models in biology, Princeton University Press, 2006.
68. H. El-Samad, J.P. Goff and M. Khammash, Calcium Homeostasis and Parturient Hypocalcemia: An Integral Feedback Perspective, *J. theor. Biol.* 214: 17-29, (2002).
69. C. P. Fall, E.S. Marland, J.M. Wagner and J.J. Tyson (Editors), Computational cell biology, Springer-Verlag New York, Inc., 2002.
70. A. Fersht, Enzyme structure and mechanism, W. H. Freeman and Company, 1985.
71. C.C. Fink, B. Slepchenko, I.I. Moraru, J. Watras, J.C. Schaff, and L.M. Loew, An image-based model of calcium waves in differentiated neuroblastoma cells, *Biophys. J.* 79: 163 – 183, (2000).
72. A. Finkelstein, J. Hetherington, L. Li, O. Margoninski, P. Saffrey, R. Seymour and A. Warner, Computational challenges of systems biology*, Computer* 37: 26-33, (2004).
73. N. Forbes, Imitation of life: How biology is inspiring computing, The MIT Press, 2004.

74. M. Freeman, Feedback control of intercellular signalling in development. *Nature* 408: 313–319, (2000).
75. D. Frenkel and B. Smit, Understanding Molecular Simulation, Academic Press, 2nd edition, 2001.
76. A. Friedman and N. Perrimon, Genome-wide high-throughput screens in functional genomics, *Curr. Opin. Genet. Dev.* 14: 470-476, (2004).
77. L.A. Gaither and D.J. Eide, Eukaryotic zinc transporters and their regulation, *Biometals* 14: 251–270, (2001).
78. K. R. Gee, Z. -L. Zhou, D. Ton-That, S. L. Sensi and J. H. Weiss, Measuring zinc in living cells. A new generation of sensitive and selective fluorescent probes, *Cell Calcium* 31: 245-251, (2002).
79. P. Gennemark, B. Nordlander, S. Hohmann, D. Wedelin, A simple mathematical model of adaptation to high osmolarity in yeast. *In Silico Biol*. 6: 193-214, (2006).
80. N. Gershenfeld, The nature of mathematical modeling, Cambridge University Press, 1998.
81. Giaever *et al.*, Functional profiling of the Saccharomyces cerevisiae genome, *Nature* 418: 387-391, (2002).
82. A. Goldbeter, Biochemical oscillations and cellular rhythms, Cambridge University Press, Cambridge, 1996.
83. A. Goldbeter and D.E. Koshland, An amplified sensitivity arising from covalent modification in biological systems, *Proc. Natl. Acad. Sci. USA*. 78: 6840–6844, (1981).
84. C. Gomez-Uribe, G.C. Verghese and L.A. Mirny, Operating regimes of signaling cycles: statics, dynamics and noise filtering, *Plos Computational Biology* 3: 2487-2497, (2007).
85. G. Grass, B. Fan, B.P. Rosen, S. Franke, D.H. Nies, C. Rensing, ZitB (YbgR), a Member of the Cation Diffusion Facilitator Family, Is an Additional Zinc Transporter in *Escherichia coli*, *J. Bacteriol.* 183: 4664-4667, (2001).
86. G. Grass, S. Franke, N. Taudte, D.H. Nies, L.M. Kucharski, M.E. Maguire and C. Rensing, The metal permease ZupT from *Escherichia coli* is a transporter with a broad substrate spectrum, *J. Bacteriol.* 187: 1604-1611, (2005).
87. G. Grass, M.D. Wong, B.P. Rosen, R.L. Smith and C. Rensing**,** ZupT is a Zn(II) uptake system in *Escherichia coli*. *J. Bacteriol.* 184: 864-866, (2002).
88. S.S. Gupta, V-K Ton, V. Beaudry, S. Rulli, K.W. Cunningham, and R. Rao**,** Antifungal activity of amiodarone is mediated by disruption of calcium homeostasis, *J. Biol. Chem.* 278: 28831-28839, (2003).
89. D. Halachmi, Y. Eilam, Calcium homeostasis in yeast cells exposed to high concentrations of calcium: Roles of vacuolar H^+-ATPase and cellular ATP, *FEBS Lett.* 316: 73-78, (1993).
90. D. Halachmi, Y. Eilam, Elevated cytosolic free Ca^{2+} concentrations and massive Ca^{2+} accumulation within vacuoles, in yeast mutant lacking *PMR1*, a homolog of Ca^{2+}-ATPase, *FEBS Lett.* 392: 194-200, (1996).
91. M. Hallhuber, N. Burkard, R. Wu, M.H. Buch, S. Engelhardt, L. Hein, L. Neyses, K. Schuh, and O. Ritter, Inhibition of nuclear import of calcineurin prevents myocardial hypertrophy**,** *Circ. Res.* 99: 626 – 635, (2006).

92. K. Hantke, Bacterial zinc transporters and regulators. *Biometals* 14: 239-249, (2001).
93. D.G. Hardie, Biochemical messengers, Chapman and Hall, London, 1991.
94. J.F. Harper and A. Harmon, Plants, symbiosis and parasites: a calcium signaling connection, *Nature Reviews Molecular Cell Biology* 6: 555-566, (2005).
95. M. Hayashi and J.D. Lee, Role of the BMK1/ERK5 signaling pathway: lessons from knockout mice, *J. Mol. Med.* 82: 800-808, (2004).
96. F. Hayot, C. Jayaprakash, A feedforward loop motif in transcriptional regulation: induction and repression, *J. Theor. Biol.* 234: 133-143 (2005).
97. M. Hershfinkel, W.F. Silverman and Israel Sekler, The zinc sensing receptor, a link between zinc and cell signaling, *Mol. Med.* 13: 331–336, (2007).
98. A.M. Hetherington and C. Brownlee, The generation of Ca^{2+} signals in plants, *Ann. Rev. Plant Biol.* 55: 401-427, (2004).
99. P.R. Hiesinger and B.A. Hassan, Genetics in the age of systems biology, *Cell* 123: 1173-1174, (2005).
100. Z. Hilioti, D.A. Gallagher, S.T. Low-Nam, P. Ramaswamy, P. Gajer, T.J. Kingsbury, C.J. Birchwood, A. Levchenko and K.W. Cunningham, GSK-3 kinases enhance calcineurin signaling by phosphorylation of RCNs, *Genes & Dev.* 18: 35 – 47, (2004).
101. J.A. Hill, B.A. Rothermel, K.D. Yoo *et al.*, Targeted inhibition of calcineurin in pressure-overload cardiac hypertropy: preservation of systolic function, *J. Biol. Chem.* 277: 10251-10255, (2002).
102. M. Hiromura and H. Sakurai, Intracellular metal transport proteins, *RIKEN Review* No. 35: 23-25, (2001).
103. Y. Hitomi, C.E. Outten and T.V. O'Halloran, Extreme zinc-binding thermodynamics of the metal sensor/regulator protein, ZntR, *J. Am. Chem. Soc.* 123: 8614-8615, (2001).
104. J.L. Hobman, J. Wilkie, and N.L. Brown**,** A design for life: prokaryotic metal-binding MerR family regulators. *Biometals* 18: 429-436, (2005).
105. A. Hodgkin and A. Huxley, A quantitative description of membrane current and its application to conduction and excitation in nerve, *J. Physiology* 117: 500-544, (1952).
106. A.M. Hofer and E.M. Brown, Extracellular calcium sensing and signaling, *Nature Reviews Molecular Cell Biology* 4: 530-538, (2003).
107. T. Ideker, T. Galitski and L. Hood, A new approach to decoding life: systems biology**,** *Annual Review of Genomics and Human Genetics* 2: 343-372, (2001).
108. H. Iida, Y. Yagawa and Y. Anraku, Essential role for induced Ca^{2+} influx followed by $[Ca^{2+}]_i$ rise in maintaining viability of yeast cells late in the mating pheromone response pathway, *J. Biol. Chem.* 265: 13391–13399, (1990).
109. P.J. Ingram, M.P.H. Stumpf, J. Stark, Network motifs: structure does not determine function**,** *BMC Genomics* 7: 108-119, (2006).
110. U. Jenal, U. and R. Hengge-Aronis, Regulation by proteolysis in bacterial cells, *Curr. Opin. Microbiol.* 6: 163-172, (2003).
111. T.K. Jingsbury, K.W. Cunningham, A conserved family of calcineurin regulators, *Genes & Dev.* 14: 1595-1604, (2000).

112. J.A. Kaandorp, C. Lowe, D. Frenkel and P.M.A. Sloot, The effect of nutrient diffusion and flow on coral morphology, *Phys. Rev. Lett.* 77: 2328—2331, (1996).
113. D. Kaplan and L. Glass, Understanding nonlinear dynamics, Springer-Verslag New York, Inc., 1995.
114. D. Kim, Y.-K. Kwon and K.-H. Cho, Coupled positive and negative feedback circuits form an essential building block of cellular signaling pathways, *BioEssays* 29: 85-90, (2006).
115. J.-R. Kim, Y. Yoon and K.-H. Cho, Coupled feedback loops form dynamic motifs of cellular networks, *Biophysical Journal* 94: 359-365, (2008).
116. T.K. Kingsbury, K.W. Cunningham, A conserved family of calcineurin regulators, *Genes & Dev.* 14: 1595-1604, (2000).
117. Y. Kirichok, G. Krapivinsky and D.E. Clapham, The mitochondrial calcium uniporter is a highly selective ion channel, *Nature* 427: 360-364, (2004).
118. H. Kitano, Computational systems biology, *Nature* 420: 206-210, (2002).
119. H. Kitano, Systems biology : a brief overview, *Nature* 295: 1662-1664, (2002).
120. B. Kofahl and E. Klipp, Modeling the dynamics of the yeast pheromone pathway, *Yeast* 21: 831-850, (2004).
121. M. Krüger, I. Kratchmarova, B. Blagoev, Y.-H. Tseng, C.R. Kahn and M. Mann, Dissection of the insulin signaling pathway via quantitative phosphoproteomics, *Proc. Natl. Acad. Sci. USA* 105: 2451-2456, (2008).
122. A.D. Lander, A calculus of purpose, *PloS Biology* 2: 712-714, (2004).
123. W.J. Langston and M.J. Bebianno, Metal metabolism in aquatic environments, Chapman & Hall, London, 1998.
124. D. Lecourieux, R. Ranjeva and A. Pugin, Calcium in plant defence-signalling pathways, *New Phytologist* 171: 249-269, (2006).
125. L.J. Lee, J.A. Barrett and R.K. Poole, Genome-wide transcriptional response of chemostat-cultured *Escherichia coli* to zinc, *J. Bacteriol*. 187: 1124 – 1134, (2005).
126. I.B. Levitan and L.K. Kaczmarek, The neuron: cell and molecular biology, Oxford University Press, Oxford, 1997.
127. F.L. Lewis, Applied optimal control and estimation, Prentice-Hall, 1992.
128. W.H. Li, J. Llopis, M. Whitney, G. Zlokarnik, and R.Y. Tsien, Cell-permeant caged $InsP_3$ ester shows that Ca^{2+} spike frequency can optimise gene expression. *Nature* 392: 936-941, (1998).
129. H. Liang, C.D. DeMaria, M.G. Erickson, M.X. Mori, B.A. Alseikhan, and D.T. Yue, Unified mechanisms of Ca^{2+} regulation across the Ca^{2+} channel family, *Neuron* 39: 951-960, (2003).
130. W. Liao, S. Wang, C. Han and Y. Zhang, 14-3-3 Proteins regulate glycogen synthase 3β phosphorylation and inhibit cardiomyocyte hypertrophy. *FEBS Journal* 272: 1845-1854, (2005).
131. C.M. Lloyd, M.D.B. Halstead and P.F. Nielsen, CellML: its future, present and past. *Progress in Biophysics & Molecular Biology* 85: 433–450, (2004).

132. E.G. Locke, L. Liang, M. Bonilla, Y. Takita, K.W. Cunningham, A homolog of voltage-gated channels stimulated by depletion of Ca^{2+} secretory pools in yeast, *Mol. Cell. Biol.* 20: 6686-6694, (2000).
133. C.W. MacDiarmid, L.A. Gaither and David Eide, Zinc transporters that regulate vacuolar zinc storage in *Saccharomyces cerevisiae*, *EMBO J.* 19: 2845–2855, (2000).
134. C.W. MacDiarmid and R.C. Gardner, Overexpression of the *Saccharomyces cerevisiae* magnesium transport system confers resistance to aluminum ion, *J. Biol. Chem.* 273: 1727–1732, (1998).
135. C.W. MacDiarmid, M.A. Milanick, D.J. Eide, Biochemical properties of vacuolar zinc transport systems of *Saccharomyces cerevisiae*, *J. Biol. Chem.* 277: 39187-39194, (2002).
136. L. Mackenzie, H.L. Roderick, M.J. Berridge, S.J. Conway and M.D. Bootman, The spatial pattern of atrial cardiomyocyte calcium signalling modulates contraction, *Journal of Cell Science* 117: 6327-6337, (2004).
137. D. Magnani and M. Solioz, How bacteria handle copper, In *Bacterial Transition Metal Homeostasis* (Nies, D. H., and Silver, S., eds.) Springer, Heidelberg, pp. 259-285, 2007.
138. F. Mammano, M. Bortolozzi, S. Ortolano and F. Anselmi, Ca^{2+} signaling in the inner ear, *Physiology* 22: 131-144, (2007).
139. M. Marhl, T. Haberichter, M. Brumen and R. Heinrich, Complex calcium oscillations and the role of mitochondria and cytosolic proteins, *Biosystems* 57: 75-86, (2000).
140. A.R. Marks, Calcium and the heart: a question of life and death, *J. Clin. Invest.* 111: 597–600, (2003).
141. V.Z. Marmarelis, Nonlinear dynamic modeling of physiological systems, IEEE, Inc., 2004.
142. Eric Massé and Mélina Arguin, Ironing out the problem: new mechanisms of iron homeostasis, *Trends in Biochem. Sci.* 30: 462-468, (2005).
143. E. McCormack, Y.-C. Tsai and J. Braam, Handling calcium signaling: Arabidopsis CaMs and CMLs, *Trends in Plant Science* 10: 383-389, (2005).
144. C. Miller, Ion channels: doing hard chemistry with hard ions, *Curr. Opin. Chem. Biol.* 4: 148-151, (2000).
145. A. Miseta, L. Fu, R. Kellermayer, J. Buckley, D.M. Bedwell, The Golgi Apparatus plays a significant role in the maintainance of Ca^{2+} homeostasis in the *vps33Δ* vacuolar biogenesis mutant of *Saccharomyces cerevisiae*, *J. Biol. Chem.* 274: 5939-5947, (1999).
146. A. Miseta, R. Kellermayer, D.P. Aiello, L. Fu, D.M. Bedwell, The vacuolar Ca^{2+}/H^{+} exchanger Vcx1p/Hum1p tightly controls cytosolic Ca^{2+} levels in *S. cerevisiae*, *FEBS Lett.* 451: 132-136, (1999).
147. C.G. Moles, P. Mendes and J.R. Banga, Parameter estimation in biochemical pathways: A comparison of global optimization methods. *Genome Res.* 13: 2467–2474, (2003).
148. J.D. Molkentin, J.R. Lu, C.L. Antos, B. Markham, J. Richardson, J. Robbins, S.R. Grant and E.N. Olson, A calcineurin-dependent transcriptional pathway for cardiac hypertrophy, *Cell* 93: 215–228, (1998).

149. C.M. Moore and J.D. Helmann, Metal ion homeostasis in *Bacillus subtilis*, *Curr. Opin. Microbiol.* 8: 188-95, (2005).
150. E. Muller, E.G. Locke, K.W. Cunningham, Differential regulation of two Ca^{2+} influx systems by pheromone signaling in *Saccharomyces cerevisiae*, *Genetics* 159: 1527-1538 (2001).
151. J.D. Murray, Mathematical biology, Springer-Verslag Berlin Heidelberg, 1993.
152. Y. F. Nanfack, J.A. Kaandorp and J.G. Blom, Efficient parameter estimation for spatio-temporal models of pattern formation: Case study of Drosophila melanogaster, *Bioinformatics* 23: 3356-3363, (2007).
153. M.C. Newman and A.W. McIntosh (editors), Metal Ecotoxicology: concepts and applications, Lewis Publishers, Inc., Chelsea, 1991.
154. J.G. Nicolls, A.R. Martin, B.G. Wallace, P.A. Fuchs, From neuron to brain, Sinauer Associates, Inc., Massachusetts, 2001.
155. D.H. Nies, How cells control zinc homeostasis, *Science* 317: 1695-1696, (2007).
156. D. Noble, From the Hodgkin-Huxley axon to the virtual heart**,** *J. Physiol.* 580: 15-22, (2007).
157. D. Noble, Modeling the heart: from genes to cells to the whole organ, *Science* 295: 1678-1682 (2002).
158. T.V. O'Halloran, B. Frantz, M.K. Shin, D.M. Ralston, J.G. Wright, The MerR heavy metal receptor mediates positive activation in a topologically novel transcription complex, *Cell* 56: 119-129, (1989).
159. Y. Ohsumi, Y. Ankaru, Calcium transport driven by a proton motive force in vacuolar membrane vesicles of *Saccharomyces cerevisiae*, *J. Biol. Chem.* 258: 5614-5617, (1983).
160. J.V. Olsen, B. Blagoev, F. Gnad, B. Macek, C. Kumar, P. Mortensen and M. Mann, Global, *in vivo*, and site-specific phosphorylation dynamics in signaling networks, *Cell* 127: 635-648, (2006).
161. H. Okamura, J. Aramburu, C. García-Rodríguez, *et al.* Concerted dephosphorylation of the transcription factor NFAT1 induces a conformational switch that regulates transcriptional activity, *Mol. Cell* 6: 539-550, (2000).
162. S. Orrenius, B. Zhivotovsky & P. Nicotera, Regulation of cell death: the calcium–apoptosis link, *Nature Reviews Molecular Cell Biology* 4: 552-565, (2003).
163. C.E. Outten and T.V. O'Halloran, Femtomolar sensitivity of metalloregulatory proteins controlling zinc homeostasis, *Science* 292: 2488 – 2492, (2001).
164. C.E. Outten, F.W. Outten, and T. V. O'Halloran, DNA distortion mechanism for transcriptional activation by ZntR, a Zn(II)-responsive MerR homologue in *Escherichia coli*, *J. Biol. Chem.* 274: 37517-37524, (1999).
165. C.P. Palmer, X. Zhou, J. Lin, S.H. Loukin, C. Kung, Y. Saimi, A TRP homolog in *Saccharomyces cerevisiae* forms an intracellular Ca^{2+}-permeable channel in the yeast vacuolar membrane, *Proc. Natl. Acad. Sci. USA* 98: 7801-7805, (2001).

166. B.O. Palsson, Systems biology: properties of reconstructed networks, Cambridge University Press, 2006.
167. S.I. Patzer and K. Hantke, The zinc-responsive regulator Zur and its control of the znu gene cluster encoding the ZnuABC zinc uptake system in *Escherichia coli*, *J. Biol. Chem.* 275: 24321-24332, (2000).
168. S.I. Patzer and K. Hantke, The ZnuABC high-affinity zinc uptake system and its regulator Zur in *Escherichia coli*, *Mol. Microbiol.* 28: 1199-1210, (1998).
169. O.H. Petersen, M. Michalak and A. Verkhratsky, Calcium signalling: past, present and future, *Cell Calcium* 38: 161–169, (2005).
170. C. Plieth, Calcium: just another regulator in the machinery of life? *Annals of Botany* 96: 1-8, (2005).
171. R. Portmann, D. Magnani, J.V. Stoyanov, A. Schmechel, G. Multhaup, and M. Solioz, Interaction kinetics of the copper-responsive CopY repressor with the cop promoter of *Enterococcus hirae*, *J. Biol. Inorg. Chem.* 9: 396-402, (2004).
172. M. Pruteanu, S.B. Neher, and T.A. Baker**,** Ligand-controlled proteolysis of the *Escherichia coli* transcriptional regulator ZntR, *J. Bacteriol.* 189: 3017-3025, (2007).
173. D. Pruyne, A. Legesse-Miller, L. Gao, Y. Dong, A. Bretscher, Mechanisms of polarized growth and organelle segregation in yeast, *Annu. Rev. Cell Dev. Biol.* 20: 559-591, (2004).
174. J.W. Putney (editor) Calcium signaling, second edition, CRC Press, 2005.
175. A.R. Quintana, D. Wang, J.E. Forbes and M.N. Waxham, Kinetics of calmodulin binding to calcineurin, *Biochem. Biophys. Res. Commun.* 334: 674–680, (2005).
176. C. Rensing, B. Mitra and B. P. Rosen**,** The *zntA* gene of *Escherichia coli* encodes a Zn(II)-translocating P-type ATPase, *Proc. Natl. Acad. Sci. USA* 94: 14326-14331, (1997).
177. B.A. Rothermel, R.B. Vega and R.S. Williams, The role of modulatory calcineurin-interacting proteins in calcineurin signaling, *Trends Cardiovasc. Med.* 13: 15–21, (2003).
178. S.I. Rubinow, Introduction to mathematical biology, John Wiley & Sons, Inc. 1975.
179. R. Rudolf, M. Mongillo, R. Rizzuto & T. Pozzan, Looking forward to seeing calcium, *Nature Reviews Molecular Cell Biology* 4: 579-586, (2003).
180. T.P. Runarsson and X. Yao, Search biases in constrained evolutionary optimization, *IEEE Transactions on Systems, Man, and Cybernetics*, Part C, 35: 233–243, (2005).
181. T.P. Runarsson and X. Yao, Stochastic ranking for constrained evolutionary optimization, *IEEE Transactions on Evolutionary Computation* 4: 284–294, (2000).
182. J.C. Rutherford and A.J. Bird, Metal-responsive transcription factors that regulate iron, zinc, and copper homeostasis in eukaryotic cells, *Eukaryotic Cell* 3: 1-13, (2004).
183. C. Salazar and T. HÖfer, Allosteric regulation of the transcription factor NFAT1 by multiple phosphorylation sites: a mathematical analysis, *J. Mol. Biol.* 327: 31–45, (2003).

184. D. Sanders, C. Brownlee, J.F. Harper, Communicating with calcium, *Plant Cell* 11: 691-706, (1999).
185. D. Sanders, J. Pelloux, C. Brownlee, J.F. Harper, Calcium at the crossroads of signaling, *Plant Cell* 14 Suppl.: 401-417, (2002).
186. C. Sardet, R. Dumollard and A. McDougall, Signals and calcium waves at fertilization, *Seminars in Cell & Developmental Biology* 17: 223–225, (2006).
187. T. Schlick, Molecular modeling and simulation: an interdisciplinary guide, Springer Science+Business Media, LLC, 2006.
188. S. Schuster, M. Marhl and T. HÖfer, Modelling of simple and complex calcium oscillations, *Eur. J. Biochem.* 269: 1333-1355, (2002).
189. S.AMG. Scrase-Field and M.R. Knight, Calcium: just a chemical switch? *Current Opinion in Plant Biology* 6: 500-506, (2003).
190. I. Sekler, S.L. Sensi, M. Hershfinkel and W.F. Silverman**,** Mechanism and regulation of cellular zinc transport, *Mol Med.* 13: 337–343, (2007).
191. S. Semsey, A.M.C. Andersson, S. Krishna, M.H. Jensen, E. Masse and K. Sneppen, Genetic regulation of fluxes: iron homeostasis of *Escherichia coli*, *Nucleic Acids Res.* 34: 4960 – 4967, (2006).
192. S.L. Sensi**,** L.M.T. Canzoniero**,** S.P. Yu**,** H.S. Ying**,** J.-Y. Koh**,** G.A. Kerchner and D.W. Choi**,** Measurement of intracellular free zinc in living cortical neurons: routes of entry, *J. Neurosci.* 17: 9554–64, (1997).
193. S.S. Shen-Orr, R. Milo, S. Mangan and U. Alon, Network motifs in the transcriptional regulation network of *Escherichia coli*, *Nature Genetics* 31: 64 – 68, (2002).
194. B.E. Shapiro, A. Levchenko, E.M. Meyerowitz, B.J. Wold and E.D. Mjolsness, Cellerator: extending a computer algebra system to include biochemical arrows for signal transduction simulations, *Bioinformatics* 19: 677-678, (2003).
195. F. Shibasaki, E.R. Price, D. Milan and F. McKeon, Role of kinases and the phosphatase calcineurin in the nuclear shuttling of transcription factor NF-AT4, *Nature* 382: 370-373, (1996).
196. S.-Y. Shin, S.-M. Choo, D. Kim, S.J. Baek, O. Wolkenhauer and K.-H. Cho, Switching feedback mechanisms realize the dual role of MCIP in the regulation of calcineurin activity, *FEBS Letters* 580: 5965-5973, (2006).
197. J.W. Shuai and P. Jung, Optimal ion channel clustering for intracellular calcium signaling, *Proc. Natl. Acad. Sci. USA* 100: 506-510, (2003).
198. T.K. Sigdel, R. Cilliers, P.R. Gursahaney, P. Thompson, J. Allen, Probing the adaptive response of *Escherichia coli* to extracellular Zn(II), *BioMetals* 19: 461–471, (2006).
199. P.M.A. Sloot, D. Frenkel, H.A. Van der Vorst, A. van Kampen, H.E. Bal, P. Klint, R.M.M. Mattheij, J. van Wijk, J. Schaye, H.-J. Langevelde, R.H. Bisseling, B. Smit, E. Valenteyn, H.J. Sips, J.B.T.M. Roerdink and K.G. Langedoen, Computational e-science: studying complex systems in silico. A national coordinated initiative, White Paper, February 2007.
200. S. Smajilovic, J. Tfelt-Hansen, Calcium acts as a first messenger through the calcium-sensing receptor in the cardiovascular system, *Cardiovascular Research* 75: 457-467, (2007).

201. D.J. Smith, D.J. Suggett and N.R. Baker, Is photoinhibition of zooxanthellae photosynthesis the primary cause of thermal bleaching in corals? *Global Change Biol*. 11: 1-11, (2005).
202. M. Solioz and J.V. Stoyanov, Copper homeostasis in *Enterococcus hirae*. *FEMS Microbiol. Rev.* 27: 183-195, (2003).
203. E.D. Sontag, Some new directions in control theory inspired by systems biology, *Syst. Biol.* 1: 9-18, (2004).
204. P.K. Sorger, A reductionist's systems biology, *Current Opinion in Cell Biology* 17: 9–11, (2005).
205. A. Sorin, G. Rosas, R. Rao, *PMR1*, a Ca^{2+}-ATPase in yeast Golgi, has properties distinct from Sarco/endoplasmic reticulum and plasma membrane calcium pumps, *J. Biol. Chem.* 272: 9895-9901, (1997).
206. G. Soveral, A. Veiga, M.C. Loureiro-Dias, A. Tanghe, P. Van Dijck and T.F. Moura, Water channels are important for osmotic adjustments of yeast cells at low temperature. *Microbiology* 152: 1515-1521, (2006).
207. N.C. Spitzer, Calcium: first messenger, *Nature Neuroscience* 11: 243 – 244, (2008).
208. A. Stathopoulos-Gerontides, J.J. Guo, M.S. Cyert, Yeast calcineurin regulates nuclear localization of the Crz1 transcription factor through dephosphorylation, *Genes & Dev.* 13: 798-803, (1999).
209. B.R. Stern, M. Solioz, D. Krewski, P. Aggett, T.-C.Aw, S. Baker, K. Crump, M. Dourson, L. Haber, R. Hertzberg, C. Keen, B. Meek, L. Rudenko, R. Schoeny, W. Slob, T. Starr, Copper and human health: biochemistry, genetics, and strategies for modeling dose-response relationships, *J. Toxicol. Environ. Health B* 10: 157-222, (2007).
210. Steven H. Strogatz, Exploring complex networks, *Nature* 410: 268-276, (2001).
211. J.V. Stoyanov D. Magnani and M. Solioz, Measurement of cytosolic copper, silver, and gold with a *lux* biosensor shows copper and silver, but not gold, efflux by the CopA ATPase of *Escherichia coli*, *FEBS Lett.* 546: 391-394, (2003).
212. J. Strayle, T. Pozzan, H.K. Rudolph, Steady-state free Ca^{2+} in the yeast endoplasmic reticulum reaches only 10μM and is mainly controlled by the secretory pathway pump *Pmr1*, *EMBO J.* 18: 4733-4743, (1999).
213. Z. Szallasi, J. Stelling and V. Periwal, System modeling in cellular biology: from concepts to nuts and bolts, MIT Press, 2006.
214. Y. Takeishi, Q. Huang, J-i. Abe, M. Glassman, W. Che, J-D. Lee, H. Kawakatsu, E.G. Lawrence, B.D. Hoit, B.C. Berk and R.A. Walsh, Src and multiple MAP kinase activation in cardiac hypertrophy and congestive heart failure under chronic pressure-overload: Comparison with acute mechanical stretch, *Journal of Molecular and Cellular Cardiology* 33: 1637-1648, (2001).
215. Y. Takita, L. Engstrom, C. Ungermann, K.W. Cunningham, Inhibition of the Ca^{2+}-ATPase Pmc1p by the v-SNARE protein Nyv1p, *J. Biol. Chem.* 276: 6200-6206, (2001).
216. L.J. Terry, E.B. Shows, S.R. Wente, Crossing the nuclear envelope: hierarchical regulation of nucleocytoplasmic transport, *Science* 318: 1412-1416, (2007).

217. S. Thomine, Cracking the calcium code, *Trends in Plant Science* 6: 501, (2001).
218. J.M.T. Thompson and H.B. Stewart, Nonlinear dynamics and chaos: geometrical methods for engineers and scientists, John Wiley & Sons Ltd., 1991.
219. C. Treiber, Metals on the Brain, *Sci. Aging Knowl. Environ.* 2005: pe27, (2005).
220. A. Trewavas, A brief history of systems biology: "every object that biology studies is a system of systems." Francois Jacob (1974), *Plant Cell* 18: 2420 – 2430, (2006).
221. J.J. Tyson, K.C. Chen, and B. Novak, Sniffers, buzzers, toggles and blinkers:. dynamics of regulatory and signaling pathways in the cell, *Curr. Opin. Cell Biol.* 15: 221-31, (2003).
222. R. van Driel (editor), ESF Forward Look Report: "Systems Biology: a grand challenge for Europe", European Science Foundation, Strasbourg, 2007.
223. L.J. Van Eldik and D.W. Watterson (editors), Calmodulin and signal transduction, Academic Press, 1998.
224. R.B. Vega, R. Bassel-Duby and E.N. Olson, Control of Cardiac growth and function by calcineurin signaling*, J. Biol. Chem.* 278: 36981–36984, (2003).
225. R.B. Vega, B.A. Rothermel, C.J. Weinheimer, A. Kovacs, R.H. Naseem, R. Bassel-Duby, R.S. Williams and E.N. Olson, Dual roles of modulatory calcineurin-interacting protein 1 in cardiac hypertrophy, *Proc. Natl. Acad. Sci. USA* 100: 669–674, (2003).
226. R.B. Vega, J. Yang, B.A. Rothermel, R. Bassel-Duby and R.S. Williams, Multiple domains of MCIP1 contribute to inhibition of calcineurin activity, *J. Biol. Chem.* 277: 30401–30407, (2002).
227. T.N. Vizard, G.W. O'Keeffe, H. Gutierrez, C.H. Kos, D. Riccardi and A.M. Davies, Regulation of axonal and dendritic growth by the extracellular calcium-sensing receptor, *Nat. Neurosci.* 11: 285–291, (2008).
228. E. Voit, A.R. Neves and H. Santos, The intricate side of systems biology, PNAS 103: 9452-9457, (2006).
229. E.O. Voit, Computational analysis of biochemical systems : a practical guide for biochemists and molecular biologists, Cambridge University Press, Cambridge, 2000.
230. G.M. Walker, Yeast physiology and biotechnology, John Wiley & Sons Ltd., 1998.
231. S.E. Webb and A.L. Miller, Calcium signaling during embryonic development, *Nature Reviews Molecular Cell Biology* 4: 539-551, (2003).
232. L.S. Weisman, Yeast vacuole inheritance and dynamics, *Annu. Rev. Genet.* 37: 435-460, (2003).
233. N. Wiener, Cybernetics or control and communication in the animal and the machine, the MIT Press, Cambridge, Massachusetts, 1967.
234. G. Wiesenberger, K. Steinleitner, R. Malli, W. F. Graier, J. Vormann, R. J. Schweyen, J. A. Stadler, Mg^{2+} deprivation elicits rapid Ca^{2+} uptake and activates Ca^{2+}/calcineurin signaling in *Saccharomyces cerevisiae*, *Euk. Cell* 6: 592–599, (2007).

235. C.L. Woldringh, P.G. Huls, N.O.E. Vischer, Volume growth of daughter and parent cells during the cell cycle of *Saccharomyces cerevisiae* a/α as determined by image cytometry, *J. Bacteriology* 175: 3174-3181, (1993).
236. World Health Organization, Vitamin and mineral requirements in human nutrition, World Health Organization, 2nd edition, 2004.
237. K. Yamamoto and A. Ishihama**,** Transcriptional response of *Escherichia coli* to external zinc, *J. Bacteriol.* 187: 6333-6340, (2005).
238. S. Yamasaki, K. Sakata-Sogawa, A. Hasegawa, T. Suzuki, K. Kabu, E. Sato, T. Kurosaki, S. Yamashita, M. Tokunaga, K. Nishida and T. Hirano, Zinc is a novel intracellular second messenger, *J. Cell. Biol.* 177: 637–645, (2007).
239. J. Yang, B. Rothermel, R.B. Vega, N. Frey, T.A. McKinsey, E.N. Olson, R. Bassel-Duby and R.S. Williams, Independent signals control expression of the calcineurin inhibitory proteins MCIP1 and MCIP2 in striated muscles, *Circ. Res.* 87: e61–e68, (2000).
240. L.A. Yatsunyk, J.A. Easton, L.R. Kim, S.A. Sugarbaker, B. Bennett, R.M. Breece, I.I. Vorontsov, D.L. Tierney, M.W. Crowder and A.C. Rosenzweig**,** Structure and metal binding properties of ZnuA, a periplasmic zinc transporter from *Escherichia coli*, *J. Biol. Inorg. Chem.* 13: 271-288, (2008).
241. T.M. Yi, M.I. Simon and J. Doyle, Robust perfect adaptation in bacterial chemotaxis through integral feedback control, *Proc .Natl. Acad. Sci. USA* 97: 4649–4653, (2000).
242. N. Yildirim and M.C. Mackey, Feedback regulation in the lactose operon: a mathematical modeling study and comparison with experimental data, *Biophysical Journal* 84: 2841–2851, (2003).
243. G.W. Zamponi, The L-type calcium channe C-terminus: sparking interest beyond its role in calcium-dependent inactivation, *J. Physiol.* 552: 333, (2003).
244. A. Zappe, Unterschiedliche funktionen der lonenpumpe *Pmr1*, http://elib.uni-stuttgart.de/opus/volltexte/2003/1425.
245. http://www.cellerator.info/
246. http://www.yeastgenome.org/
247. http://www.physiome.org.nz/
248. http://www.bio.vu.nl/hwconf/Silicon/
249. http://www.ihop-net.org/UniPub/iHOP/
250. http://www.ncbi.nlm.nih.gov/Genbank/
251. http://en.wikipedia.org/wiki/Main_Page
252. http://www.eurekalert.org/pub_releases/2007-09/esf-sbp090707.php
253. http://www.esd.ornl.gov/PGG/HERMES/description.html
254. http://www.cellml.org/
255. http://www.cellml.org/models/cui_kaandorp_lloyd_2008_version01
256. http://www.cellml.org/models/cui_kaandorp_lloyd_2008_version01_variant01
257. http://www.vph-noe.eu/

Acknowledgements:

Firstly I would like to thank my promoter Peter Sloot for providing me the opportunity to work as a PhD candidate researcher in his group and for his sustaining support on my research. As mentioned in Chapter 1 of this thesis, one of the greatest challenges of systems biology is the challenge of collaboration. Thank Peter for his enormous efforts of developing Section Computational Science into a comprehensive computational group with a number of international collaborators. The close collaborations within the group and among the international collaborators make the possibilities for tackling various complex biological problems and will surely bring bright prospect in the future (Chapter 3 of this thesis illustrates a good example of the power of collaborations).

Secondly I would like to thank my supervisor Jaap Kaandorp for his appreciation, patience and enthusiasm. His wide relations in the circle of biologists help me to know all kinds of biologists. Thank Peter and Jaap for making me one of the most frequent speakers in ISNB (International Symposium on Networks in Bioinformatics) symposium. It is obvious that ISNB symposium provides us a good platform to develop collaborative relations with pioneering biologists and other important researchers all over the world and to magnify the influence of our research achievements.

Thirdly I would like to thank the Dutch Science Foundation (NWO) for funding my research and for funding ISNB symposium. The research in the field of system biology is like rolling the snow ball during which the initial start may be quite difficult, but once the snow ball gets running, things become easier. Thank NWO and EU again for the funding which delivers the initial push on my research career.

My full respect and gratitude go to Professor Kyle W. Cunningham whose valuable data constitute the basis of Chapter 2 and Chapter 3 of this thesis. The work presented in Chapter 4 will also be impossible without his kind suggestion of the topic.

Special thanks to all the collaborators involved in the works presented in this thesis, including Y. Fomekong Nanfack, Olufisayo O. Ositelu, Olufisayo O. Ositelu, Veronica Beaudry, Alicia Knight and Dr. Catherine M. Lloyd. Thank Catherine again for translating three models (Chapter 2, 4, 5) in this thesis into CellML codes and include them into the CellML Model Repository.

I would also like to thank Dr. Peter Willems, Dr. Leen Torenvliet, Dr. Walter Hoffmann and Dr. Pia Pfluger for their appreciation of my research and mathematical abilities. Thank many members in our group for all kinds of forms of support and thank many biologists and other scientists whom I ever met in person (particularly Prof. Bastien Chopard, Prof. Daan Frenkel, Dr. Nan-nan Zhang, Dr. Drew D. Dudgeon, Drs. Joke blom, Dr. L.J. van den Horn, Dr. Gertien J. Smits, Dr. Sylvia Tambutté, Prof. Matthias Mann, Prof. David Yue, Prof. David Miller, Prof. Denis Allemand, Prof. Sjoerd Verduyn Lunel) or contacted through emails (Dr. Caryn E. Outten, Dr. C.L. Woldringh, Prof. David M.

Bedwell, Prof. Patrick Gervais, Prof. Dietrich H. Nies) in these several years for their advice and discussions.

Finally many thanks to the reading committee of my PhD thesis. Thank you for your time and patience to read such a big bulk of research stuff.

Publication List

Journal Papers:

1. Jiangjun Cui and Jaap Kaandorp, Mathematical modeling of calcium homeostasis in yeast cells, *Cell Calcium* 39: 337-348, (2006).
2. Jiangjun Cui, Jaap Kaandoorp, Olufisayo O. Ositelu, Veronica Beaudry, Alicia Knight, Yves F. Nanfack and Kyle W. Cunningham, Simulating calcium influx and free calcium concentrations in yeast, *Cell Calcium*, in press, doi:10.1016/j.ceca.2008.07.005, (2008).
3. Jiangjun Cui, Jaap Kaandorp and Catherine M. Lloyd, Simulating *in vitro* transcriptional response of Zn^{2+} homeostasis system in *Escherichia coli*, *BMC Systems Biology* 2: 89, (2008).
4. Jiangjun Cui, Jaap A. Kaandorp and P.M.A. Sloot, Calcium homeostasis and signaling in yeast cells and cardiac myocytes (abstract accepted by UK e-Science Programme All Hands Meeting 2008, the full paper submitted to *FEMS Yeast Research*).
5. Jiangjun Cui and Jaap Kaandorp, The modulation on the properties of signaling cycle motif by an inhibitor (in preparation).

Conference paper:

6. Jiangjun Cui and Jaap Kaandorp, Simulating complex calcium-calcineurin signaling network, in M.T. Bubak; G.D. van Albada; J.J. Dongarra and P.M.A. Sloot, editors, *Computational Science - ICCS 2008: 8th International Conference, Krakow, Poland, Proceedings, Part III*, in series *Lecture Notes in Computer Science*, vol. 5103, pp. 110-119. Springer, Berlin, Heidelberg, June 2008.